INTERMITTENCY OF ENERGY DISSIPATION IN MAGNETOHYDRODYNAMIC TURBULENCE

by

Vladimir V. Zhdankin

A dissertation submitted in partial fulfillment of
the requirements for the degree of

Doctor of Philosophy

(Physics)

at the

UNIVERSITY OF WISCONSIN–MADISON

2015

Date of final oral examination: 8/3/15

The dissertation is approved by the following members of the Final Oral Committee:
Stanislav Boldyrev, Professor, Physics
Ellen G. Zweibel, Professor, Astronomy and Physics
Paul W. Terry, Professor, Physics
Jan Egedal, Associate Professor, Physics
Carl Sovinec, Professor, Engineering Physics

© Copyright by Vladimir V. Zhdankin 2015
All Rights Reserved

As customary, but not undeserved, to my parents.

ACKNOWLEDGMENTS

My experiences with the following thesis are best described by analogy. In the early stages, I felt as if I was peacefully flying an airplane through the clouds, admiring the sky with only a vague sense of destination. At some point, I descended below the clouds and came into view of a landing runway. But the runway came at me too rapidly, as I desperately made last-minute adjustments and tried to figure out how to land.

I have many people to thank for a safe landing, and an enjoyable and productive time in graduate school. First and foremost, I thank my mentor, Stas Boldyrev, for introducing me to the field of turbulence, for teaching me good research habits, for always being available for discussions and ideas, for giving me every opportunity to grow as a physicist, and for continually encouraging me to pursue the topics in this thesis.

I also thank Dmitri Uzdensky for a long and fruitful collaboration, for introducing me to plasma astrophysics and magnetic reconnection, and for guidance on a countless number of scientific and practical topics. I also thank Steve Tobias for his bright ideas and for introducing me to the dynamo. I look forward to continuing collaborations with these remarkable theoretical physicists.

I thank Jean Carlos Perez, Joanne Mason, and Qian Xia for helping with the numerical simulations required for my various projects, including performing some of the high-resolution runs. I thank my other collaborators, including Chris Chen, Kirit Makwana, Hui Li, and M.J. Pueschel, for broadening my perspective. I also thank my officemates: Kosta Horaites, Robert Siller, and Bill Capecchi, for making work more vivid and for offering their opinions on various subjects. Finally, I thank the rest of the outstanding plasma physics group at UW-Madison, including the faculty for managing the students and Karsten McCollam for hosting the group talks.

Finally, I thank my family: mother Olga, chemist father Viktor, and bigger brother Vasa. I hope that this thesis does not cause them too much confusion.

CONTENTS

LIST OF TABLES

LIST OF FIGURES

ABSTRACT

Energy dissipation in turbulent plasmas is highly intermittent, which has widespread consequences for laboratory, space, and astrophysical systems. In this thesis, the intermittency of energy dissipation in numerical simulations of driven magnetohydrodynamic turbulence is investigated. A methodology is developed for identifying and characterizing intermittent dissipative structures and spatiotemporal processes. A statistical analysis is then performed on the resulting population. At any given time, the energy dissipation of the system is found to be evenly spread among current sheets with energy dissipation rates, lengths, and widths in the inertial range, and thicknesses localized within the dissipation range. These current sheets are involved in complex, time-asymmetric spatiotemporal processes that have durations up to several large eddy turnover times. The largest and most intense dissipative processes dominate the energy dissipation of the system. The scalings of the statistical properties with Reynolds number are estimated. These results are then compared with the observed statistical properties of solar flares.

1 INTRODUCTION

1.1 Toward understanding turbulence

Turbulence is the complex spatiotemporal behavior of a dynamical field, characterized by irregular and irreversible dynamics, fluctuations across many scales, and energy exchange between many scales. It is commonly observed in three of the four classical states of matter: liquids, gases, and plasmas; it also exists in more exotic forms of matter including various types of quantum fluids (Paoletti and Lathrop, 2011) and gravitational fields (Yang et al., 2015; Green et al., 2014; Adams et al., 2014). Despite its ubiquitous presence in the Universe, decades of extensive experimental and theoretical research, and tantalizing hints of universality, much remains to be discovered about the nature of turbulence in all of these systems.

This thesis is concerned with one of the fundamental aspects of turbulence which eludes a complete, unified understanding: the intermittency of energy dissipation. Intermittency, caused by the stochastic disposition of the turbulent energy cascade as it proceeds from large scales to small scales, is a hallmark of turbulence. It leads to dynamics that are inhomogeneous in space and in time, with different regions exhibiting varying degrees of irregularity. This inhomogeneity is marked by the presence of coherent structures and sporadic temporal activity. A testament to the adversity of intermittency is the fact that although many phenomenological models have been constructed over several decades in attempts to describe it, controversy remains to this day over the appropriate description.

More narrowly, this thesis is concerned with intermittency in large-scale turbulent plasmas. Intermittency takes an elevated role in plasmas, forming sites for magnetic reconnection, particle heating, and particle acceleration, while also affecting processes such as particle diffusion and the dynamo. Intense dissipative events produced by intermittency lead to the localized emission of energetic particles and radiation, which are ideal for experimental and astrophysical observations. Intermittency plays a central role in, for example, instabilities in fusion devices (Carbone et al., 2000; Antar et al., 2003; D'Ippolito et al., 2004), the heating of the solar corona and the solar

wind (Cranmer et al., 2007; Osman et al., 2011; Uritsky et al., 2007), granulation in the solar photosphere (Cattaneo, 1999; Bushby and Houghton, 2005; Stein and Nordlund, 2006), star formation in the interstellar medium (Boldyrev et al., 2002; Pan et al., 2009; Kritsuk et al., 2011; Falgarone et al., 2015), and flares from accreting systems (Di Matteo et al., 1999; Eckart et al., 2009; Albert et al., 2007) and pulsar wind nebulae (Tavani et al., 2011; Abdo et al., 2011).

The goal of this thesis is to systematically assess the properties and dynamical role of intermittent dissipative structures, i.e., current sheets, in magnetohydrodynamic (MHD) turbulence. To accomplish this, we develop a methodology for identifying and characterizing dissipative structures in both space and time. This methodology is then applied to numerical simulations of MHD turbulence, and a statistical analysis of the dissipative structures is performed.

The primary motivation for this work is to advance the theoretical understanding of intermittency in turbulent plasmas. Until recently, the established knowledge of intermittency in plasmas was relatively limited compared to hydrodynamic turbulence. However, this is now changing due to the advent of increasingly powerful numerical simulations, capable of reliably reproducing the turbulent dynamics. These simulations offer an enticing opportunity to probe turbulence and guide theoretical models. A secondary motivation for this work is to better comprehend the potential observable consequences of intermittency in experimental, space, and astrophysical plasmas. In particular, the methodology developed in this work may be valuable for addressing the possible role of turbulence in the heating of the solar corona and solar wind. The remainder of this chapter expounds on these motivations and gives an overview of this thesis.

1.2 What is intermittency?

To illustrate the phenomenon of intermittency, consider the prototypical turbulence: the flow of an incompressible hydrodynamic fluid with relatively small viscosity, or equivalently, with large Reynolds numbers, $\mathrm{Re} = v_0 L/\nu \gg 1$, where v_0 is the characteristic velocity of the flow, L is the characteristic scale of the flow (e.g.,

system size), and ν is the kinematic viscosity. The turbulence is described by the Navier-Stokes equation,

$$\begin{aligned} \partial_t \boldsymbol{v} + \boldsymbol{v} \cdot \nabla \boldsymbol{v} &= -\nabla p + \nu \nabla^2 \boldsymbol{v} \\ \nabla \cdot \boldsymbol{v} &= 0\,, \end{aligned} \tag{1.1}$$

where $\boldsymbol{v}(\boldsymbol{x}, t)$ is the velocity field and $p(\boldsymbol{x}, t)$ is the pressure. For a well-posed problem, the initial conditions and boundary conditions must also be specified. It is also common to add a forcing term which acts at large scales, so that energy lost by the dissipative term $\nu \nabla^2 \boldsymbol{v}$ is replenished and a statistical steady-state can be reached. The resulting dynamics are characterized by a single dimensionless parameter, the Reynolds number, which encapsulates the ratio of the nonlinear term to the dissipative term, $\mathrm{Re} = v_0 L/\nu \sim |\boldsymbol{v} \cdot \nabla \boldsymbol{v}|/|\nu \nabla^2 \boldsymbol{v}|$. The onset of turbulence occurs at $\mathrm{Re} \sim 10^3$; for lower Re, the viscosity damps fluctuations toward a stable (laminar) state.

At the present time, the existence and uniqueness of solutions to the 3D Navier-Stokes equation remains a challenging, high-profile, unsolved mathematical problem (Fefferman, 2000). It remains uncertain whether a complete statistical theory of Navier-Stokes turbulence based on first principles (Eq. 1.1) can be obtained. Despite this, there is an extensive partial understanding of turbulence based on phenomenology. For details on the following discussion, see, for example, Frisch (1995) and Biskamp (2003).

The first major phenomenological framework for turbulence was presented by Kolmogorov (1941) (hereafter, K41), based on the assumption of scale invariance. Specifically, K41 exploited the fact that, when the dissipative term can be neglected, the Navier-Stokes equations have no characteristic scale. Turbulence in this regime can be described as a self-similar heirarchy of eddies. The continuum of scales in which the dynamics exhibit this scale invariance is the known as the inertial range. K41 assumed that the statistical properties of the inertial-range of turbulence are entirely described by the average rate of energy transfer to smaller scales, or equivalently, the mean rate of energy dissipation, $\langle \epsilon \rangle$.

Mathematically, K41 put forward a prediction for the scaling of the structure

functions $S^{(n)}(l)$, which characterize the statistical properties of turbulence. Given the velocity increment between two points separated by $\boldsymbol{l}$, $\delta\boldsymbol{v}_l(\boldsymbol{x}) = \boldsymbol{v}(\boldsymbol{x}+\boldsymbol{l}) - \boldsymbol{v}(\boldsymbol{x})$, the nth order longitudinal structure function is defined by

$$S^{(n)}(l) = \langle(\delta\boldsymbol{v}_l \cdot \boldsymbol{l}/l)^n\rangle\,, \tag{1.2}$$

where the angled brackets denote an ensemble average. By exploiting dimensional analysis, it is inferred that the typical velocity increments must scale as $\delta v_l \sim (\langle\epsilon\rangle l)^{1/3}$, and so the structure functions are given by

$$S^{(n)}(l) = c_n(\langle\epsilon\rangle l)^{n/3} \sim l^{n/3}\,, \tag{1.3}$$

where c_n are universal constants. Several remarkable results are contained in Eq. 1.3. For $n = 2$, one can perform a Fourier transform to obtain the famous inertial-range energy spectrum,

$$E(k) \sim k^{-5/3}\,, \tag{1.4}$$

which agrees extremely well with experiments and numerical simulations. For $n = 3$, Eq. 1.3 is an exact analytical result for inertial-range turbulence, known as Kolmogorov's four-fifths law, since it can be shown that $c_3 = -4/5$. Since $c_3 < 0$, energy is transferred from large scales to small scales on average.

The inertial range in K41 extends from large scales down to the Kolmogorov dissipation scale, $\lambda_\nu = (\nu^3/\langle\epsilon\rangle)^{1/4}$. This scale is derived by equating the dissipative term, $|\nu\nabla^2\boldsymbol{v}| \sim \nu\delta v_\nu/\lambda_\nu^2$, to the nonlinear term, $|\boldsymbol{v}\cdot\nabla\boldsymbol{v}| \sim \delta v_\nu^2/\lambda_\nu$, where $\delta v_\nu \sim (\langle\epsilon\rangle\lambda_\nu)^{1/3}$ is the velocity increment at the dissipation scale. The scales smaller than λ_ν are collectively known as the dissipation range. Scale invariance is broken in the dissipation range, making it nontrivial to describe.

Although the K41 phenomenology was a landmark result in turbulence, it is now known to be incomplete. The predicted energy spectrum and energy flux in Fourier space agree very well with observations, but deviations from Eq. 1.3 are clearly observed for structure functions with $n > 3$. The problem is due to the fact

that, as energy cascades from large scales to small scales, it is distributed unevenly in space, making it inappropriate to use the mean energy dissipation rate $\langle\epsilon\rangle$ in Eq. 1.3. This inherent inhomogeneity of turbulence is known as intermittency.

Intermittency remains one of the most challenging aspects of turbulence to describe theoretically. Nevertheless, there does exist a basic phenomenological framework used to describe intermittency in hydrodynamic turbulence, based on the idea of a random cascade. Obukhov (1962) suggested that the scaling of structure functions given by K41 in Eq. 1.3 can be corrected by using the local value of energy dissipation, which has a scale-dependent distribution. Kolmogorov (1962) (hereafter, K62) then proposed a correction to K41 based on the refined similarity hypothesis,

$$S^{(n)}(l) = d_n \langle \epsilon_l^{n/3} \rangle l^{n/3} \,, \tag{1.5}$$

where d_n are universal constants and the local coarse-grained energy dissipation rate is defined by

$$\epsilon_l = \frac{1}{V_l} \int_{V_l} d^3 r \epsilon(\boldsymbol{r}) \,, \tag{1.6}$$

where $\epsilon = \nu(\partial_i v_j + \partial_j v_i)^2/2$ is the local energy dissipation rate (where indices are to be summed over, and ∂_i denotes the ith component of the gradient), and integration is performed across a region of linear size l and volume V_l. The shape of V_l is unimportant, but usually taken to be a ball (in theoretical studies) or a line (in experimental studies). It is then assumed that the moments of the local energy dissipation rate scale as power laws, $\langle \epsilon_l^n \rangle \sim l^{-\tau_n}$. By the refined similarity hypothesis (Eq. 1.5), this is equivalent to the power-law scaling of the velocity structure functions,

$$S^{(n)}(l) \sim l^{\zeta_n} \,, \tag{1.7}$$

with scaling exponents $\zeta_n = n/3 - \tau_{n/3}$. In general, ζ_n deviates from the linear scaling of K41. This is taken as an indication of intermittency, with the specific scaling depending on the probability density function $P(\epsilon_l)$.

K62 proposed that the stochastic fragmentation of the energy cascade causes $P(\epsilon_l)$ to approach a log-normal distribution at small scales. The fragmentation process can be described by a single free parameter, the intermittency parameter μ, which describes how the variance of $P(\epsilon_l)$ increases as l decreases[1]. The predicted scaling exponents are given by $\tau_n = \mu n(n-1)/2$ for the moments of ϵ_l, and $\zeta_n = n/3 - \mu n(n-3)/18$ for the velocity structure functions. The predicted scaling of ζ_n, in particular, agrees with both experimental and numerical observations up to roughly $n \approx 10$ (Naert et al., 1998; Arneodo et al., 1998, 1999; Molchan, 1997; Mouri et al., 2009).

Much like K41, the K62 phenomenology is a landmark result in the field of turbulence. However, its overall validity remains contested since deviations from the log-normal predictions are observed for $n > 10$, and theoretical shortcomings of the log-normal model have been found for incompressible fluids (Novikov, 1971; Mandelbrot, 1974; Kraichnan, 1974; Schertzer et al., 1997). This led to the development of a number of other random cascade models, culminating in the log-Poisson model (She and Waymire, 1995; Dubrulle, 1994) and the associated She-Lévêque formula (She and Leveque, 1994). These random cascade models generally predict $P(\epsilon_l)$, the scaling of its moments, or related quantities, and link it to velocity structure functions by applying the refined similarity hypothesis. Although these models successfully describe numerical and experimental observations of hydrodynamic turbulence, it is often difficult to distinguish between them in observations (e.g., Nelkin, 1995).

In principle, structure functions form a simple and mathematically robust basis for studying intermittency. However, there are several major challenges associated with structure functions. First of all, it is difficult, if not practically impossible, to accurately measure structure functions of high order. Since higher-order structure functions probe the noisy and unreliable tail of the distribution of velocity gradients, it can be nearly impossible to meaningfully assess structure functions for orders as low as 5 or 6 (Tennekes and Wyngaard, 1972; De Wit, 2004). Furthermore, structure

[1]The scale-dependence of $P(\epsilon_l)$ means that intermittency breaks scale invariance. This does not, however, imply non-universality; on the contrary, the small-scale structure is anticipated to be the most likely aspect of turbulence to be universal (e.g., Sreenivasan and Antonia, 1997). Intermittency is an inherent property of turbulence, with any residual effects from forcing or boundary conditions being wiped out by the fragmentation of the energy cascade across the inertial range.

functions may not exist for all orders, if the distribution declines algebraically rather than exponentially (Frisch, 1995). It is also unclear to what extent the refined similarity hypothesis and assumed power-law scaling for each moment (Eq. 1.7) are valid (Hosokawa and Yamamoto, 1992; Thoroddsen, 1995); indeed, these scalings are often not particularly robust in experimental and numerical observations, although extended self-similarity has been applied to extract improved an scaling (Benzi et al., 1993). Finally, structure functions do not contain all information about the cascade process, missing information about the morphology of dissipative sites, which makes it difficult to predict some effects of intermittency relevant for observations. These issues motivate the development of alternative, more robust and informative approaches to describing intermittency.

1.3 Statistical analysis of structures as a route forward

One remarkable consequence of intermittency is the formation of coherent structures in which energy dissipation is concentrated. In 3D hydrodynamic turbulence, these dissipative structures take the form of quasi-1D vorticity filaments, whereas in magneto-fluids, they take the form of quasi-2D (i.e., ribbon-like) vorticity sheets and current sheets (e.g., Politano et al., 1995; Müller and Biskamp, 2000; Müller et al., 2003; Biskamp, 2003). These coherent structures are often thought to play a central role in the dynamics, although this is sometimes disputed (Tsinober, 1998). In any case, they are observationally important for their roles in heating and particle acceleration, and serve as useful objects for testing models of intermittency. The presence of intermittent structures can be inferred visually from images of quantities such as the vorticity or local energy dissipation rate in numerical simulations, and related surrogates such as low-pressure regions in experiments. Some examples of intermittent vorticity filaments are shown in Fig. 1.1. Coherent structures can also be inferred from non-Gaussian distributions of quantities such as velocity field increments, where the extended tails indicate traversals across the structures.

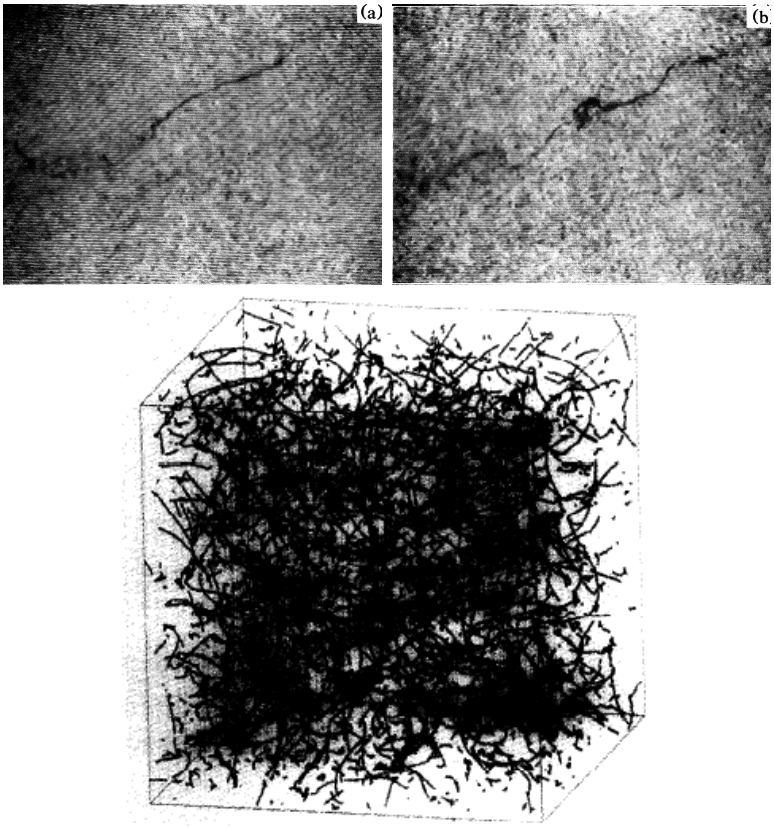

Figure 1.1: Examples of intermittent vorticity filaments in hydrodynamic turbulence. The first image shows the formation of a vorticity filament (5 cm long, 0.1 mm diameter) in a Re $\approx 8 \times 10^4$ turbulent flow created by Douady et al. (1991) (this visualization is possible due to cavitation in low-pressure regions). The second image shows the destabilization of the same filament, 0.02 s later. The third image shows vorticity filaments in a numerical simulation from Kida and Miura (1998).

Due to the close connection between them, it is reasonable to study coherent structures to learn about intermittency. It is convenient, for both practical and theoretical purposes, to treat intermittent structures as discrete objects due to their localized nature and their key dynamical role. The statistical properties of these structures then gives insight into the underlying dynamics. In particular, their sizes, morphology, and energetics can reveal the characteristic dynamical scales, local anisotropies, and overall inhomogeneity. The analysis of structures is well suited not only for theoretical and numerical applications, but also for a large class of experimental and observational problems where dissipative structures and events can be directly identified.

The analysis of intermittent structures is complementary to and distinct from more conventional approaches such as structure functions. In particular, the focus is shifted from the statistics of averages of energy dissipation to the clustering of the energy dissipation, as defined by isosurfaces, thresholds, or other means. This allows a better characterization of dissipative sites, and can give a more transparent, intuitive picture of intermittency.

Statistical analyses of dissipative structures were performed in a number of previous numerical studies of turbulence. Most notably, there are many papers that investigate the statistical properties of dissipative vorticity filaments in hydrodynamic turbulence (e.g., Jiménez et al., 1993; Jimenez and Wray, 1998; Moisy and Jiménez, 2004; Leung et al., 2012). These studies reveal, for example, that the majority of the vorticity is concentrated in filaments whose radii scale with the Kolmogorov microscale while lengths occupy large scales. More recently, attention has been drawn to the statistical properties of dissipative current sheets and vorticity sheets in turbulent plasmas, with investigations in MHD turbulence (Servidio et al., 2009, 2010; Uritsky et al., 2010), the kinematic dynamo (Wilkin et al., 2007), ambipolar diffusion MHD (Momferratos et al., 2014), boundary-driven MHD (Wan et al., 2014), and collisionless turbulence (Makwana et al., 2015). This thesis is based on, and extends the work described in, a series of papers applied to turbulence in reduced MHD simulations (Zhdankin et al., 2013, 2014, 2015c,b).

1.4 Value of temporal information

As with any dynamical physics problem, a complete phenomenological solution of intermittency cannot be claimed unless the dynamics are described in both the spatial and the temporal dimensions. In this respect, most of the previous numerical analyses of intermittent structures have been extremely limited, being based solely on spatial information. The analysis of spatial structures is appropriate for determining the morphology, scaling properties, and instantaneous energetics of the structures, but cannot directly describe the evolution of structures in time. Hence, studies of spatial structures are unable to measure the characteristic timescales, time-integrated energetics, stability, interactions, motion, and impulsiveness of dissipative structures. In order to understand these temporal characteristics, the metholodogy must be extended into the temporal realm.

A temporal analysis of dissipative structures can address several fundamental questions regarding intermittency. One key question is whether, in the limit of high Reynolds number, the overall energy dissipation is dominated by a few intense, long-lasting events residing at large scales, or by many weak, short-lived events residing near the dissipation scale. Another question is whether the spatial and temporal aspects of intermittency are related, e.g., whether larger structures better retain their coherency in time. A third question is whether the dissipative events show any characteristic temporal asymmetry, e.g., an impulsive onset followed by a slow decay, or in contrast, slow growth followed by rapid instability.

Information on temporal intermittency is particularly valuable for space and astrophysical applications, including the heating of the solar corona, since these observations are often very well resolved in time but not in space. Indeed, one usually wants to explain the shape of light curves and the distribution of temporal parameters of flares, such as durations and waiting times. Furthermore, flares in astrophysical systems are often very asymmetric in time, originating from the impulsive onset of an instability or magnetic reconnection (e.g., Bhattacharjee, 2004). Temporal information can therefore be used to constrain models and infer the underlying physical processes.

A major objective of the work described in this thesis is to develop a methodology for the temporal analysis of intermittent dissipative structures. As will be seen, this new framework is based on 4D spatiotemporal objects which represent structures evolving in time. These dissipative processes, analogous to flares in astrophysical systems, may involve many interacting coherent structures. We consider various aspects of processes, including their total dissipated energy, peak energy dissipation rate, duration, and geometric scales; measures of complexity such as the number of interacting structures and types of interactions (mergers and divisions); and the temporal evolution of individual processes. This temporal analysis gives a more complete and informative picture of dissipative structures in turbulence.

1.5 Intermittency in plasmas and astrophysical systems

Plasma, the state of matter described as an ionized gas, is pervasive in the Universe. On the Earth, it is artificially created in laboratory experiments, fusion devices, and some industrial applications. In space, it endures as a natural state of matter. In the solar system, it is a major component of the Sun and its corona, the solar wind, planetary magnetospheres, and the outer heliosphere. Beyond the heliosphere, it is present in the interstellar medium, accretion disks, jets, stars, pulsar wind nebulae, and galaxy clusters. It is also believed to have been ubiquitous in the early Universe (e.g., Brandenburg et al., 1996).

Turbulence is the generic dynamical state of these astrophysical environments due to their large scales. Plasma turbulence is considerably more complex than hydrodynamic turbulence due to electromagnetic effects and, for many systems, the increased importance of kinetic effects. It is therefore not surprising that the present theoretical knowledge of intermittency in plasma turbulence is relatively limited. Despite this, intermittency arguably plays a richer and more significant role in plasmas than in hydrodynamic fluids, due to its extreme experimental and observational consequences.

Turbulent plasmas are often associated with complex, tangled magnetic fields spanning a wide range of scales. This leads to rich dynamics including the occurrence of magnetic reconnection, the release of stored magnetic energy into the kinetic energy of particles via the topological reconfiguration of the large-scale magnetic field. Magnetic reconnection is thought to be the source of energetic particles and radiation observed in a variety of phenomena, including solar and stellar flares, magnetospheric substorms, accretion disk flares, and gamma-ray bursts (e.g., Zweibel and Yamada, 2009).

Magnetic reconnection has a close and subtle relationship with turbulence. In most natural astrophysical systems, both magnetic reconnection and turbulence occur simultaneously with complex, nontrivial interactions between them. Turbulent magnetic reconnection is thought to be ubiquitous in the solar system, occurring in the solar corona (Georgoulis, 2005; Knizhnik et al., 2011; Uritsky et al., 2007, 2013), solar wind (Gosling, 2007; Phan et al., 2010), planetary magnetospheres (Retinò et al., 2007), and outer heliosphere (Drake et al., 2010; Swisdak et al., 2010; Opher et al., 2011; Swisdak et al., 2013). The presence of turbulence in the background ambient plasma before or during magnetic reconnection may invalidate laminar models for reconnection of the large-scale magnetic fields (Parker, 1957; Sweet, 1958; Petschek, 1964), requiring turbulent models of magnetic reconnection (Matthaeus and Lamkin, 1986; Lazarian and Vishniac, 1999; Kim and Diamond, 2001; Kowal et al., 2009; Loureiro et al., 2009) or non-stationary models such as the secondary tearing/plasmoid unstable reconnection (Loureiro et al., 2007; Uzdensky et al., 2010; Baalrud et al., 2012; Huang and Bhattacharjee, 2012; Loureiro et al., 2013). Large-scale turbulence may also continuously drive magnetic reconnection at the bottom of the turbulent cascade; intermittent current sheets can then serve as sites for local reconnection (Servidio et al., 2009, 2010; Zhdankin et al., 2013; Wan et al., 2014).

Intermittent energy dissipation has important consequences in astrophysical systems, regardless of its relationship to magnetic reconnection. For example, in high-energy astrophysical systems, intermittent temperature profiles may occur if strong prompt radiation removes energy from localized dissipation sites faster than it can be conducted through the medium. This can alter the thermodynamics of such

systems, possibly being relevant for the solar corona (Dahlburg et al., 2012), quasars (Goodman and Uzdensky, 2008), accretion disks and flows (Pariev et al., 2003; Blaes, 2013), and hot gas in galaxy clusters. As another example, in collisionless and weakly collisional plasmas, intermittency sets the coherence lengths of electric fields, which accelerate particles to high energies. This may produce a nonthermal population of particles in systems such as the solar wind, radiatively-inefficient accretion flows, galaxy clusters, and molecular clouds. Finally, intermittency may govern the transfer of energy from coronal magnetic fields into heat, which may be relevant for explaining the observed temperatures and flares in solar, stellar, and accretion disk coronae (Uzdensky and Goodman, 2008). In particular, intermittency may play a major role in the long-standing coronal heating problem, as described in the next section.

1.6 The coronal heating problem

The solar corona is arguably the best-observed natural instance of inhomogeneous energy dissipation in a large-scale magnetized plasma. Despite this, the physical processes which govern the coronal dynamics and energetics remain shrouded in mystery. Indeed, the overall theoretical knowledge of energy dissipation in the corona is relatively rudimentary, arguably far behind the observational knowledge. This has led to a major unsolved physics puzzle known as the coronal heating problem (see, e.g., Klimchuk, 2006; Parnell and De Moortel, 2012, for recent reviews). In essence, the question is why the solar corona (at temperatures exceeding 10^6 K) is so much hotter than the solar surface (at temperatures 6×10^3 K), when one would expect the reverse from thermodynamics. Evidently, the strong coronal magnetic fields must be efficiently dissipating energy into heat, but the mechanism by which it does so is unclear. There are two major (but non-exclusive) candidate explanations for coronal heating: wave heating and magnetic reconnection. In both pictures, turbulence may play an important role (e.g., Heyvaerts and Priest, 1992; Asgari-Targhi et al., 2013; Liu et al., 2014; Cranmer et al., 2015).

One particularly attractive solution to the coronal heating problem, based on magnetic reconnection, was proposed and developed by Parker (Parker, 1972, 1983,

1988). In this model, coronal magnetic field lines, which are anchored into and slowly driven by the photosphere, become increasingly tangled until a myriad of small-scale magnetic reconnection events intermittently release the stored energy. These small-scale dissipative events are known as nanoflares, and are conjectured to give the background coronal emission a spiky character at small temporal and spatial scales. In the context of coronal heating, nanoflares have energy scales in the range of $10^{24} - 10^{27}$ ergs, much weaker than the typical observed solar flares with energies up to and exceeding 10^{30} ergs (Hudson, 1991). Hence, nanoflares are often unresolved or difficult to discern even in present-day measurements of coronal emissions. Flares below these energies are expected to not contribute to heating (Aschwanden et al., 2000).

The statistical analysis of dissipative events can help shed light on whether nanoflares are a significant source of heating. This methodology has been extensively applied in observational studies of solar flares (Crosby et al., 1993; Shimizu, 1995; Boffetta et al., 1999; Parnell and Jupp, 2000; Hannah et al., 2008; Aschwanden et al., 2000; Uritsky et al., 2013, 2007; Veronig et al., 2002; Aschwanden et al., 2014) and stellar flares (Benz and Güdel, 1994; Audard et al., 1999; Collura et al., 1988; Pallavicini et al., 1990; Güdel et al., 2003; Telleschi et al., 2005). In these studies, the time-series of extreme UV, soft X-ray, and hard X-ray emissions from the Sun are used to characterize solar flares and to quantify their contribution to the coronal heating. Measured quantities include the size, duration, peak intensity, and fluence of the flares, from which the dissipated energy is inferred. These quantities are ideal for probing the underlying dynamics and constraining potential theoretical models.

A measurement of central importance for Parker's nanoflare model is the probability distribution for the dissipated energy of a flare, $P(E)$. The index of this distribution, in effect, determines whether nanoflares provide a significant contribution to the overall heating. Assuming that dissipative events are well-defined and that the distribution for their dissipated energy is a power law, $P(E) \sim E^{-\alpha}$, the

total energy dissipation (for $\alpha \neq 2$) scales as

$$E_{\rm tot} \sim \int_{E_{\rm min}}^{E_{\rm max}} EP(E)dE \sim \int_{E_{\rm min}}^{E_{\rm max}} E^{1-\alpha}dE \sim \frac{E_{\rm max}^{2-\alpha} - E_{\rm min}^{2-\alpha}}{2-\alpha}\,, \tag{1.8}$$

where $E_{\rm min}$ and $E_{\rm max}$ are arbitrary lower and upper cutoffs, respectively. Assuming that $E_{\rm min} \ll E_{\rm max}$, three distinct scenarios can occur. If $\alpha > 2$, then the term with $E_{\rm max}$ is negligible and $E_{\rm tot}$ scales with $E_{\rm min}$; thus, in this case, the overall energy dissipation is dominated by an enormous number of weak events, i.e., nanoflares, giving the emissions a spiky character at small temporal and spatial scales. If, on the other hand, $\alpha < 2$, then the term with $E_{\rm min}$ is negligible and $E_{\rm tot}$ scales with $E_{\rm max}$; in this case, the overall energy dissipation is dominated by the rarest, strongest dissipative events, which will generally have relatively large temporal and spatial scales. The third possibility, $\alpha = 2$, represents a remarkable special case in which dissipative events of all sizes contribute equally to the overall energy dissipation.

The distribution of solar flare energies is observed to obey a power law across eight orders of magnitude, with an index generally close to -1.8 (Aschwanden et al., 2000), although the precise value varies significantly between different studies depending on the time period, region, type of emission, and methods used to identify the flares. Most importantly, this index is consistently shallower than the critical value of -2, which implies that nanoflares do not have a major contribution to the overall heating of the solar corona. Hence, the viability of the nanoflare picture of coronal heating is presently in doubt.

In addition to the observational evidence against nanoflares, there were a number of theoretical and numerical studies of Parker's nanoflare model. The system is often modeled in the framework of MHD with line-tied boundary conditions and slow driving at these boundaries. Numerical simulations of this system show the production of current sheets with power-law scaling relations (e.g., Longcope and Sudan, 1994; Dmitruk and Gómez, 1999; Einaudi and Velli, 1999; Rappazzo et al., 2008, 2010) and power-law distributions of flare intensities (e.g., Dmitruk and Gómez, 1997; Georgoulis et al., 1998; Einaudi and Velli, 1999; Nigro et al., 2004; Buchlin and Velli, 2007; Ng and Lin, 2012). Generally, these studies also find an index shallower

than the critical value.

This brings to our attention another major question about the solar corona: what physical process governs the intermittent release of large-scale magnetic energy observed in solar flares, microflares, and nanoflares? There currently exist two major candidates for the answer: self-organized criticality and turbulence (e.g., Georgoulis, 2005; Uritsky et al., 2007, 2013). Although the predictions for the statistical properties of dissipative events due to self-organized criticality are clearly presented in the literature (Aschwanden, 2012b; Aschwanden, 2014), the equivalent has not yet been concretely established for turbulence.

The methodology developed in this thesis for MHD turbulence has many similarities with, and is partly inspired by, the investigations of solar flares and nanoflares. A comparison between the dissipative events in both systems will help address whether MHD turbulence can explain the intermittent heating of the solar corona. More broadly, the questions regarding intermittency in the solar corona are equally important questions for MHD turbulence itself (Einaudi and Velli, 1999). One key question is whether, in the limit of high Reynolds number, the overall energy dissipation is dominated by a few intense, long-lasting events residing at large scales (i.e., coherent structures), or by many weak, short-lived events residing at the dissipation scale (i.e., nanoflares). Qualitatively, the question is whether intermittency is coherently self-organized in both space and time, or spiky in space and bursty in time. Despite its simplicity, this question appears to be unanswered in the previous literature on MHD turbulence.

1.7 Overview of thesis

The primary goal of this thesis is to gain a basic understanding of the intermittency of energy dissipation in MHD turbulence. Although intermittency was long recognized to form intense dissipative current sheets and vorticity sheets, their statistical properties and scalings with Reynolds number have not been previously investigated in a systematic and quantitative manner. To address this, we develop a methodology for investigating intermittent dissipative structures. We develop methods for identifying

dissipative structures and for measuring their spatial and temporal characteristics. We then apply these methods to a series of numerical simulations of reduced MHD to investigate the statistical properties of dissipative current sheets in MHD turbulence with varying Reynolds numbers.

From this statistical analysis, we uncover the distributions and scaling relations that describe the dissipative current sheets. The main results of this thesis are as follows. First, we verify that energy dissipation is dominated by thin current sheets with thicknesses that are inside the dissipation range. We additionally find that these current sheets have lengths and widths that span the inertial range. We find that, instantaneously, the energy dissipation is distributed evenly amongst structures of all energy dissipation rates, lengths, and widths in the inertial range. As the Reynolds number is increased, the structures become thinner and more numerous, while their lengths and widths continue to occupy a continuum of inertial-range scales up to the system size. We find that these current sheets participate in complex spatiotemporal processes with durations proportional to the maximum length of the constituent structures. We find that these dissipative processes exhibit a slight but consistent asymmetry in time, evidently due to the turbulent cascade. Upon accounting for the temporal profile of dissipative structures, we find that the overall energy dissipation is dominated by the largest and most intense dissipative events. In this sense, intermittent energy dissipation in MHD turbulence is concentrated in large-scale coherent structures rather than nanoflares.

A secondary goal for this thesis is to provide a preliminary assessment of whether intermittent energy dissipation in the solar corona may be consistent with MHD turbulence. To this end, we compare our numerical results for the dissipative events with the previously observed statistical properties of solar flares. This comparison is necessarily limited, since our numerical simulations are not applicable for describing all aspects of the coronal dynamics, due to differences in boundary conditions and driving mechanisms, and the exclusion of numerous physical effects. Regardless, we find several nontrivial similarities with the statistics of solar flares, including similar indices in both cases for the distribution of dissipated energy, motivating a more detailed comparison in the future.

This thesis is organized as follows. Chapter 2 is an overview of the present-day phenomenology of MHD turbulence and intermittency, which includes some remarks on dissipative structures in reduced MHD. Chapter 3 describes the methodology developed for the statistical analysis of dissipative structures and spatiotemporal processes. This includes descriptions of the methods and numerical algorithms used for identifying structures, measuring their morphology, and tracking them in time. The presentation of the results begins in Chapter 4, which describes the numerical simulations and the distribution of local energy dissipation rates. This chapter also shows that the coarse-grained energy dissipation rate is relatively well described as a log-normal random cascade. Chapter 5 contains our statistical analysis of dissipative current sheets, including the distributions and scaling properties of their energy dissipation rates and geometric scales. Chapter 6 follows with our statistical analysis of time-evolving current sheets, i.e., dissipative processes. This chapter also compares the statistical properties of dissipative processes in our simulations with observations of solar flares. Finally, Chapter 7 summarizes the results, discusses implications, and outlines directions for future work.

2 BACKGROUND

2.1 Magnetohydrodynamics

This chapter describes the idealized system which is the focus of this thesis: driven incompressible magnetohydrodynamic (MHD) turbulence. Specifically, this section describes the MHD equations, Sec. 2.2 describes the inertial-range phenomenology and some aspects of intermittency, and Sec. 2.3 includes some remarks on dissipative structures in reduced MHD.

Kinetic theory provides the most fundamental description of a plasma. It is based on the Maxwell-Vlasov equations, which describe the evolution of the distribution function of ion and electron positions and velocities, as well as the evolution of the electric and magnetic fields (see, e.g., Gurnett and Bhattacharjee, 2005). A major drawback of kinetic theory is that the equations are computationally expensive, having a large phase space including the position and velocity information for all particle species. There are a number of simpler models which approximate the plasma dynamics in certain parameter regimes. In particular, for a collisional plasma with scales much larger than the ion gyroradius and frequencies lower than the ion gyrofrequency, MHD is derived by taking moments of the Maxwell-Vlasov equation. MHD turbulence, rather than kinetic turbulence, will be the focus of this thesis for the following reasons. First, it is the most tractable model of a plasma, both theoretically and computationally. Second, it shares many conceptual similarities with hydrodynamic turbulence, including well-defined inertial ranges and dissipation ranges. Characterizing turbulence in the kinetic regime, on the other hand, requires a broader framework (e.g., Schekochihin et al., 2009; Servidio et al., 2014). Third, many astrophysical plasmas are thought to be well approximated by MHD, although one must be cautious because the derivation of MHD assumes a collisional plasma, whereas astrophysical systems are often collisionless.

MHD describes the large-scale, low-frequency dynamics of an electrically conductive fluid, including plasmas and liquid metals (e.g., Biskamp, 2003). In MHD turbulence, turbulent motions amplify the magnetic field $\boldsymbol{B}$ via the dynamo effect

until it becomes dynamically relevant. The incompressible MHD equations can be written out as

$$\begin{aligned} \partial_t \boldsymbol{v} + \boldsymbol{v} \cdot \nabla \boldsymbol{v} - \boldsymbol{B} \cdot \nabla \boldsymbol{B} &= -\nabla P + \nu \nabla^2 \boldsymbol{v} + \boldsymbol{f}_v \\ \partial_t \boldsymbol{B} + \boldsymbol{v} \cdot \nabla \boldsymbol{B} - \boldsymbol{B} \cdot \nabla \boldsymbol{v} &= \eta \nabla^2 \boldsymbol{B} + \boldsymbol{f}_b \\ \nabla \cdot \boldsymbol{v} = \nabla \cdot \boldsymbol{B} &= 0\,, \end{aligned} \tag{2.1}$$

where P is the total (magnetic and plasma) pressure, ν is the viscosity, η is the magnetic diffusivity, and $\boldsymbol{B} = \boldsymbol{B}_0 + \boldsymbol{b}$, where $\boldsymbol{B}_0 = \langle \boldsymbol{B} \rangle$ is a uniform background field and $\boldsymbol{b}$ is the fluctuating part satisfying $\langle \boldsymbol{b} \rangle = 0$. The units are such that $\boldsymbol{B}$ is scaled by $\sqrt{4\pi\rho_0}$, where ρ_0 is uniform plasma density, giving it the same units as velocity. The equations are also supplemented with arbitrary forcing terms, $\boldsymbol{f}_v$ and $\boldsymbol{f}_b$, which describe the input of energy at large scales. The first line in Eq 2.1 is essentially the Navier-Stokes equation while the second line comes from Maxwell's equations. The MHD equations take a more symmetric form when recast in terms of the Elsässer variables, $\boldsymbol{z}^{\pm} = \boldsymbol{v} \pm \boldsymbol{b}$, which gives

$$\begin{aligned} \left(\partial_t \mp \boldsymbol{B}_0 \cdot \nabla\right) \boldsymbol{z}^{\pm} + \left(\boldsymbol{z}^{\mp} \cdot \nabla\right) \boldsymbol{z}^{\pm} &= -\nabla P + \nu \nabla^2 \boldsymbol{z}^{\pm} + \boldsymbol{f}^{\pm} \\ \nabla \cdot \boldsymbol{z}^{\pm} &= 0\,. \end{aligned} \tag{2.2}$$

For simplicity, we have assumed that $\eta = \nu$ (i.e., a magnetic Prandtl number of $Pm = 1$), which is the case for all numerical simulations considered in this thesis. Hence, the Reynolds number $\mathrm{Re} = v_0 L/\nu$ is equal to the magnetic Reynolds numbers $\mathrm{Rm} = v_0 L/\eta$.

Energy loss from the above system is governed by resistive dissipation and viscous dissipation, with respective contributions to the average energy dissipation rate per unit volume given by $\epsilon^{\eta} = \eta j^2$ and $\epsilon^{\nu} = \nu \omega^2$, where $\boldsymbol{j} = \nabla \times \boldsymbol{B}$ is the current density and $\boldsymbol{\omega} = \nabla \times \boldsymbol{v}$ is the vorticity. By contrast, in many natural plasmas, the energy dissipation is governed by more complex kinetic physics which, in general, is not directly associated with the current density and vorticity. Although the mechanism of energy dissipation used here is therefore idealized, the large-scale dynamics of a

turbulent plasma, including its intermittency, are thought to be insensitive to the specific mechanism of dissipation.

There are several things that make MHD turbulence significantly more complex and richer than hydrodynamic turbulence. First of all, the system is described by two vector fields, $\boldsymbol{v}$ and $\boldsymbol{b}$, which may be nontrivially correlated. Second, the dynamics are anisotropic due to the presence of the large-scale magnetic field, which becomes increasingly important at small scales. Third, unlike incompressible Navier-Stokes turbulence, MHD has Alfvén waves in addition to nonlinear eddies, which is encapsulated in the linear term proportional to B_0. This necessitates a distinction between weak turbulence, i.e., turbulence dominated by linear waves (Galtier et al., 2000), and strong turbulence, i.e., turbulence in which the nonlinear term is comparable to the linear term. For the remainder of thesis, we focus on strong turbulence.

In this thesis, we further focus on an approximation of the MHD equations known as reduced MHD (RMHD) (Kadomtsev and Kantorovich, 1974; Strauss, 1976). RMHD assumes a uniform background magnetic field $\boldsymbol{B}_0 = B_0\hat{z}$ that is strong relative to turbulent fluctuations (i.e., $B_0 \gg b_{\rm rms}$), and that typical gradients along $\boldsymbol{B}_0$ are much smaller than those perpendicular to $\boldsymbol{B}_0$. In this limit, the fluctuating component along $\boldsymbol{B}_0$ can be ignored, so that Eq. 2.2 can be written as

$$\begin{aligned} \left(\partial_t \mp \boldsymbol{B}_0 \cdot \nabla_\parallel\right) \boldsymbol{z}^\pm + \left(\boldsymbol{z}^\mp \cdot \nabla_\perp\right) \boldsymbol{z}^\pm &= -\nabla_\perp P + \nu \nabla_\perp^2 \boldsymbol{z}^\pm + \boldsymbol{f}_\perp^\pm \\ \nabla_\perp \cdot \boldsymbol{z}^\pm &= 0\,, \end{aligned} \tag{2.3}$$

where $\nabla_\parallel = \hat{z}\partial_z$ and $\nabla_\perp = \hat{x}\partial_x + \hat{y}\partial_y$. In this case, the fields $\boldsymbol{z}^\pm$ (and also $\boldsymbol{v}$, $\boldsymbol{b}$) all have directions strictly perpendicular to $\boldsymbol{B}_0$. Hence, in RMHD, only the z-component of current density and vorticity are nonvanishing, so that $j = \hat{z} \cdot \nabla_\perp \times \boldsymbol{b}$ and $\omega = \hat{z} \cdot \nabla_\perp \times \boldsymbol{v}$; these two scalar fields contain complete information to describe the dynamics as well as energetics.

An alternative form of the RMHD equations can be obtained in terms of the scalar potentials: the magnetic flux function ψ and stream function ϕ. The RMHD

equations are then

$$\begin{aligned} \partial_t \psi + \boldsymbol{v} \cdot \nabla \psi &= B_0 \partial_z \phi + \eta \nabla^2 \psi \\ \partial_t \omega + \boldsymbol{v} \cdot \nabla \omega - \boldsymbol{b} \cdot \nabla j &= B_0 \partial_z j + \nu \nabla^2 \omega \,, \end{aligned} \tag{2.4}$$

where $\boldsymbol{b} = \hat{z} \times \nabla \psi$, $\boldsymbol{v} = \hat{z} \times \nabla \phi$, $\omega = \nabla_\perp^2 \phi$, and $j = \nabla_\perp^2 \psi$.

RMHD is of significant practical and theoretical utility. In most natural systems, a strong background field is present when attention is drawn to scales small compared to the system size, due to the large-scale magnetic fields acting as an effective background field at small scales, so that $B_0 \gg b_{\mathrm{rms}}$. Likewise, the dynamics naturally develop steeper gradients in the directions perpendicular to the guide field than parallel to it. Hence, the central assumptions of RMHD are often satisfied at small scales. RMHD is more analytically tractable than the full MHD equations because there are only two unknown scalar fields, ψ and ϕ, or equivalently, j and ω. Another attractive feature of RMHD is its applicability to collisionless plasmas, which is not a-priori true for the full MHD equations (Schekochihin et al., 2009).

The RMHD equations represent the "first principles" upon which this work is based on. They impose constraints on the statistical properties and morphology of intermittent structures, although it is generally very difficult to extract this information directly from the equations.

2.2 Phenomenology of MHD turbulence

Inertial-range phenomenology

This section sets the stage for the subsequent numerical analysis in this thesis by briefly reviewing the present phenomenological theories of MHD turbulence. These models are idealized in the sense that they assume infinitely large Reynolds numbers, and hence cannot reliably describe dynamics near the dissipation scale. Although these theories do not account for intermittency, they are still valuable for providing estimates for the dissipation scale and anisotropy of typical turbulent eddies.

Recall that in the K41 phenomenology for hydrodynamic turbulence (described in Sec. 1.2), dimensional analysis requires that the velocity increments across a given scale are related to the energy cascade rate by $\delta v_l \sim (\langle\epsilon\rangle l)^{1/3}$, which implies an energy spectrum of $E(k) \sim k^{-5/3}$. This argument, however, cannot be applied directly to MHD turbulence, due to the fact that the additional quantities, namely, B_0 and the possible correlations between the two independent fields, prevent dimensional analysis from giving a unique result. In order to develop a more suitable phenomenological framework, the MHD dynamics must be considered more carefully.

There are two major qualitative differences between incompressible MHD turbulence (described by Eq. 2.2) and Navier-Stokes turbulence. The first difference is the presence of a linear term in the equations due to the background field $\boldsymbol{B}_0$, or more generally, a local background field is created by large-scale turbulent fluctuations. This background field creates an inherent anisotropy and plays an essential dynamical role since, in the limit of small fluctuations, linear Alfvén waves can propagate along it with dispersion relation $\omega^{\pm}(\boldsymbol{k}) = \pm k_{\parallel} v_A$, where $\omega^{\pm}(\boldsymbol{k})$ is the frequency of the mode (not to be confused with vorticity), $k_{\parallel}$ is the wavenumber parallel to the background magnetic field, and v_A is the Alfvén velocity (equal to B_0 in the given units). The presence of these linear waves sets an additional characteristic timescale, the Alfvén time $\tau_A = l_{\parallel}/v_A$, where $l_{\parallel}$ is the given scale along the local guide field. The second difference between MHD turbulence and Navier-Stokes turbulence is the presence of two independent fields $\boldsymbol{z}^{\pm}$, which in general are nontrivially correlated through interactions mediated by the nonlinearity.

A phenomenological picture that convincingly accounted for anisotropy in MHD turbulence was proposed by Goldreich and Sridhar (1995) (henceforth, GS95). The GS95 phenomenology was based on the conjecture that the timescale for the linear Alfvén waves traveling along the background field, $\tau_A = l_{\parallel}/v_A$, equals the timescale for the nonlinear cascade transverse to the background field, $\tau_{\rm NL} = l_{\perp}/\delta v_l$. Hence, turbulent eddies are anisotropic, with scales related by

$$l_{\parallel}/l_{\perp} \sim v_A/\delta v_l \,. \tag{2.5}$$

This is known as critical balance, and is based on the following insight. When $\tau_A \ll \tau_{NL}$, the dynamics are in the regime of weak turbulence. When Re is large enough, the theory of weak turbulence implies that there is a scale below which it transitions into strong turbulence, which occurs at $\tau_A \sim \tau_{NL}$. When $\tau_A \gg \tau_{NL}$, motions along the background field become decorrelated and naturally evolve toward $\tau_A \sim \tau_{NL}$. Hence, the dynamics are attracted toward the critical balanced state.

Under critical balance, the equality of the linear and nonlinear timescales removes the ambiguity in dimensional analysis caused by B_0. By the same reasoning as K41, it is found that

$$\delta v_l \sim (\langle \epsilon \rangle l_\perp)^{1/3}, \tag{2.6}$$

giving an energy spectrum $E(k_\perp) \sim k_\perp^{-5/3}$ in the direction perpendicular to the background field. In contrast, eddies tend to be elongated in the parallel direction, with the scaling given by

$$l_\parallel \sim \frac{v_A}{\delta v_l} l_\perp \sim v_A \langle \epsilon \rangle^{-1/3} l_\perp^{2/3} \sim l_\perp^{2/3}. \tag{2.7}$$

Hence, the anisotropy of structures (i.e., $l_\parallel / l_\perp$) increases with decreasing scale. These arguments also imply that the dissipation scale in the perpendicular direction is the same as in K41, $l_{\perp,\eta} \sim \eta^{3/4}$, while in the parallel direction it scales as $l_{\parallel,\eta} \sim \eta^{1/2}$.

The GS95 phenomenology is a landmark result in MHD turbulence, with some aspects of it, such as critical balance, supported by numerical simulations (Cho et al., 2002; Beresnyak, 2011), solar wind measurements (Podesta, 2009; Wicks et al., 2010; Chen et al., 2011), and observations of electron density fluctuations in the interstellar medium (Armstrong et al., 1995). However, there are also indications that it may not be completely correct. In particular, numerical simulations often tend to exhibit a spectrum closer to $E(k_\perp) \sim k_\perp^{-3/2}$ (e.g., Mason et al., 2008; Perez et al., 2012). On more theoretical grounds, although the notion of critical balance seems to be reasonable, GS95 does not take into account the possible correlations between $\boldsymbol{b}$ and $\boldsymbol{v}$.

Building off of GS95, a more general phenomenology developed by Boldyrev (2005, 2006) takes into account these correlations by allowing for a scale-dependent alignment between $\boldsymbol{b}$ and $\boldsymbol{v}$. Referred to as scale-dependent dynamic alignment, this model obtains an energy spectrum of $E(k_\perp) = k_\perp^{-3/2}$ by assuming that the alignment angle between fluctuating magnetic and velocity field, $\theta_\lambda = \cos^{-1}(\boldsymbol{b}_\lambda \cdot \boldsymbol{v}_\lambda/(b_\lambda v_\lambda))$, scales as $\theta_\lambda \sim \lambda^{1/4}$. This dynamic alignment causes inertial-range turbulent eddies to be anisotropic in three directions, rather than the two directions in GS95. The typical eddy is characterized by the length l in the field-parallel direction, the width ξ along the fluctuating velocity $\boldsymbol{v}_\lambda$ and fluctuating magnetic field $\boldsymbol{b}_\lambda$, and the thickness λ in the field-perpendicular direction but transverse to $\boldsymbol{v}_\lambda$ and $\boldsymbol{b}_\lambda$. These quantities are found to scale as

$$\begin{aligned} \xi &\sim \lambda^{3/4}\,, \\ l &\sim \xi^{2/3} \sim \lambda^{1/2}\,. \end{aligned} \tag{2.8}$$

Accordingly, the typical velocity and magnetic field fluctuations in the inertial range scale as

$$v_\lambda \sim b_\lambda \sim \lambda^{1/4}\,. \tag{2.9}$$

The dissipation scale for MHD turbulence with dynamic alignment can be obtained by equating the resistive diffusion time, $\tau_\eta = \lambda_\eta^2/\eta$, to the characteristic nonlinear timescale (the eddy turnover time), $\tau_\lambda = \xi_\lambda/v_\lambda \sim \lambda^{1/2}$, to obtain

$$\lambda_\eta \sim \eta^{2/3}\,. \tag{2.10}$$

Most notably, this differs from the GS95 prediction of $\lambda_\eta \sim \eta^{3/4}$. The dissipation scale in the other directions is given by

$$\begin{aligned} \xi_\eta &\sim \eta^{1/2} \\ l_\eta &\sim \eta^{1/3}\,. \end{aligned} \tag{2.11}$$

Scale-dependent dynamic alignment therefore naturally predicts the creation of ribbon-like turbulent eddies, which may be associated with the observed intermittent current sheets. However, the exact connection is unclear since scale-dependent dynamic alignment is based on non-intermittent, inertial-range phenomenology.

Intermittency phenomenology

There are a number of different methods conventionally employed to describe intermittency in plasmas, including structure functions (Horbury and Balogh, 1997; Müller et al., 2003; Chen et al., 2010, 2011; Podesta, 2011), topological methods (Servidio et al., 2009, 2010; Wan et al., 2014), and statistics of discontinuities (Greco et al., 2009a,b; Servidio et al., 2011; Wan et al., 2012b; Zhdankin et al., 2012b,a). However, phenomenological models for intermittency are largely limited to the random cascade models originating in hydrodynamic turbulence. In particular, the log-Poisson model was often used to describe the scaling of structure functions in MHD turbulence (Grauer et al., 1994; Politano and Pouquet, 1998; Müller and Biskamp, 2000; Müller et al., 2003; **?**). For example, Müller and Biskamp (2000) proposed using the log-Poisson model with assumptions of 2D structures and Kolmogorov scaling; they found good agreement with numerical simulations (Müller et al., 2003). However, the connection between structure functions and the energy cascade rate is nontrivial, due to the necessity of formulating a refined similarity hypothesis for MHD.

A more direct and transparent route to understanding intermittency is to investigate the statistics of energy dissipation rather than structure functions. The energy dissipation rate is more closely related to the previous phenomenological ideas of intermittency, being essentially equivalent to the energy cascade rate. Biskamp (1995, 2003) noted that the log-normal model is a good approximation to the distribution of coarse-grained energy dissipation rates in the inertial range for 2D numerical simulations of MHD turbulence, while later studies found the distribution moments to be consistent with the log-Poisson model (Bershadskii, 2003; Merrifield et al., 2005). We will revisit these phenomenological models in Chapter 4.

2.3 Remarks on intermittent structures

In this section, we describe some properties of intermittent structures that can be inferred from the RMHD equations. Although we mainly deal with structures in the current density j in this thesis, it is mathematically more tangible to work with structures in the Elsässer vorticities, $\omega^{\pm}$. Hence, it is apt and instructive to consider the properties of Elsässer vorticity structures. Although intermittency in $\omega^{\pm}$ is not necessarily identical to that in j and ω, the overall statistical features are similar in both cases.

The RMHD equation for ψ (from Eq. 2.4) can be rewritten for j by using the identity (where indices are to be summed over perpendicular components, and $(x, y, z) = (x_1, x_2, x_3)$)

$$\begin{aligned}
\nabla_{\perp}^2(\boldsymbol{v}\cdot\nabla\psi) &= \epsilon_{ij3}\partial_k\partial_k(\partial_i\phi\partial_j\psi) \\
&= \epsilon_{ij3}\partial_k(\partial_i\partial_k\phi\partial_j\psi + \partial_i\phi\partial_j\partial_k\psi) \\
&= \epsilon_{ij3}(\partial_i\partial_k\partial_k\phi\partial_j\psi + 2\partial_i\partial_k\phi\partial_j\partial_k\psi + \partial_i\phi\partial_j\partial_k\partial_k\psi) \\
&= \boldsymbol{v}\cdot\nabla j - \boldsymbol{b}\cdot\nabla\omega + 2\epsilon_{ij3}\partial_i\partial_k\phi\partial_j\partial_k\psi\,, \qquad (2.12)
\end{aligned}$$

which leads to the RMHD equations for current density and vorticity,

$$\begin{aligned}
\partial_t j + \boldsymbol{v}\cdot\nabla j - \boldsymbol{b}\cdot\nabla\omega + 2\epsilon_{ij3}\partial_i\partial_k\phi\partial_j\partial_k\psi &= B_0\partial_z\omega + \eta\nabla^2 j \\
\partial_t\omega + \boldsymbol{v}\cdot\nabla\omega - \boldsymbol{b}\cdot\nabla j &= B_0\partial_z j + \nu\nabla^2\omega\,. \qquad (2.13)
\end{aligned}$$

The RMHD equations for Elsässer vorticities, $\omega^{\pm} = \omega \pm j$, are then

$$\partial_t\omega^{\pm} + \epsilon_{ij3}\partial_i\partial_k\phi^{\mp}\partial_j\partial_k\phi^{\pm} + \epsilon_{ij3}\partial_i\phi^{\mp}\partial_j\omega^{\pm} = \pm B_0\partial_3\omega^{\pm} + \eta\partial_k\partial_k\omega^{\pm}\,, \qquad (2.14)$$

where we assumed that $\eta = \nu$. We use this form of the equations to show several properties of structures below.

Consider structures defined by isosurfaces at $\omega^{+} = \omega_{\rm thr}$, with corresponding normal vector $\hat{n} = -\nabla\omega^{+}/|\nabla\omega^{+}|$. Integration of Eq. 2.14 across the enclosed volume

$\mathcal{V}$ (containing $\omega^+ > \omega_{\rm thr}$) eliminates the advective terms (via the divergence theorem), giving

$$\int_{\mathcal{V}} dV \left(\partial_t \omega^+ + \epsilon_{ij3}\partial_i\partial_k\phi^-\partial_j\partial_k\phi^+ - \eta\partial_k\partial_k\omega^+\right) = 0\,. \tag{2.15}$$

The first term here describes the overall growth or decay of the structure, the second term describes the nonlinear interactions with the opposite field (which can contribute either to growth or decay), and the third term describes the decay due to dissipation. An analogous equation for structures in ω^- (i.e., volumes bounded by an isosurface at $\omega^- = \omega_{\rm thr}$) is obtained by interchanging ϕ^+ and ϕ^- in Eq. 2.15.

Symmetries

Before moving on, we note that the RMHD equations have the following basic symmetries:

- $(x_1, x_2, x_3, t) \to (hx_1, hx_2, h^2x_3, h^2t)$ and $\phi^\pm \to \phi^\pm$ (scaling)
- $x_1 \to -x_1$ (or $x_2 \to -x_2$) and $\phi^\pm \to -\phi^\pm$ (parity)
- $x_3 \to -x_3$ and $\phi^\pm \to \phi^\mp$ (orientation)
- $t \to -t$ and $\phi^\pm \to -\phi^\mp$ if $\eta = 0$ (time-reversal)
- $t \leftrightarrow x_3/B_0$ and $\phi^- \to -\phi^-$ if $\eta = 0$
- $t \leftrightarrow -x_3/B_0$ and $\phi^+ \to -\phi^+$ if $\eta = 0$

where h is an arbitrary constant. Spatial symmetry is therefore associated with the exchange of the Elsässer populations or the simultaneous reversal of their signs. Temporal symmetry is associated with the combination of these operations, but is broken by dissipation.

The last two symmetries indicate a subtle relationship between the temporal dynamics and the spatial variation along $\boldsymbol{B}_0$. In essence, if the dissipation is ignored, then the dynamics are equivalent in both of these dimensions after either population

is individually reversed in sign. Reversing the sign of one population, however, affects the correlations between the two populations; thus the symmetry is spontaneously broken. Regardless, since the correlations are observed to be relatively weak (as will be shown in Sec. 4.3), the temporal evolution of structures is roughly similar the spatial variation along $\boldsymbol{B}_0$. This statement appears to be related to critical balance ($\tau_{\mathrm{NL}} \sim \tau_A = l_\parallel / v_A$), which is thought to be a robust property of reduced MHD at all scales (Mallet et al., 2015). The linear relationship between timescales and parallel length scales in critical balance implies that the lifetimes of structures should be proportional to their maximum lengths.

Correlations

A qualitative argument for correlations between ω^+ and ω^- can be made as follows. Since the nonlinear term acts with opposite sign on ω^- (at any given point) than on ω^+, the structures interact in such a way that if the nonlinearity causes ω^+ to increase, then ω^- will decrease by a corresponding amount. Hence, one would expect a tendency for structures with $\omega^+ > 0$ to be correlated with structures with $\omega^- < 0$, and for $\omega^+ < 0$ to be correlated with $\omega^- > 0$. This implies that fluctuations in j will tend to have a larger amplitude than in ω.

Morphology

Although the advective terms in Eq. 2.15 vanish upon integration across a structure, they may still influence its morphology. In particular, advection causes the structure to be stretched along $\boldsymbol{z}^-$ and $\boldsymbol{B}_0$, giving it a sheet-like morphology. One may estimate the advective terms inside the structure from Eq. 2.14, roughly as

$$\begin{aligned} |B_0 \partial_3 \omega^+| &\sim \frac{B_0 \omega_{\mathrm{thr}}}{L^*} \\ |\epsilon_{ij3} \partial_i \phi^- \partial_j \omega^+| &\sim \frac{z_0 \omega_{\mathrm{thr}}}{W^*}\,, \end{aligned} \tag{2.16}$$

where the length L^* and width W^* are the characteristic scales along $\boldsymbol{B}_0$ and along $\boldsymbol{z}^-$, respectively, and z_0 is the typical magnitude of the background $\boldsymbol{z}^-$. If these terms are of comparable magnitude, then $W^* \sim (z_0/B_0)L^*$. If we take the large-scale Elsässer field as a reference value, $z_0 \sim z_{\rm rms}$, then $W^* \sim L^*$; in general, however, z_0 may be correlated with L^* in a nontrivial way.

Motion

The typical motion of Elsässer vorticity structures can be inferred as follows. Partition the volume $\mathcal{V}$ into a top part $\mathcal{V}_t$ and bottom part $\mathcal{V}_b$ ($\mathcal{V}_t \cup \mathcal{V}_b = \mathcal{V}$, $\mathcal{V}_t \cap \mathcal{V}_b = \emptyset$), defined as regions with $\partial_3\omega^+ < 0$ and $\partial_3\omega^+ > 0$ respectively. Then the four integrals are equal:

$$\int_{\mathcal{V}_b} dV \left(\partial_t\omega^+ + \epsilon_{ij3}\partial_k\partial_i\phi^-\partial_k\partial_j\phi^+ - \eta\partial_k\partial_k\omega^+\right) = \int_{\mathcal{V}_b} dV B_0\partial_3\omega^+$$
$$= -\int_{\mathcal{V}_t} dV \left(\partial_t\omega^+ + \epsilon_{ij3}\partial_k\partial_i\phi^-\partial_k\partial_j\phi^+ - \eta\partial_k\partial_k\omega^+\right) = -\int_{\mathcal{V}_t} dV B_0\partial_3\omega^+ \geq 0\,. \quad (2.17)$$

Now consider a quasi-stationary structure, so that $\int_{\mathcal{V}} dV\partial_t\omega^+ = 0$. By virtue of Eq. 2.15, the nonlinear term and dissipative term cancel out after integration across $\mathcal{V}$. It is then reasonable to assume that the structure is relatively symmetric, so that both $\mathcal{V}_t$ and $\mathcal{V}_b$ are comparable in size and the nonlinear term and dissipative term cancel out separately in both halves. In this symmetric case, Eq. 2.17 requires that $\int_{\mathcal{V}_t} dV\partial_t\omega^+ < 0$ and $\int_{\mathcal{V}_b} dV\partial_t\omega^+ > 0$, i.e., the structure is decaying in the top half and growing in the bottom half, implying that it moves counter to the guide field. If we instead consider structures of negative amplitude, $\omega^+ < -\omega_{\rm thr}$, then the structure is also found to move counter to the guide field. Therefore, any structures in ω^+, regardless of sign, tend to move counter to the guide field. For structures in ω^-, the B_0 term is flipped and so structures will tend to move in the direction of the guide field. Assuming a symmetric and quasi-stationary structure, the characteristic

velocity v^* for motion along the guide field is estimated by

$$v^* \sim \frac{\int_{\mathcal{V}_b} dV \partial_t \omega^+}{\int_{\mathcal{V}_b} dV \partial_3 \omega^+} = B_0 \,. \tag{2.18}$$

Hence, Elsässer vorticity structures propogate along the background field at the Alfvén velocity. Since structures in j and ω are superpositions of $\omega^{\pm}$ structures, they will correspondingly have Alfvénic growth, although with no net motion (on average).

3 METHODOLOGY: STATISTICAL ANALYSIS OF STRUCTURES

3.1 Identification of spatial structures

In this chapter, we describe the framework for our statistical analysis of intermittent structures and spatiotemporal processes. We first describe the methodology and measurements for the analysis of spatial structures, which is later applied for the spatial analysis of current sheets in numerical simulations of MHD turbulence in Chapter 5. We then extend this methodology for the analysis of intermittent spatiotemporal processes, which is applied for the temporal analysis in Chapter 6.

For simplicity, we focus on the identification of structures in numerical simulations. In contrast, for most experimental and observational scenarios, the available information is necessarily limited, either having reduced dimensionality (e.g., 1D temporal measurements from spacecraft in the solar wind, or 2D spatial emission profiles from images of the solar corona) or lacking direct measurements of key quantities (e.g., the local energy dissipation rate in the solar corona, which must instead be inferred from emissions). This makes it challenging, if not impossible, to infer full information about the structures from observations. Simulations, on the other hand, have a decisive advantage in that all information is, in principle, immediately available.

The identification and characterization of coherent structures is a significant industry in the hydrodynamic community, being applied mainly to transient vortices in 2D turbulence (McWilliams, 1990; Carnevale et al., 1991; McWilliams et al., 1999; Pasquero et al., 2002; Whitcher et al., 2008) and intermittent vorticity filaments in 3D turbulence (Jiménez et al., 1993; Jimenez and Wray, 1998; Moisy and Jiménez, 2004; Leung et al., 2012). The general consensus is that there is no unique, ideal way to identify vorticity filaments (Kida and Miura, 1998; Kolář, 2007). However, some criteria for a robust statistical analysis include:

- Large sample size of well-defined (smooth, localized, coherent) structures.

- Insensitivity to threshold parameters (or other methodological parameters).
- Insensitivity to specific methods for identification and characterization of structures.
- Computational efficiency of numerical algorithms.

We employ one of the simplest conceivable methods for identifying structures, being based on isosurfaces of the field. For concreteness, we consider structures in the current density $j(\boldsymbol{x})$, although other fields such as the vorticity $\omega(\boldsymbol{x})$ can be used as well. We define structures in the current density to be contiguous regions with points satisfying $|j| > j_{\rm thr}$, where $j_{\rm thr}$ is an imposed threshold, which is the only free methodological parameter. Ideally, the threshold should be relatively large, e.g., $j_{\rm thr} \gg j_{\rm rms}$, so that structures occupy well-defined regions and do not percolate through the system. Hence, a robust statistical analysis requires that the probability density function of field values, $P(j)$, extends to large values, which is satisfied by the non-Gaussian distributions associated with intermittent fields. Each structure is bounded by a closed isosurface at $|j| = j_{\rm thr}$, which can be used to characterize its morphology. Information about $j(\boldsymbol{x})$ across the interior volume is used to characterize other properties of the structures, including its energetics.

Formally, this framework for identifying structures is mathematically well-defined and suitably characterizes the morphological properties of the field, including implicit information about higher-order correlations (Mecke, 2000). However, some caution is required in interpretation of the results. Specifically, isosurfaces have some drawbacks, including:

- The threshold is an arbitrary parameter.
- Overlapping structures cannot be individually distinguished.
- There exists some threshold below which structures cannot be meaningfully probed.
- Other dynamical information, e.g., vector aspects of the field and correlations with other fields, is generally ignored.

On the other hand, constructing a more complex and informative method for identifying structures must typically be designed with some ad-hoc decisions. Since there is always some ambiguity in the concept of a coherent structure, especially in turbulence, it is not clear that investing in a more complex identification scheme will pay off. In this thesis, we prefer a simple and straightforward, rather than elaborate, methodology.

The identification scheme may affect the measured characteristics for any given structure. It may determine, for example, whether two nearby, partially-overlapping structures are resolved as a single structure or as two separate structures. Likewise, the threshold may have a similar effect. Moreover, in general, different methods for measuring the properties of the structure, such as its characteristic scales, may give conflicting answers. However, the statistical conclusions should be, and in our experience are found to be, broadly consistent regardless of the identification scheme, threshold, and measurement techniques. Consistency is an important condition for any successful statistical analysis of structures. As long as the structures are well-defined objects, and the methods are reasonably constructed, we conjecture that different methods will give consistent results.

One drawback of this identification method is the fact that the threshold parameter must be arbitrarily specified. Some structures may not be well-resolved at the given threshold; indeed, in practice, a large fraction of the identified structures are under-resolved, due to their peaks being near the threshold. These structures do not exhibit robust scaling relations and should be carefully ignored. Fortunately, they only appear as noise in the low-amplitude, small-scale regime of parameter space and generally have a negligible contribution to the total energy dissipated and volume occupied by the structures. To some extent, under-resolved structures are inevitable since there will always be a population of small, short-lived structures that barely cross the detection criteria. Filtering procedures can be applied to remove the population of under-resolved structures, but for simplicity we do not apply any filtering for most of the analysis.

Another drawback is that the threshold methodology does not easily distinguish between overlapping (i.e., superimposed) structures. This does not seem to be a

serious issue, however, since overlapping structures may be rather rare, and it is unclear to what extent they should be treated as separate structures in any case, due to their mutual interactions.

A notable alternative identification scheme for current sheets was used in Zhdankin et al. (2013). In this alternative scheme, structures were identified by finding local peaks in current density and then taking a threshold (separately for each individual structure) to be half of that local peak current density. In many ways, this alternative scheme is more appropriate than the fixed-threshold one adopted in this thesis, since it better represents the structures that would otherwise barely exceed the threshold. However, there are some shortcomings with this alternative scheme. One issue is that it is unclear how to treat overlapping structures, i.e., peaks that are in the vicinity of larger peaks and give coinciding volumes. A second issue is that the local peak current density may be sensitive to chaotic fluctuations. A third issue is that it is nontrivial to efficiently extend this methodology to spatiotemporal structures. Regardless, the statistical results previously presented in Zhdankin et al. (2013) are very similar to the results discussed in this thesis, supporting the conjecture that the statistical analysis methodology is insensitive to methods.

Numerical algorithm for identification

To identify structures on the lattice of a 3D simulation, we find sets of spatially-connected points (i.e., clusters) satisfying $|j| > j_{\rm thr}$, where two points on the lattice are considered spatially-connected if they are separated by strictly less than 2 lattice spacings, i.e., one is contained in the other's 26 nearest neighbors. The numerical algorithm scans the lattice for points with $|j| > j_{\rm thr}$. For each such point found, an array is constructed to store the constituent points of the structure. The neighboring points satisfying $|j| > j_{\rm thr}$ are identified and its coordinates are added to this array; this is then repeated for neighbors of those neighboring points, and so on, until no more points remain. The array containing the coordinates of all constituent points of the stucture is then stored for later use, and then the rest of the lattice is scanned for any additional structures (while ignoring the points already found to belong to

a structure). Each structure is therefore associated with an array containing the coordinates of its constituent points. Once every structure in a snapshot is identified, measurements are performed (as described in the next section) and stored for later use.

3.2 Measurements for dissipative current sheets

Energy dissipation rate

Once each structure in the current density is identified, we can immediately measure its volume, V, by counting the number of constituent points and multiplying it by the lattice volume element. We can also measure its resistive energy dissipation rate,

$$\mathcal{E} = \int dV \eta j^2 \,, \tag{3.1}$$

where integration is performed across the volume of the given structure.

Discrete quantities

Although not the focus of this work, structures can be characterized by some discrete properties. Perhaps the most important example is the number of topological features such as magnetic X-points or O-points, due their role in magnetic reconnection and particle acceleration. Indeed, X-points were the focus of several numerical studies of turbulence in 2D MHD and RMHD (Servidio et al., 2009, 2010; Zhdankin et al., 2013; Wan et al., 2014). These studies found that current sheets in RMHD do not, in general, coincide with X-points (and vice-versa). However, the strongest current sheets have a higher tendency to contain X-points and may therefore be associated with reconnection. It is, however, unclear how to best characterize magnetic reconnection in a fully 3D system, since magnetic nulls are not required for reconnection (e.g., Priest and Démoulin, 1995; Parnell et al., 2010; Haynes and Parnell, 2010; Pontin, 2011). Other examples of discrete properties include the direction of the current flow

and the Euler characteristic (i.e., genus). For the present work, we do not consider these discrete properties, although they are potential topics for future research.

Characteristic scales

We now describe the methods used for determining the morphology, i.e., characteristic scales, of structures. Ignoring the finer features, each structure can be characterized by three scales. These are the length L, width W, and thickness T, with $L \geq W \geq T$.

For current sheets in MHD turbulence, the length is generally aligned with the guide field, while the width and thickness are associated with the anisotropy in the perpendicular plane. This fact was exploited in Zhdankin et al. (2013) to measure the scales of current sheets in RMHD. In that work, the length was taken to be the distance between the constituent points with the smallest and the largest z coordinates, while the thickness and width were measured in the xy plane containing the point of peak current density in the structure. Width was taken to be the largest distance between constituent points in this plane, while thickness was measured in the direction of steepest descent from the peak (determined from the eigenvectors of the Hessian matrix). In this thesis, we use more general methods which do not rely on the anisotropy of RMHD, and hence, can be applied to a broader class of systems.

As a consistency check, we use two different methods based on distinct definitions for the characteristic scales. The first method is based on the direct measurement of distance across the structure in three orthogonal directions, while the second method is based on the ratios of the Minkowski functionals (Kerscher, 2000). We refer to these as the Euclidean scales and the Minkowski scales, respectively.

Euclidean method

We first describe the Euclidean method. The Euclidean scales are intuitive, direct measurements of the scale across certain parts of the structure, which may be misleading for irregular morphologies. For example, structures with an S-shaped cross-section may be inaccurately described, since, as we will see, the thickness would be measured along the elongated part of the S.

For length L_e, we take the maximum distance between any two points in the structure. Although very straightforward to measure, this can be computationally inefficient for large structures, scaling as $\mathcal{O}(n^2)$, where n is the number of points in the structure. A quicker estimate is obtained by finding the point in the structure which is furthest from the point of peak amplitude (i.e., the location of the local current density maximum), and then identifying the largest distance between this point and any other point in the structure. This second method scales as $\mathcal{O}(n)$, and will be used to obtain most of the results.

For width W_e, we consider the plane orthogonal to the length and coinciding with the point of peak amplitude. We then take the maximum distance between any two points of the structure in this plane (with allowed offset of less than the lattice spacing from the plane) to be the width. The direction for thickness T_e is then set to be orthogonal to length and width. We take the thickness to be the distance across the structure in this direction through the point of peak amplitude. Since typical thicknesses may be comparable to the lattice spacing, we use a linear interpolation scheme to obtain finer measurements.

Minkowski method

We now describe the Minkowski method, which has previously been applied to study the morphology of large-scale structures in the universe (Schmalzing et al., 1999), coherent structures in the kinematic dynamo (Wilkin et al., 2007), and vorticity filaments in hydrodynamic turbulence (Leung et al., 2012). The Minkowski scales are mathematically rigorous measurements which take into account information about the entire structure. Hence, the Minkowsi scales may be well suited for complex morphologies, but often elude a straightforward physical interpretation.

By Hadwiger's theorem, the morphology of an object in d-dimensional space is completely characterized by the set of $d + 1$ numbers known as the Minkowski functionals (Mecke, 2000)[1]. In 3D space, the first three Minkowski functionals are

[1]However, the much larger set of Minkowski tensors is required to fully describe the orientation and anisotropy of objects (Schröder-Turk et al., 2013)

given by

$$V_0 = V = \int dV$$
$$V_1 = \frac{A}{6} = \frac{1}{6}\int dS$$
$$V_2 = \frac{H}{3\pi} = -\frac{1}{6\pi}\int dS \nabla \cdot \hat{n}\,, \tag{3.2}$$

where V is volume, A is surface area, and H is the mean curvature on the surface (and $\hat{n} = -\nabla j/|\nabla j|$ is the surface normal, assuming structures in the current density). The fourth Minkowski functional is $V_3 = \chi$, the Euler characteristic (obtained from the mean Gaussian curvature), which will not be used here since it is dimensionless. Three quantities with the dimensions of length are formed from ratios of these functionals,

$$L_m = \frac{3V_2}{4}$$
$$W_m = \frac{2V_1}{\pi V_2}$$
$$T_m = \frac{V_0}{2V_1}\,. \tag{3.3}$$

These scales are normalized such that when applied to a sphere, all scales equal the radius. The Minkowski functionals satisfy the isoperimetric inequalities (Schmalzing et al., 1999):

$$S^2 \geq 3VH$$
$$H^2 \geq 4\pi S\chi\,, \tag{3.4}$$

from which $L_m > W_m > T_m$ follows. For simple convex objects, these three scales have the usual interpretation of length, width, and thickness.

To compute the Minkowski functionals on the simulation lattice, we employ Crofton's formula, which is a numerical approximation for the Minkowski functionals based on counting the number of lattice points N_0, lattice edges N_1, lattice faces N_2, and lattice cubes N_3 that constitute the structure (see, e.g., Schmalzing and Buchert,

1997, for details). Explicitly, Crofton's formula for an isotropic lattice, with lattice spacing h, is:

$$\begin{aligned} V_0 &= h^3 N_3 \\ V_1 &= h^2 \left(-\frac{2}{3} N_3 + \frac{2}{9} N_2 \right) \\ V_2 &= h \left(\frac{2}{3} N_3 - \frac{4}{9} N_2 + \frac{2}{9} N_1 \right) \\ V_3 &= -N_3 + N_2 - N_1 + N_0 \,. \end{aligned} \tag{3.5}$$

In order to apply Crofton's formula on the elongated lattice in our RMHD simulations, we treat each lattice element as a composite of isotropic lattice elements. Accuracy of the Crofton method was established on low-resolution (512^3) simulations by comparing it with another numerical method, based on Koenderink invariants, also discussed in Schmalzing and Buchert (1997).

3.3 Extension to temporal realm: dissipative processes

General remarks

We now describe the methodology for the temporal analysis of intermittent structures, i.e., for the statistical analysis of spatiotemporal dissipative processes. In essence, this methodology extends the identification scheme used for 3D spatial dissipative structures (current sheets) to 4D spatiotemporal dissipative processes (flare events).

It is straightforward in principle to extend the previous procedures into the temporal realm by applying the same threshold criterion to the 4D spatiotemporal field $j(\boldsymbol{x}, t)$. However, although simple in principle, it is challenging in practice to analyze a high-resolution 4D data set in this way. Assuming that the analysis is applied to post-processed data from well-resolved simulations stored on a computer system, the data storage conditions limit the total number of available snapshots,

negatively affecting the possible time cadence of snapshots and size of the overall time interval. Hence, the time resolution of post-processed data must generally be worse than the internal time resolution of the simulation. This is a serious issue since the data must be well-resolved in all dimensions in order to properly resolve and track structures across a wide range of scales.

A related problem is that the primary memory limits the amount of data that can be loaded by the analysis program at any given time, requiring the numerical procedures to work with small pieces of the overall data set at a time. Therefore, a feasible temporal analysis should be based on first identifying the structures in the spatial dimensions of a given snapshot, and then tracking them through time, from their formation to their destruction. The algorithms required to perform this task are rather complex, and must be designed in a robust and efficient manner. In particular, there needs to be an algorithm that accurately associates structures in one snapshot with their time-evolved counterparts in subsequent snapshots. A fundamental challenge here lies in the fact that there may not be a unique correspondence between a structure in one snapshot and a structure in the adjacent snapshot, due to mergers and divisions.

The interactions between structures cause the notion of a coherent time-evolving structure to be ambiguous. Instead, the objects of central importance are the processes involving structures. These processes can be variously thought of as sets of interacting structures, as dissipative events, or as flares (if we equate the dissipated energy with outgoing radiation). More generally, they can be thought of as branched spatiotemporal structures.

Classification of processes

In order to build an intuition and facilitate the subsequent discussion of processes, we now describe a convenient classification scheme for processes. This allows processes to be visualized diagrammatically, which has some superficial similarities to Feynman diagrams for quantum mechanical scattering processes (Feynman, 1948); however, none of the mathematical symmetries characterized by the Feynman rules carry

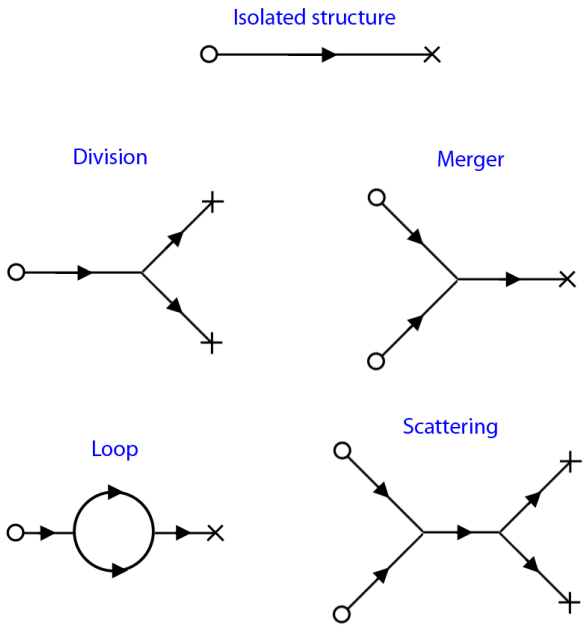

Figure 3.1: Diagrams of some simple processes, where formation is represented by O, interaction by a vertex, and destruction by X. An isolated structure is a process with no vertices. Division and merger processes are the next simplest case, with a single vertex each. Higher-order processes such as loops and scatterings have a larger number of vertices or vertices with more paths.

over, since, to the best of our knowledge, isosurfaces in the current density described by the MHD equations contain no conserved quantities. Regardless, the following classification scheme is a simple way to describe processes and their complexity.

We first introduce some terminology. We define a state to be an individual spatial structure at fixed time, which represents the basic building block of processes. We assume that the states are given at times spaced by an infinitesimal increment dt. We also assume that there exists a map between all states at any time t to other states at time $t - dt$ and $t + dt$, which represents the instantaneous temporal evolution of structures from one state to another state. We define a path segment to be a bijective (i.e., one-to-one) sequence of states under this map, which represents the coherent temporal evolution of an individual structure while it does not interact with

any other structures. We then define a path to be a path segment with bijectivity breaking down only at the initial and final states in the sequence. A process is then described as a set of paths that are (non-bijectively) connected at their endpoints, which represents a set of interacting structures.

Diagrams of some simple conceivable processes are shown in Fig. 3.1. Here, we represent paths schematically as lines with an arrow marking the direction of time. If the path begins by spontaneous formation, i.e., from a peak that grows to exceed the detection threshold, then we mark the beginning of the path with an O. If the path ends by spontaneous destruction, i.e., from a structure that recedes below the detection threshold, then we mark the end of the path with an X. The third possibility is for the path to start or end with an interaction. Interactions between structures are represented by vertices connecting sets of three (or more) paths. A process schematically consists of a set of paths connected by a set of vertices.

The simplest process is the evolution of an isolated structure, i.e., a structure that is formed and then destroyed without interactions. Isolated structures are described by a single path and have well-defined histories with well-defined properties. Other structures undergo at least one interaction. The two simplest processes involving an interaction are the division of one structure into two structures and the merger of two structures into one structure. Since an interaction is non-bijective, the structures in these processes do not have completely well-defined histories, so many of the quantities used to describe isolated structures are ambiguous. However, we will see that a meaningful set of more general characteristics can be introduced.

We claim that the most logical approach for a temporal analysis is to study processes rather than individual spatially-coherent structures, i.e., paths, which lose their identity upon interacting. This is also the most conservative approach, as it requires no fundamental changes to the methodology used for the statistical analysis of spatial structures at fixed time, and requires no ad-hoc assumptions to treat the interactions. We also find that the statistical trends are more robust for processes rather than paths.

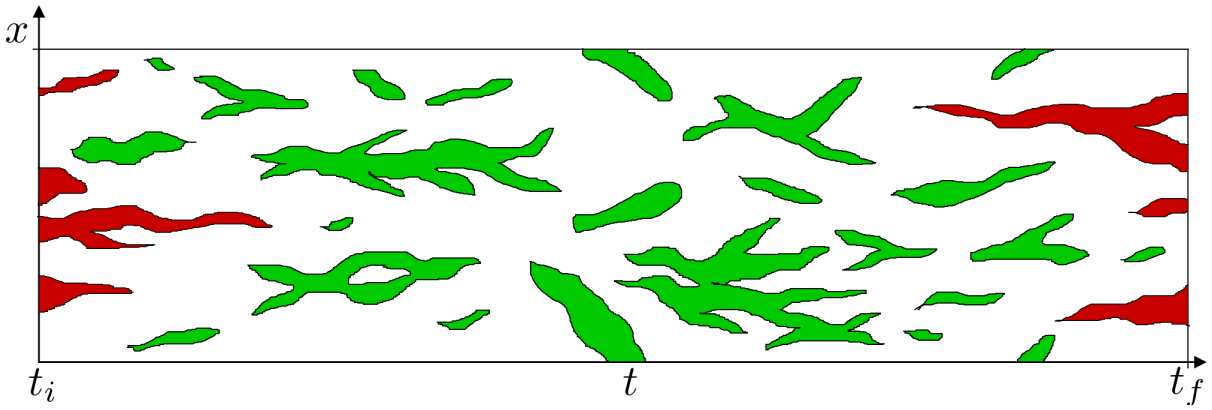

Figure 3.2: A schematic of structures evolving in time, highlighted in green (shown in one-dimensional space for clarity). Structures from the initial and final states are marked in red.

3.4 Methods for temporal analysis

Outline of procedure

In this section, we describe our algorithms for the temporal analysis. Since the procedure in its entirety is rather complicated, we include a brief outline in this subsection. A more detailed description is presented in the rest of this section. The procedure rests on a hierarchy of steps: first, we find sets of contiguous points (above the threshold) in each snapshot to obtain the spatial structures; next, we find sets of bijectively-connected states to obtain the paths; finally, we find sets of connected paths to obtain the processes. A schematic of the final result is shown in Fig. 3.2, where processes (colored in green) of varying complexity are identified on the space-time lattice.

1. Identify all states (i.e., spatial structures) in each snapshot, and represent temporal connectivity by constructing a map between states in adjacent snapshots.

    a) Load initial snapshot and determine states (by using threshold algorithm).

        - Store constituent points of each state in a temporary array;

- Perform measurements on states and store in a permanent array;

b) For $i = 2, \ldots, N_{\text{snap}}$, do following:

- Load ith snapshot, determine states, and store constituent points and measurements;
- Construct the evolution map, which associates states in snapshot $i-1$ with temporally-connected states in snapshot i, and vice-versa (do this by comparing constituent points of structures in both snapshots); remove temporary array for snapshot $i-1$;

2. Identify paths.

a) Obtain paths from states that form a bijective sequence under the evolution maps.

b) Perform measurements on paths by referencing the constituent states.

c) For each path, construct (non-bijective) map that identifies other paths connected to it.

3. Identify processes.

a) Obtain processes from sets of connected paths.

b) Perform measurements on processes by referencing the constituent paths.

c) Treat processes that exist during the initial snapshot or final snapshot as special cases (incomplete processes).

Identification of states (spatial structures)

The first step of our procedure is to identify the states in each snapshot, i.e., the spatial structures at fixed times. As before, states are defined as spatially-connected sets of points with current density magnitudes exceeding a fixed threshold, j_{thr}. Since our algorithm for identifying states is the same as in the spatial analysis, we defer the reader to Sec. 3.1 for details. Once every state in a snapshot is identified, the constituent points and other measurements are stored for later use.

Temporal association between states in adjacent snapshots

In this subsection, we describe the algorithm for identifying the time-evolved counterparts of a state, i.e., the states in the adjacent snapshots that represent the evolved structure. The result is a (non-bijective) map associating the set of states in one snapshot with the set of states in an adjacent snapshot, representing the instantaneous temporal evolution of structures.

Consider a given state in the kth snapshot. To find the future counterparts of the given state, we iterate through all states in the subsequent snapshot and determine which ones have any constituent points that are spatially-connected to the given state. In other words, we look for states with points that coincide with or neighbor any of the given state's points (using the 26 nearest neighbor criterion). Any such states are identified as future counterparts of the given state.

We suppose that the states in each snapshot are identified by an index $i \in \{1, 2, \ldots, N_k\}$, where N_k is the number of states in the snapshot. We construct an array that stores the indices of the corresponding future states in the $(k+1)$th snapshot, which we call the forward evolution map $T_k^+(i)$ where $i = 1, 2, \ldots, N_k$. Thus, if the ith state in snapshot k is associated with the jth state in snapshot $k+1$, then $T_k^+(i) = j$. If the ith state has no future counterparts, then we assign $T_k^+(i) = 0$, representing the null state. If the ith state is associated to multiple future states (i.e. it divides), then we assign $T_k^+(i)$ multiple values containing all of these future states.

We perform a similar procedure to find the past counterparts of the given state. In this case, we iterate through all states in the preceding snapshot to determine which ones have points that are spatially-connected to the given state. Any such states are identified as past counterparts of the given state. Likewise, we construct a backward evolution map, $T_k^-(i)$, which identifies state i in the kth snapshot with its corresponding past counterparts in the $(k-1)$th snapshot. If the ith state has no past counterpart, then we assign $T_k^-(i) = 0$. If the ith state is associated to multiple past states (i.e. it results from a merger), then we assign $T_k^-(i)$ multiple values containing all of these past states.

The entire set of evolution maps $T_k^{\pm}$ where $k = 1, \ldots, N_{\text{snap}}$ is constructed by

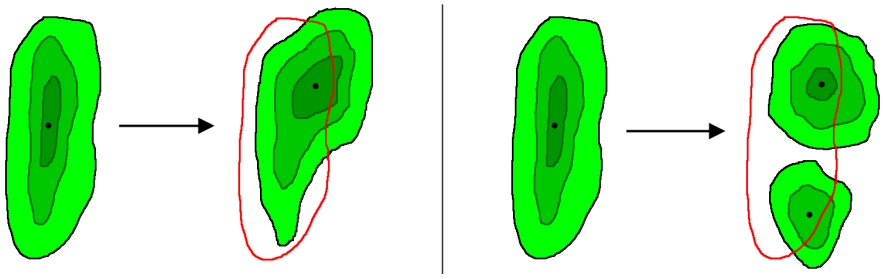

Figure 3.3: Schematic of structure evolution, shown in 2D space for clarity. The procedure stores the constituent points of the present state, checks the future snapshot for any states with points that are spatially-connected to the present state's points, and then identifies these states as future counterparts of the present state. In the left panel, a structure evolves without interacting. In the right panel, a structure divides, having multiple future counterparts. This procedure is reversed in time to determine past counterparts, with a merger occuring for multiple past counterparts.

iterating through the snapshots and applying the above procedure immediately after identifying the states in pairs of consecutive snapshots. After $T_k^{\pm}$ is constructed for all N_k states in a given snapshot k, the array containing the constituent points of the states is deleted to free up memory before loading the next snapshot.

Identification of paths (tracking algorithm)

In this subsection, we describe the algorithm for identifying paths across multiple snapshots, which is an important intermediate step before processes themselves can be identified. A path is abstractly defined as a sequence of states that is bijectively-connected under the evolution maps (see Sec. 3.3). From the algorithms in the preceding subsections, we have a sequence of $N_{\rm snap}$ snapshots (denoted by index k), each with a set of N_k states, along with the evolution maps $T_k^{\pm}$ associating the states in each snapshot with their time-evolved counterparts in adjacent snapshots. To identify paths, we must find the bijective sequences in $\{T_k^{\pm}\}$.

Consider the ith state in snapshot k. Bijectivity of the forward evolution map is satisfied if there exists a unique state j in snapshot $k+1$ such that $T_k^{+}(i) = j$ and $T_{k+1}^{-}(j) = i$. Any two states satisfying this condition form a path segment. If this

condition fails, however, then state i is the endpoint of a path. This happens either when the structure is destroyed ($T_k^+(i) = 0$) or when it interacts (either $T_k^+(i)$ or $T_{k+1}^-(j)$ is multi-valued). Likewise, if there exists a unique state l in snapshot $k-1$ such that $T_k^-(i) = l$ and $T_{k-1}^+(l) = i$, then these two states form a path segment; otherwise state i is the beginning of a path due to either formation ($T_k^-(i) = 0$) or an interaction (either $T_k^-(i)$ or $T_{k-1}^+(l)$ is multi-valued). Using these conditions, we can track the state of any given structure along a path through a sequence of snapshots, until an interaction is encountered.

We iterate through the states in all N_{snap} snapshots and use the above tracking procedure to identify the associated path and its constituent states, marking those states so that they are ignored in the remaining iterations. As a result, we obtain a set of N_{path} paths. For each path, we construct an array which contains the indices of the constituent states, which is referenced to perform measurements on the path. We also construct an array containing the indices of the predecessors, which are the other paths connecting to it from the beginning of the path. The predecessors are determined by operating with T^- on the first state of the path to obtain all of the past states, and finding the paths that contain these past states. In a separate array, we store the indices of successors, which are the other paths connecting to the end of the path, obtained by operating with T^+ on the final state of the path. The predecessors and successors of paths characterize the vertices between paths. Note that if the number of predecessors is zero, then the path is formed spontaneously. If the number of successors is zero, then the path is destroyed spontaneously.

Identification of processes

Finally, we describe how to identify processes from the set of paths and their predecessors and successors. Recall that processes are described as sets of connected paths. Therefore, we first iterate through the set of paths. For each path, iterate through the predecessors and successors of the path, and then through the predecessors and successors of those, and so on, until no new paths can be obtained. The set of paths acquired in this way constitute a single process, and their indices are stored in an

array corresponding to that process. The paths that have already been identified as belonging to a process are ignored in the remaining iterations of paths.

Some processes will contain states from the initial snapshot or in the final snapshot of the dataset, which we call initial processes or final processes, respectively. These processes must be treated as special cases, since our information about them is incomplete. The simplest treatments of these processes are either to ignore them or to treat them as normal processes undergoing formation or destruction in the initial or final snapshots. For most of our analysis, we will ignore initial and final processes. However, they are included in the probability distributions for better statistics at long durations. Due to the relatively long interval of time in our simulations, the initial and final processes are a very minor contribution to the statistics, unless low thresholds are used.

This concludes our discussion of the algorithms used to identify processes. We now have a sample of N_{proc} processes, each including an array of constituent paths. The paths contain all of the information necessary to perform measurements on the processes. These measurements are described in the next section.

3.5 Measurements for temporal analysis

Measurements for paths

In this subsection, we describe measurements for paths, which are conceptually simpler than those for processes due to the bijectivity condition. These measurements will be used and generalized in the next subsection to characterize processes.

The evolution of a path can be described by the time-series $\mathcal{E}(t)$, $V(t)$, $L(t)$, $W(t)$, and $T(t)$ of instantaneous characteristics defined for the constituent states. For simplicity, we use the Euclidean method to measure the spatial scales of states. Consider a path given by a sequence of states at times t_k, where $k \in \{1, \ldots, N_{\text{s}}\}$ and N_{s} is the number of constituent states. Assuming a fixed cadence of snapshots, the states are separated by a fixed time interval Δt. The kth state has characteristics denoted by $\mathcal{E}_k$, V_k, L_k, W_k, and T_k.

One of the most basic properties of a path is its duration (or lifetime) τ, defined as

$$\tau = t_{N_s} - t_1 = (N_s - 1)\Delta t \,. \tag{3.6}$$

The energy dissipation rate of states generalizes to the dissipated energy,

$$E = \int dt \mathcal{E}(t) = \sum_{k=1}^{N_s} \mathcal{E}_k \Delta t \,, \tag{3.7}$$

where time integration is performed over the duration of the path. We also define the peak volume, peak energy dissipation rate, maximum length, maximum width, and maximum thickness as

$$\begin{aligned} V_{\max} &= \max(V(t)) = \max(\{V_k\}) \\ \mathcal{E}_{\max} &= \max(\mathcal{E}(t)) = \max(\{\mathcal{E}_k\}) \\ L_{\max} &= \max\left(L(t)\right) = \max(\{L_k\}) \\ W_{\max} &= \max\left(W(t)\right) = \max(\{W_k\}) \\ T_{\max} &= \max\left(T(t)\right) = \max(\{T_k\}) \,. \end{aligned} \tag{3.8}$$

Note that as an alternative to these local quantities, we can consider time-averaged quantities; these are, however, less easily generalized for processes.

Measurements for processes

We now describe how to generalize the quantities defined for paths in the previous section to processes, i.e., sets of interacting structures. We characterize each process by the number of constituent paths, N_p. Processes with a single path, $N_p = 1$, are isolated structures. Processes with three paths, $N_p = 3$, are division or merger processes. Processes consisting of more than three paths, $N_p > 3$, are higher-order processes, containing either more than one vertex or vertices joining more than three paths. Other related measures of the complexity of a process include the number of

vertices N_v, the number of constituent states N_s, the number of internal paths N_{int} (i.e. paths that begin and end in vertices), and the number of incoming paths N_{in} or outgoing paths N_{out}.

Consider a process with constituent paths enumerated by index $n = 1, \ldots, N_p$, extending from initial times t_n to final times t'_n. Let E_n, $V_{\text{max},n}$, $\mathcal{E}_{\text{max},n}$, $L_{\text{max},n}$, $W_{\text{max},n}$, and $L_{\text{max},n}$ be the characteristics of the nth path as defined in the previous subsection. We define the process duration by

$$\tau = \max(\{t'_n\}) - \min(\{t_n\})\,, \tag{3.9}$$

which is simply the time interval from the formation of the first existing constituent path to the destruction of the last existing constituent path. The dissipated energy E of a process is defined by integrating ηj^2 across the enclosed 4D spacetime region. This is given by

$$E = \sum_{n=1}^{N_p} E_n\,. \tag{3.10}$$

Likewise, we can define the peak volume and peak energy dissipation rate as the maximum of the peaks corresponding to the constituent paths,

$$\begin{aligned} V_{\text{max}} &= \max(\{V_{\text{max},n}\}) \\ \mathcal{E}_{\text{max}} &= \max(\{\mathcal{E}_{\text{max},n}\})\,. \end{aligned} \tag{3.11}$$

Note that an alternative definition for V_{max} ($\mathcal{E}_{\text{max}}$) can be based on the maximum of the volume (energy dissipation rate) summed for all states belonging to the process at any given time. These two definitions may differ for processes with a large number of paths, but will otherwise give similar results; we use the first definition only for simplicity. The most difficult quantities to generalize for a process are the characteristic spatial scales. There appears to be no universally satisfactory way to obtain average characteristic scales for a general configuration with many paths. If we apply an average across all paths (or all states) constituting the process, then

the result may be skewed toward unphysical short-lived paths (or states). A simpler alternative is to take the maximum scale corresponding to any path in the process,

$$\begin{aligned} L_{\max} &= \max(\{L_{\max,n}\}) \\ W_{\max} &= \max(\{W_{\max,n}\}) \\ T_{\max} &= \max(\{T_{\max,n}\})\,. \end{aligned} \tag{3.12}$$

One alternative possible definition for the spatial scales, which gives results consistent with the definition that we apply, is to take the spatial scales from the largest state at the moment of the peak energy dissipation rate.

This concludes the discussion of the methods for our statistical analysis of intermittent structures. In the next three chapters, we will describe the results from applying this methodology to MHD turbulence.

4 STATISTICS OF LOCAL ENERGY DISSIPATION

This chapter is a prelude to our statistical analysis of intermittent dissipative structures, setting the stage by establishing the statistics of the local energy dissipation rate in MHD turbulence. We first describe our numerical simulations in Sec. 4.1. We then describe the cumulative distribution of the energy dissipation, and the volume filling fraction of structures, in Sec. 4.2, the correlations between current density and vorticity in Sec. 4.3, and finally, the statistics of coarse-grained energy dissipation in Sec. 4.4, which is found to be well approximated by the log-normal model.

4.1 Numerical simulations

The analysis in this thesis is performed on numerical simulations of strong MHD turbulence in the RMHD approximation (see Sec. 2.1 for the relevant equations). Thus, a strong uniform background field $\boldsymbol{B}_0 = B_0\hat{\boldsymbol{z}}$ is assumed; specifically, we take $B_0/b_{\rm rms} \approx 5$, where $b_{\rm rms}$ is the root-mean-square average of the fluctuating component[1]. As is conventional, turbulence is driven at large scales in a periodic box; the energy then cascades through a relatively short inertial range until it is lost in the dissipation range. The reader may refer to (Perez and Boldyrev, 2010; Perez et al., 2012) for additional details on simulations.

The RMHD equations are solved in a periodic, rectangular domain of size $L_\perp = 2\pi$ perpendicular to the guide field and size $L_\parallel = 6L_\perp$ parallel to the guide field. The turbulence is driven at the largest scales by colliding Alfvén modes, excited by statistically independent random forces $\boldsymbol{f}^+$ and $\boldsymbol{f}^-$ in Fourier space at low wavenumbers $2\pi/L_\perp \le k_{x,y} \le 2(2\pi/L_\perp)$, $k_z = 2\pi/L_\parallel$. The Fourier coefficients of $\boldsymbol{f}^\pm$ in this range are Gaussian random numbers with amplitudes chosen so that $b_{\rm rms} \sim v_{\rm rms} \sim 1$. The forcing is solenoidal in the perpendicular plane and has no component along $\boldsymbol{B}_0$. The random values of the different Fourier components of the forces are refreshed

[1]The RMHD equations have a scaling symmetry such that if B_0 and the z coordinates are rescaled so that $B_0/L_\parallel$ is fixed, then the dynamics are unchanged. Hence, the magnitude of the guide field is actually arbitrary in this sense.

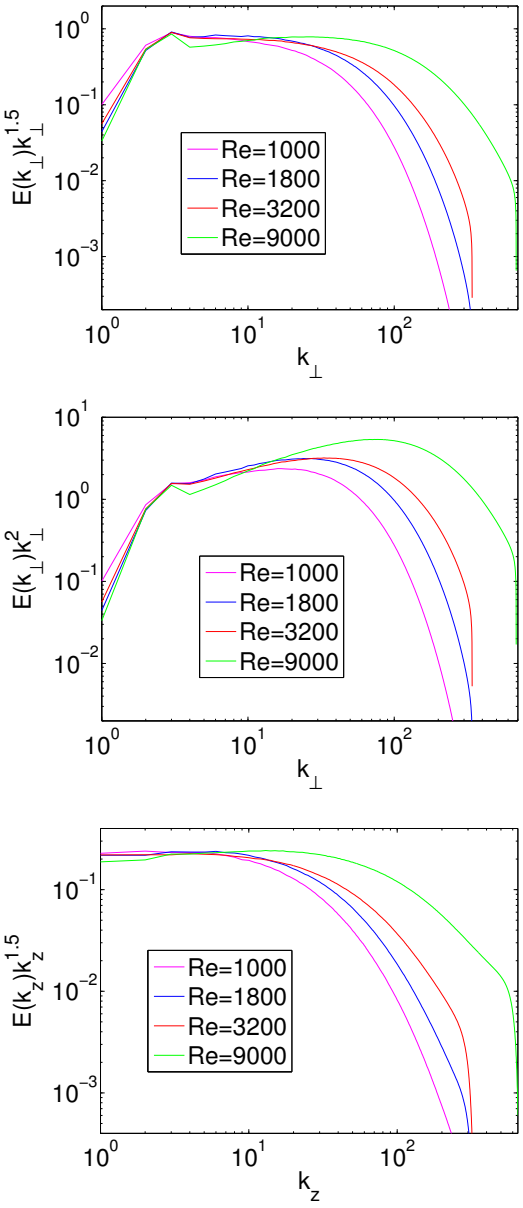

Figure 4.1: Top: Energy spectrum for perpendicular fluctuations in the magnetic field, compensated by $k_\perp^{3/2}$, for $Re = 1000$ (magenta), $Re = 1800$ (blue), $Re = 3200$ (red), and $Re = 9000$ (green). Center: Same spectrum compensated by $k_\perp^2$, representing the current density fluctuations. Bottom: Energy spectrum for magnetic field fluctuations in the z direction, compensated by $k_z^{3/2}$.

independently on average about 10 times per eddy turnover time. To perform the spatial discretization, a fully dealiased 3D pseudo-spectral algorithm is used.

The Reynolds number is given by $\mathrm{Re} = v_{\mathrm{rms}}(L_\perp/2\pi)/\nu$, which is equal to the magnetic Reynolds number, $\mathrm{Rm} = v_{\mathrm{rms}}(L_\perp/2\pi)/\eta$. Timescales are measured in terms of large-scale eddy turnover times of the turbulence, given by $\tau_{\mathrm{eddy}} = L_\perp/(2\pi v_{\mathrm{rms}}) \approx 1$. The analysis in this chapter and Chapter 5 is performed for roughly 15 snapshots (spaced at intervals of one eddy-turnover time during statistical steady state) for independent runs with $Re = 1000$, $Re = 1800$, and $Re = 3200$ on 1024^3 lattices, and also for 9 snapshots with $Re = 9000$ on a 2048^3 lattice. These simulations are listed in Table 4.1. In addition, analysis was performed on lower-resolution 512^3 simulations to establish numerical convergence of the simulations and the methods at $Re = 1800$. Simulations for the temporal analysis, which require hundreds of snapshots dumped at high cadence, are described separately in Sec. 6.2.

Table 4.1: Numerical simulations for spatial analysis

Case	Resolution	Re	Number of snapshots
1	1024^3	1000	14
2	1024^3	1800	15
3	1024^3	3200	15
4	2048^3	9000	9

For reference, in Fig. 4.1 we show the magnetic energy spectra for the given simulations. The first panel shows the perpendicular magnetic energy spectrum averaged over the given snapshots, compensated by $k_\perp^{3/2}$ expected from dynamic alignment (Boldyrev, 2005, 2006). The magnetic energy spectrum clearly exhibits an inertial range which increases in size with Re. By compensating by an additional factor of $k_\perp^{1/2}$, as shown in the second panel of Fig. 4.1, the energy spectrum for the current density is obtained, which is maximized at wavenumbers in the dissipation range. Hence, the energy spectra show that the bulk of energy dissipation occurs in smaller and smaller scales as Re increases, which is consistent with dissipation occurring in thin, intermittent structures. However, the energy spectra cannot be used to infer the morphology or overall size of the structures. We also show in Fig. 4.1

the magnetic energy spectrum in the z direction, compensated by $k_z^{3/2}$. As noted in previous studies, the energy spectrum along the global mean field better represents the perpendicular cascade rather than the parallel cascade, due to the bending of field lines causing the local mean field to deviate from the global mean field (Maron and Goldreich, 2001).

4.2 Distribution of energy dissipation rates

In this section, we describe the pointwise statistics of the energy dissipation rate. To compare the intermittency of energy dissipation between different simulations with varying parameters such as Re, we take the total resistive energy dissipation rate in the system as a reference value,

$$\mathcal{E}_{\rm tot} = \int d^3x \eta j^2 = V_{\rm tot} \eta j_{\rm rms}^2 \,, \tag{4.1}$$

where $V_{\rm tot}$ is the system volume. Note that $\mathcal{E}_{\rm tot}$ is fixed in the simulations. Hence, the rms current density, $j_{\rm rms} = \sqrt{\langle j^2 \rangle}$, increases with Re as $j_{\rm rms} = \sqrt{\mathcal{E}_{\rm tot}/\eta V_{\rm tot}} \propto Re^{1/2}$. In order to study the statistics of energy dissipation in a universal manner, it is natural to rescale the current density to the rms value, i.e., to use a fixed threshold $j_{\rm thr}/j_{\rm rms}$ when comparing structures in simulations with different Re.

To get a better sense of the concentration of dissipative structures in the simulations, we consider the cumulative resistive energy dissipation rate $\mathcal{E}_{\rm cum}(j_{\rm thr}/j_{\rm rms})$ and cumulative volume $V_{\rm cum}(j_{\rm thr}/j_{\rm rms})$ conditioned on the threshold $j_{\rm thr}/j_{\rm rms}$. In terms of probability density function for j, $P(j)$, these are defined by

$$\begin{aligned} \frac{\mathcal{E}_{\rm cum}(j_{\rm thr}/j_{\rm rms})}{\mathcal{E}_{\rm tot}} &= \frac{\int_{j_{\rm thr}}^{\infty} dj P(j) \eta j^2}{\int_0^{\infty} dj P(j) \eta j^2} \\ \frac{V_{\rm cum}(j_{\rm thr}/j_{\rm rms})}{V_{\rm tot}} &= \int_{j_{\rm thr}}^{\infty} dj P(j) \,. \end{aligned} \tag{4.2}$$

In essence, these quantities represent the energy dissipated and volume occupied by structures above a given threshold, i.e., at points with current densities $|j| > j_{\rm thr}$.

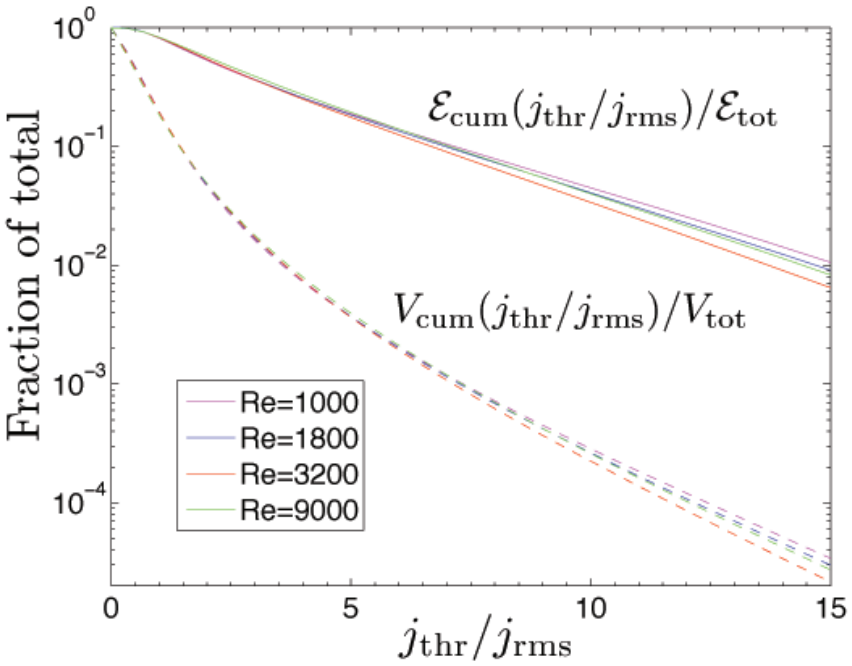

Figure 4.2: The fraction of overall resistive energy dissipation (solid lines) and fraction of total volume (dashed lines) accounted for by structures with current densities $|j| > j_{\rm thr}$. The colors correspond to $Re = 1000$ (magenta), $Re = 1800$ (blue), $Re = 3200$ (red), and $Re = 9000$ (green).

We show $\mathcal{E}_{\rm cum}(j_{\rm thr}/j_{\rm rms})/\mathcal{E}_{\rm tot}$ and $V_{\rm cum}(j_{\rm thr}/j_{\rm rms})/V_{\rm tot}$ in Fig. 4.2. These cumulative distributions show very little sensitivity to Re, suggesting that they may be universal. The fraction of volume occupied by structures with $|j| > j_{\rm thr}$ is always much smaller than the fraction of energy dissipated; for example, 40% of energy is dissipated in approximately 2% of the volume. Both quantities decay approximately exponentially at large $j_{\rm thr}/j_{\rm rms}$.

It is interesting to note that half of the resistive energy dissipation occurs in regions with current densities above $j_{\rm thr}/j_{\rm rms} \approx 2.2$, at which current sheets are still visibly very well-defined and occupy about 3% of the volume. Therefore, one can conclude that the majority of energy dissipation occurs in intermittent structures. In fact, structures can be discerned at thresholds all the way down to $j_{\rm thr} \sim j_{\rm rms}$

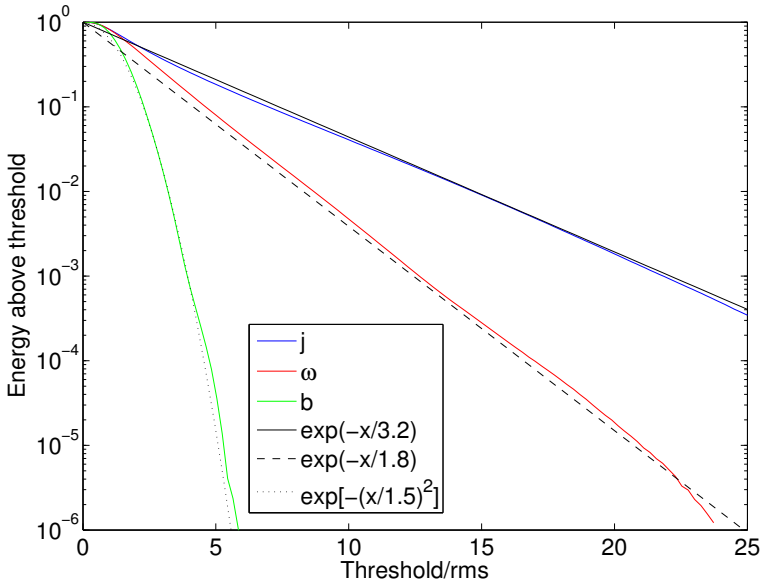

Figure 4.3: The fraction of overall resistive energy dissipation occurring at current densities $|j| > j_{\rm thr}$ (blue) and the fraction of overall viscous energy dissipation occurring at vorticities $|\omega| > \omega_{\rm thr}$ (red), with exponential fits (black). For comparison, the magnetic energy b^2 occurring at magnetic fields $|\boldsymbol{b}| > b_{\rm thr}$ is also shown (green).

(where they fill 20% of the volume and account for over 80% of the dissipation). Since a larger threshold is better suited for a statistical analysis of structures, most of the analysis in this thesis is performed at $j_{\rm thr}/j_{\rm rms} \sim 4$, which focuses on the most intense and well-defined dissipative structures, contributing around 30% of the overall resistive energy dissipation. This threshold is low enough to get a large sample of structures while being high enough to avoid many structures percolating through the domain and to avoid large numbers of overlapping structures.

The cumulative resistive energy dissipation can be fit rather well by an exponential, $\exp\left(-j_{\rm thr}/3.2j_{\rm rms}\right)$, as shown in Fig. 4.3. For comparison, we perform an analogous procedure on the vorticity ω, and find that the cumulative viscous energy dissipation decays more steeply with threshold $\omega_{\rm thr}/\omega_{\rm rms}$ than the resistive case, roughly as $\exp\left(-\omega_{\rm thr}/1.8\omega_{\rm rms}\right)$. Hence, the resistive energy dissipation exceeds the viscous

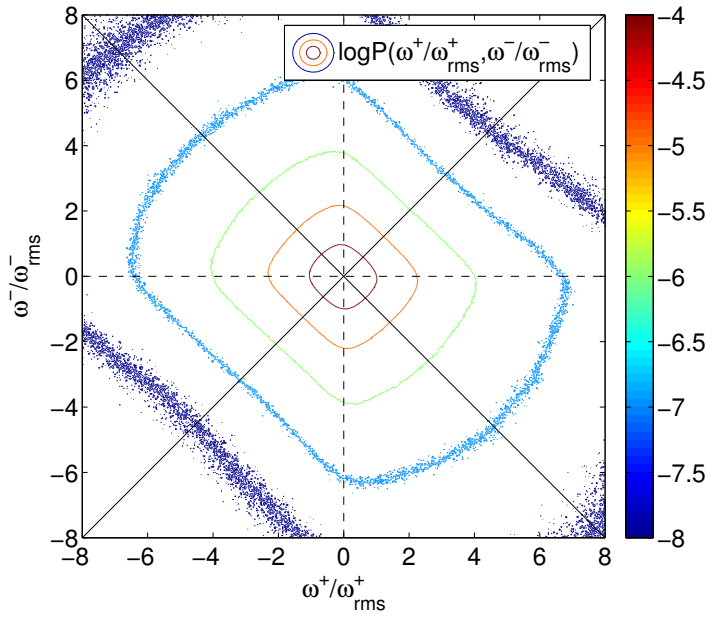

Figure 4.4: The 2D probability density function $P(\omega^+/\omega^+_{\rm rms}, \omega^-/\omega^-_{\rm rms})$. Dashed black lines represent the axes for ω^- and ω^+, while solid black lines represent the axes for j (going from top-left to bottom-right) and ω (going from bottom-left to top-right).

energy dissipation on average (despite $\eta = \nu$), and current sheets are generally more intense than vorticity sheets. We also repeat the same procedure for the magnitude of the fluctuating magnetic field $|\boldsymbol{b}|$ to find the cumulative magnetic energy $|\boldsymbol{b}|^2$ at magnetic fields $|\boldsymbol{b}| > b_{\rm thr}$. The cumulative distribution decreases very rapidly in this case, and can be fit by a Gaussian, $\exp\left[-(b_{\rm thr}/1.5b_{\rm rms})^2\right]$. This is consistent with the fact that the magnetic field is much less intermittent than the current density.

4.3 Relationship between current density and vorticity

Although vorticity structures are not the focus of this thesis, we make some remarks here on the correlation between current density and vorticity in MHD tur-

bulence. The correlations can be seen in the 2D distribution of Elsässer vorticities, $P(\omega^+/\omega^+_{\rm rms}, \omega^-/\omega^-_{\rm rms})$, which is equivalent to $P(j,\omega)$ rotated clockwise by 45 degrees. We show the contours of $P(\omega^+/\omega^+_{\rm rms}, \omega^-/\omega^-_{\rm rms})$ for the $Re = 3200$ simulation in Fig. 4.4. As required by the symmetries of the MHD equations, this distribution is symmetric about the (diagonal) ω and j axes. It is, however, not symmetric about the ω^- and ω^+ axes, instead showing that ω^- and ω^+ have a small tendency to have opposite signs rather than identical signs. This asymmetry is due to the nonlinear term acting with opposite signs on the two populations, skewing ω^+ and ω^- toward opposite signs (as described in Sec. 2.3). As a consequence, j extends to larger values than ω, implying that the resistive energy dissipation will generally be larger than the viscous energy dissipation (despite $\eta = \nu$).

The tendency of j to have a larger amplitude than ω can also be inferred by comparing the total resistive dissipation $\mathcal{E}^\eta_{\rm tot} = \int d^3x \eta j^2$ (simply denoted $\mathcal{E}_{\rm tot}$ above) to the total viscous dissipation, $\mathcal{E}^\nu_{\rm tot} = \int d^3x \nu \omega^2$. We find that $\mathcal{E}^\eta_{\rm tot}/\mathcal{E}^\nu_{\rm tot}$ varies from approximately 1.67 at $Re = 1000$ to 1.42 at $Re = 9000$, indicating a sizeable mismatch between the two types of dissipation which possibly decreases with Re.

Another important relationship is that between dissipation rates in the different fields. To understand this, we show the contours of $P(\omega^2/\omega^2_{\rm rms}, j^2/j^2_{\rm rms})$ (i.e., the distribution for the local viscous and resistive dissipation rates) and $P[(\omega^-/\omega^-_{\rm rms})^2, (\omega^+/\omega^-_{\rm rms})^2]$ (i.e., the distribution for the local Elsässer dissipation rates) in Fig. 4.5. There is a clear anti-correlation between the different local dissipation rates, i.e., large values of j^2 tend to be associated with small values of ω^2, and vice-versa. This implies that intermittent structures in one field are offset from structures in the other field, which may be expected from the quadrupolar structure of vorticity around current sheets (e.g., Matthaeus, 1982; Politano et al., 1995).

4.4 Test of log-normal random cascade

In this section, we consider the statistics of coarse-grained energy dissipation rates, which are the quantities conventionally described by random cascade models. In particular, we perform a careful test of the log-normal model proposed by K62

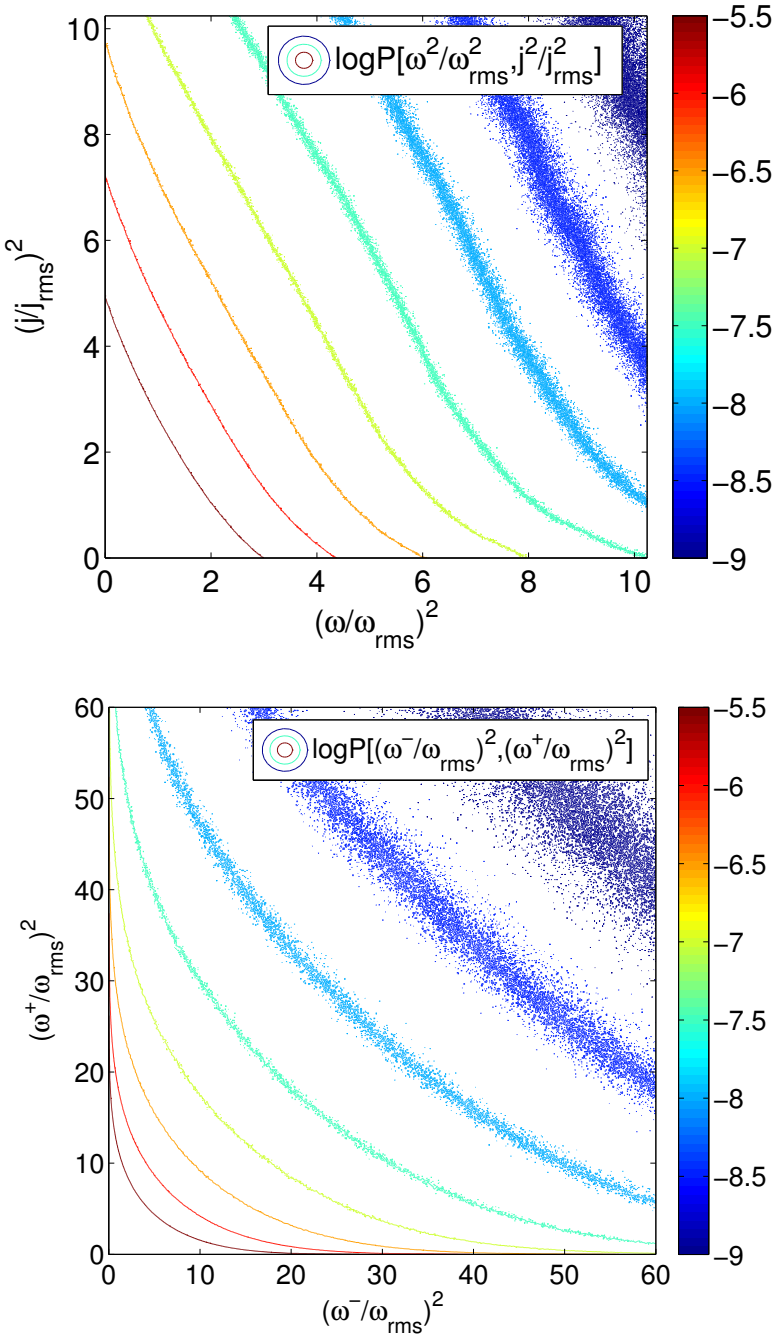

Figure 4.5: The 2D probability density function $P(j^2/j^2_{\rm rms}, \omega^2/\omega^2_{\rm rms})$ (top) and $P(\omega^{+2}/\omega^{+2}_{\rm rms}, \omega^{-2}/\omega^{-2}_{\rm rms})$ (bottom), showing anti-correlation between the two types of energy dissipation.

and described in Section 1.2. By considering the energy dissipation rate rather than structure functions, we bypass the ambiguity associated with formulating the refined similarity hypothesis for MHD. This analysis leads us to conclude that the log-normal model can provide a remarkably good description of the intermittency in incompressible MHD turbulence, although we do not rule out other random cascade models.

It is reasonable to investigate to what extent the log-normal model can describe intermittency in MHD turbulence for several reasons. The first reason is its simplicity; the log-normal model does not make any assumption about the specific form of the dynamical equations, so one may anticipate that it applies to MHD turbulence at least as well as it does to hydrodynamic turbulence. A second reason is that there appears to be a lack of previous numerical tests of the log-normal model in modern high-resolution simulations of MHD turbulence, despite favorable agreement noted in early numerical studies (Biskamp, 1995, 2003). Finally, it can be used to approximate the distribution of local energy dissipation rates, which is linked to the filling fraction of structures.

Following the notation in Biskamp (2003), we subdivide the simulation lattice into regions of size $l_n = 2^{-n} L_\perp$, where n is referred to as the level. The coarse-grained resistive and viscous energy dissipation rates at point $\boldsymbol{x}$, averaged at the nth level, are respectively defined as[2],

$$\begin{aligned} \epsilon_n^\eta(\boldsymbol{x}) &= \frac{1}{V_n} \int_{V_n(\boldsymbol{x})} d^3x' \eta j^2(\boldsymbol{x}+\boldsymbol{x}'), \\ \epsilon_n^\nu(\boldsymbol{x}) &= \frac{1}{V_n} \int_{V_n(\boldsymbol{x})} d^3x' \nu \omega^2(\boldsymbol{x}+\boldsymbol{x}') \,. \end{aligned} \tag{4.3}$$

where integration is performed across a region centered at $\boldsymbol{x}$ with volume V_n. The total coarse-grained energy dissipation rate at $\boldsymbol{x}$ is therefore $\epsilon_n(\boldsymbol{x}) = \epsilon_n^\eta(\boldsymbol{x}) + \epsilon_n^\nu(\boldsymbol{x})$.

[2]Strictly speaking, the local viscous energy dissipation rate should be defined by using $\nu(\partial_i v_j + \partial_j v_i)^2/2$ instead of $\nu\omega^2$ in the integral, which makes the quantity rotationally invariant. By the divergence theorem, these two quantities are equal upon averaging over space. For simplicity, we use $\nu\omega^2$ for the majority of the analysis. We find that using $\nu(\partial_i v_j + \partial_j v_i)^2/2$ gives similar results for averages across large and intermediate scales, differing only near lattice scales.

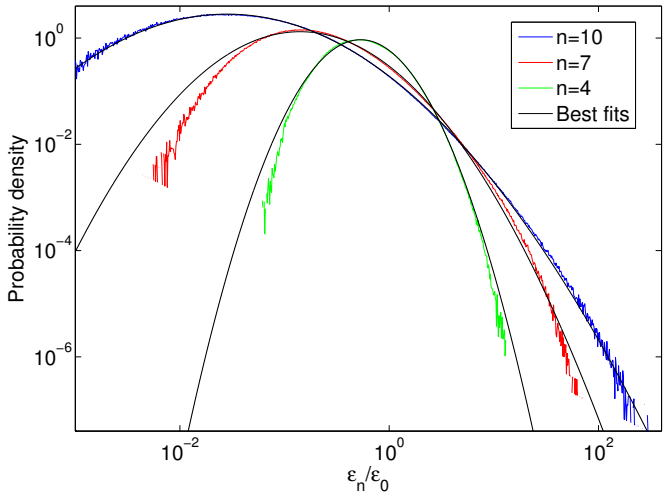

Figure 4.6: The probability distributions for coarse-grained energy dissipation rate, ϵ_n/ϵ_0, for $Re = 9000$ and $n \in \{4, 7, 10\}$ (in green, red, and blue, respectively). Best-fit log-normals are shown in black.

There is some freedom in choosing the shape of the averaging region. As will be seen, the results are largely insensitive to this shape (i.e., cubes, squares, or lines); we focus mainly on square averages. The averaging regions are taken perpendicular to the guide field, since this is the preferential direction for nonlinear energy transfer.

The probability distribution $P(\epsilon_n/\epsilon_0)$ for $n \in \{4, 7, 10\}$ from the $Re = 9000$ simulation are shown in Fig. 6.4. We find that $P(\epsilon_n/\epsilon_0)$ is fit remarkably well by a log-normal distribution,

$$P(\epsilon_n/\epsilon_0) = \frac{1}{\sqrt{2\pi\sigma_n^2}} \frac{\epsilon_0}{\epsilon_n} \exp\left[-\frac{1}{2\sigma_n^2}\left(\log\frac{\epsilon_n}{\epsilon_0} - \mu_n\right)^2\right], \tag{4.4}$$

where μ_n and σ_n are the location parameter and scale parameter, respectively. The log-normal distribution provides a reasonable fit to the bulk and tails of $P(\epsilon_n/\epsilon_0)$ for all scales in all of the given simulations.

We now consider the scaling properties of the log-normal fits. Since the variables are normalized to the mean, the parameters must satisfy $\mu_n = -\sigma_n^2/2$, leaving one free

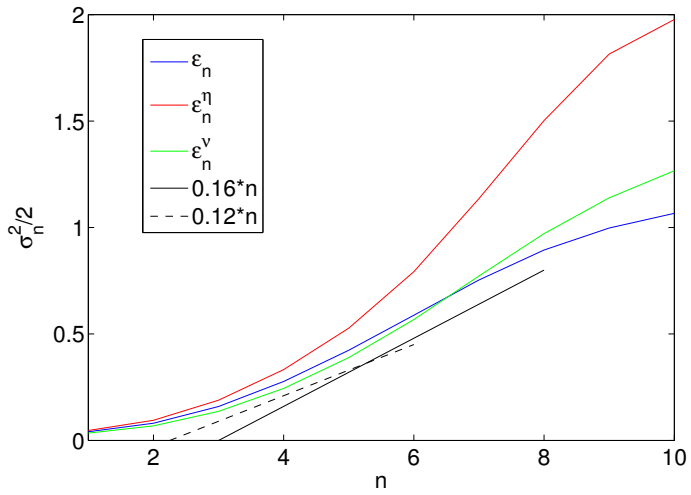

Figure 4.7: The scaling of $\sigma_n^2/2$, obtained from best-fit log-normals to distributions of ϵ_n/ϵ_0 (blue), $\epsilon_n^\eta/\epsilon_0^\eta$ (red), and $\epsilon_n^\nu/\epsilon_0^\nu$ (green) for $Re = 1800$ with averages taken across squares. Linear scalings proportional to $0.12n$ (dashed black) and $0.16n$ (solid black) are shown.

parameter for each level. The log-normal model predicts that $\sigma_n^2/2 \sim cn$, where the constant c is related to the intermittency parameter m (denoted by μ in Section 1.2) by $m = 2c/\log 2$; for reference, $m \approx 0.2$ in hydrodynamic turbulence (e.g., Biskamp, 2003; Sreenivasan and Kailasnath, 1993).

The scaling of $\sigma_n^2/2$, obtained from the best-fit log-normal distributions, are shown in Fig. 4.7 for ϵ_n/ϵ_0, $\epsilon_n^\eta/\epsilon_0^\eta$ and $\epsilon_n^\nu/\epsilon_0^\nu$. For this case, we took $Re = 1800$ and square averaging. Focusing on the total dissipation rate, ϵ_n/ϵ_0, we identify a range of intermediate scales where $\sigma_n^2/2 \approx c(n-1)$, with $c \approx 0.16$, implying an intermittency parameter of $m \approx 0.46$. These scales are mainly in the dissipation range. If we focus only on the inertial range, the scaling is shallower, with $c \approx 0.12$ ($m \approx 0.35$); however, this limited inertial range is not as robustly fit by a linear scaling. The resistive contribution alone, $\epsilon_n^\eta/\epsilon_0^\eta$, has a significantly steeper scaling, which may be due to the anti-correlation of j^2 and ω^2 in the dissipation range, causing them to individually have a larger scatter of values.

The scaling of $\sigma_n^2/2$ in the linear region is insensitive to the shape of the averaging

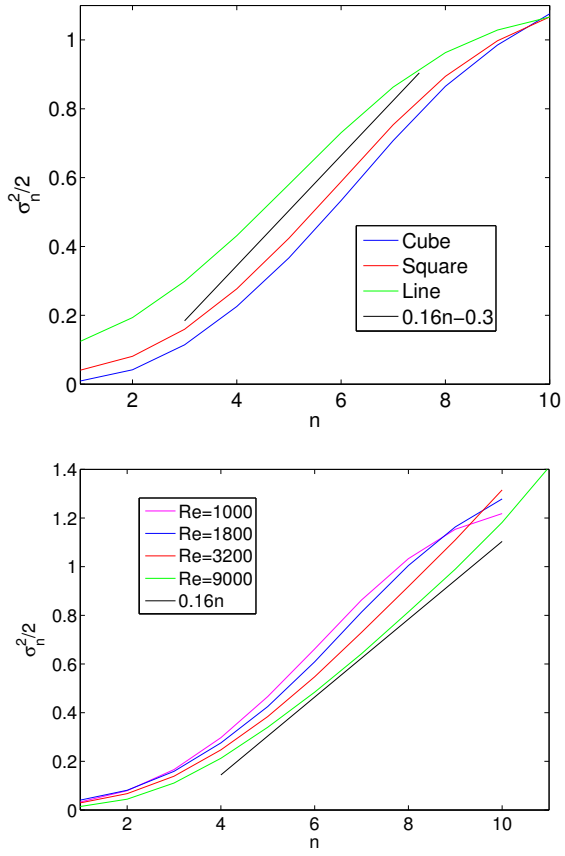

Figure 4.8: Top panel: $\sigma_n^2/2$, obtained from best-fit log-normals, for $Re = 1800$ with averages in ϵ_n taken across lattice cubes (blue), squares (red), and lines (green). Bottom panel: $\sigma_n^2/2$ with varying Reynolds number: $Re = 1000$ (magenta), 1800 (blue), 3200 (red), and 9000 (green).

regions, the numerical resolution, and Re, as shown in Fig. 4.8, although these factors may shift the curve. Averages performed across lattice cubes (i.e., rectangles with aspect ratio $L_\parallel/L_\perp$) and squares give nearly identical results, whereas line averages have notably larger variances. Increasing Re decreases the variance and shifts the curve to higher n, as expected from a decreasing dissipation scale. This implies that most of the scaling takes place in the dissipation range, with the inertial range scaling being barely discernable (going from $n \approx 1$ to $n \approx 4$.

The above results are consistent with a log-normal random cascade, but do not rule out other models such as the log-Poisson model. To get a sense of how well the log-Poisson model compares, we next consider the moments of the distributions. The pth moment of the coarse-grained energy dissipation rate is expected to scale as $\langle \epsilon_l^p \rangle \sim l^{-\tau_p}$. For the log-normal model, the scaling exponents are given by

$$\tau_p^{(LN)} = \frac{1}{2} mp(p-1)\,. \tag{4.5}$$

For the log-Poisson model, the scaling exponents are instead given by

$$\tau_p^{(LP)} = C(1-\beta)p - C(1-\beta^p)\,, \tag{4.6}$$

where C is the co-dimension of the most intermittent structure and β is the efficiency of energy transfer. In particular, Müller and Biskamp (2000) proposed that $C = 1$ and $\beta = 1/3$ for MHD turbulence, representing ribbon-like dissipative structures and hydrodynamic scaling.

We show $\langle \epsilon_l^p \rangle$ for $p \in \{2, 3, 4, 5\}$, compensated by the predicted scalings for each model, in Figs. 4.9 and 4.10 for $Re = 1800$ and $Re = 9000$, respectively. We find that both Eq. 4.5 and Eq. 4.6 can fit the results reasonably well for $p = 2$ and $p = 3$, but then deviate for higher orders. We find that, overall, the log-normal model (with $m = 0.35$, somewhat smaller than the scaling inferred from $\sigma_n^2/2$ in the dissipation range) may describe the results somewhat better than the log-Poisson model for the given parameters, especially for the more reliable data at low p. The predicted log-normal scaling works well for $p = 2$ to $p = 4$, but then shows large deviations

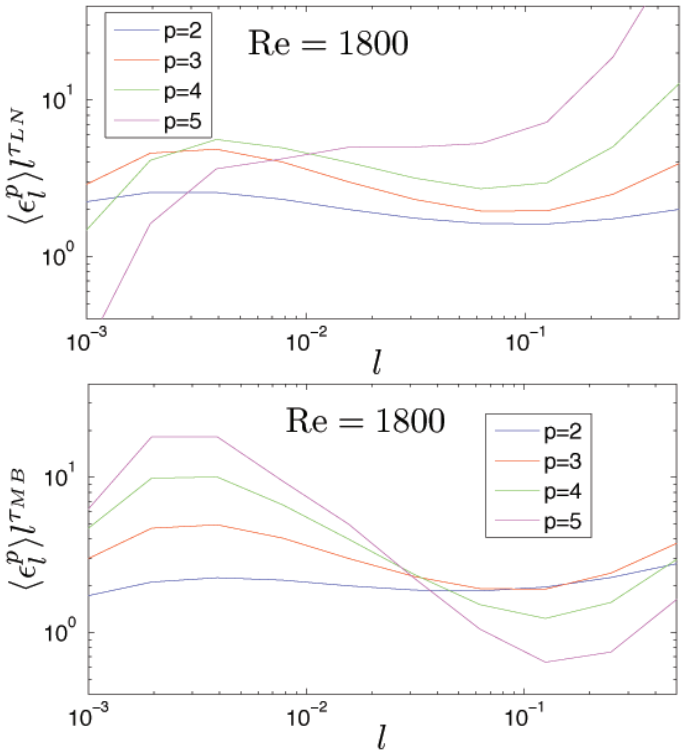

Figure 4.9: Moments of the coarse-grained energy dissipation rate, $\langle \epsilon_l^p \rangle$, versus l, for $p \in \{2, 3, 4, 5\}$, compensated by expected power-law scaling for the log-normal model with $m = 0.35$ (top panel) and for the log-Poisson model (with Müller-Biskamp parameters) (bottom panel). Measured from square averages in the $Re = 1800$ case.

beyond $p = 5$, consistent with the expected accuracy limits due to finite statistics (De Wit, 2004). The log-Poisson model shows deviations at $p = 4$, but may possibly be fined-tuned with other values of C and β to give an improved fit.

4.5 Connecting log-normal statistics with current sheets

The results in the previous section suggest that the log-normal model provides a reasonable approximation of intermittency in MHD turbulence. Although the log-

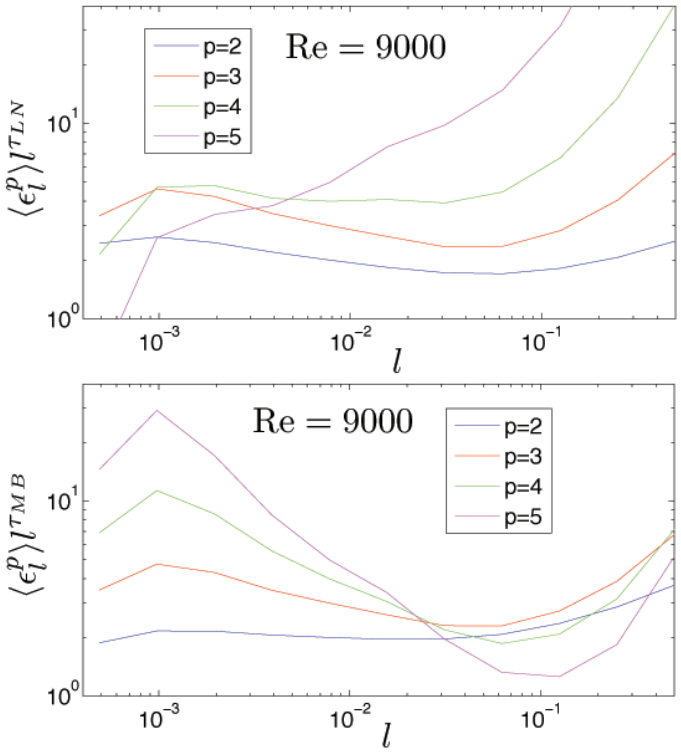

Figure 4.10: Same as Fig. 4.9, but for $Re = 9000$.

normal model best describes the energy dissipation rates averaged at intermediate scales, we can also use it to estimate the current density on the lattice. In particular, we can estimate that

$$P(\tilde{j}^2) \sim \frac{1}{\sqrt{2\pi\sigma^2}} \frac{1}{\tilde{j}^2} \exp\left[-\frac{1}{2\sigma^2}\left(\log \tilde{j}^2 - \mu\right)^2\right], \tag{4.7}$$

where $\tilde{j} = j/j_{\rm rms}$ and $\sigma^2/2 = -\mu$. We can then obtain the cumulative distribution of energy dissipation rates,

$$\begin{aligned}\frac{\mathcal{E}_{\rm cum}(\tilde{j}_{\rm thr})}{\mathcal{E}_{\rm tot}} &= \int_{\tilde{j}^2_{\rm thr}}^{\infty} d\tilde{j}^2 \tilde{j}^2 P\left(\tilde{j}^2\right) \\ &= \frac{1}{\sqrt{2\pi\sigma^2}} \int_{\tilde{j}^2_{\rm thr}}^{\infty} d\tilde{j}^2 \exp\left[-\frac{1}{2\sigma^2}\left(\log\tilde{j}^2 - \mu\right)^2\right] \\ &= \frac{1}{2}\left[1 - {\rm erf}\left(\frac{\log\tilde{j}^2_{\rm thr} - \sigma^2/2}{\sqrt{2}\sigma}\right)\right], \end{aligned} \tag{4.8}$$

and the filling fraction,

$$\frac{V_{\rm cum}(\tilde{j}_{\rm thr})}{V_{\rm tot}} = \int_{\tilde{j}^2_{\rm thr}}^{\infty} d\tilde{j}^2 P(\tilde{j}^2) = \frac{1}{2}\left[1 - {\rm erf}\left(\frac{\log\tilde{j}^2_{\rm thr} + \sigma^2/2}{\sqrt{2}\sigma}\right)\right]. \tag{4.9}$$

The cumulative energy dissipation from the log-normal distribution (Eq. 4.8) is compared with the direct measurements from the simulations in Fig. 4.11. The model works well up to $j_{\rm thr}/j_{\rm rms} \approx 10$, beyond which it overestimates the observed result. This deviation is likely due to the fact that a log-normal distribution does not adequately describe the resistive energy dissipation at the lattice scale.

We note, in passing, that if a random cascade model describes the distribution of local resistive energy dissipation rates, then $\mathcal{E}_{\rm cum}(j_{\rm thr}/j_{\rm rms})$ cannot be universal, due to the increasing variance of $P(j/j_{\rm rms})$ with Re. If this is the case, then the apparent universality seen in Fig. 4.2 must be violated for well-resolved simulations with higher Reynolds numbers.

4.6 Discussion

In this chapter, we showed that the log-normal model provides a reasonable description of the distribution of the coarse-grained energy dissipation rates in the RMHD simulations. We measured the intermittency parameter to be $m \approx 0.45$ at intermediate scales, and possibly closer to $m \approx 0.35$ in the inertial range. This implies that RMHD

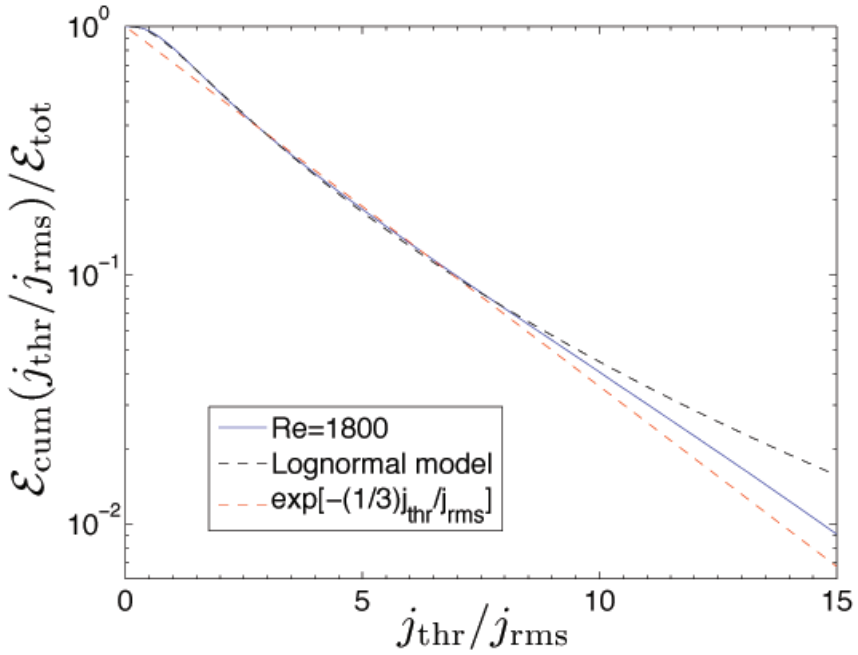

Figure 4.11: The fraction of overall resistive energy dissipation versus threshold (for $Re = 1800$) fit by the integrated log-normal distribution (black dashed line) and fit by the exponential function (red dashed line).

is significantly more intermittent than hydrodynamic turbulence, as noted in previous numerical studies using structure functions (e.g., Müller and Biskamp, 2000; **?**).

Due to the challenges in testing and distinguishing between the various models, however, we cannot rule out a log-Poisson or other random cascade process. We also note that, while log-normal model provides an estimate of the energy dissipated and volume occupied by structures at various thresholds, it does not give any direct insight into the morphology of intermittent structures. These issues motivate other approaches to studying intermittency, including the analysis of current sheets and dissipative processes in the next two chapters.

Although we considered the log-normal model for intermittency in the MHD regime, a similar process may describe turbulent plasmas with more realistic, kinetic mechanisms of energy dissipation. Indeed, random cascade models take the inertial-

range energy cascade rate as the fundamental quantity, which should be insensitive to the mechanism of energy dissipation. This allows the log-normal model to be tested in the solar wind by using magnetic field gradients as a proxy for current density, which itself is a proxy for energy dissipation (as used in, e.g., Makwana et al., 2015). A comparison of the coarse-grained energy dissipation rates in MHD simulations with a weak guide field and in solar wind measurements is currently in preparation (Zhdankin et al., 2015a). Log-normal distributions were previously measured in the solar wind for related quantities such as the magnetic field fluctuations (Burlaga, 2001; Bruno et al., 2004) and rotational discontinuities (Zhdankin et al., 2012b,a), which may also serve as indirect surrogates for energy dissipation.

5 SPATIAL ANALYSIS

5.1 Overview of spatial analysis

This chapter describes the results from our statistical analysis of intermittent, dissipative current sheets at fixed time in numerical simulations of MHD turbulence, using the methodology described in the first part of Chapter 3, including measurements of the characteristic scales defined in Sec. 3.2. The scalings and probability distributions for current sheet characteristics are described in Sec. 5.2 and Sec. 5.3, respectively. Some remarks on the population size are presented in Sec. 5.4. The main results are summarized in Sec. 5.5. For most of the analysis in this chapter, unless otherwise noted, we fix the threshold to $j_{\rm thr}/j_{\rm rms} \approx 3.75$.

Before proceeding, we show some visual examples of current sheets in the reduced MHD simulations (described in Sec. 4.1). Fig. 5.1 shows regions of intense current density (exceeding the threshold) in a 3D slab which extends a quarter of the box in the z direction of the $Re = 1800$ simulation. There is evidently a large sample of filamentary or ribbon-like structures in the box, aligned with the guide field. Fig. 5.2 shows two large current sheets (and additional nearby small current sheets) in part of the simulation domain, spanning roughly a third of the simulation box in length. Each structure is shown from two different orientations, demonstrating the overall ribbon-like shape, although it is clear that the structures are very irregular as well, showing curvature, twisting, and branching. Fig. 5.3 shows contours of current density in an arbitrary plane perpendicular to the guide field. The three panels show increasing Reynolds number, in the order $Re = 1000$, $Re = 3200$, and $Re = 9000$. These contour plots reveal that when Re increases, the structures become finer and more morphologically complex. Although these visual examples qualitatively show nontrivial structure at all scales, a statistical analysis is necessary in order to quantitatively determine which structures are dominant.

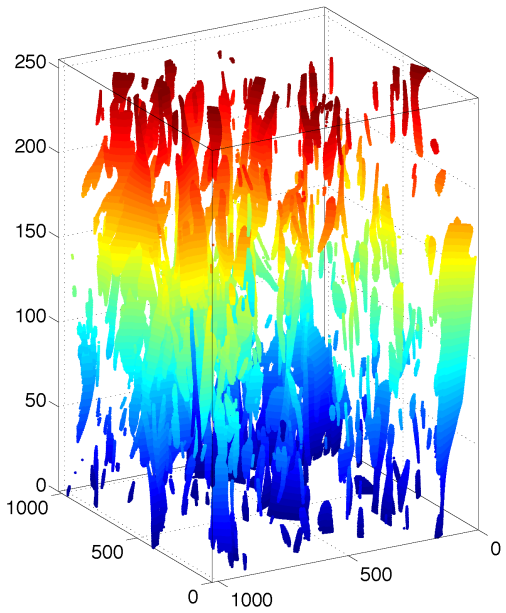

Figure 5.1: Regions of intense current density (exceeding the threshold) in a 3D slab of the reduced MHD simulation with $Re = 1800$. The slab extends in the full horizontal scale of the simulation, but only a quarter of the vertical scale. For clarity, colors indicate the z coordinate of points.

5.2 Current sheet scalings

We first discuss the scaling properties of the current sheets. These scalings can be inferred from scatterplots of the measurements, but for clarity, we instead show 2D probability distributions $P(X, Y)$, where $P(X, Y)dXdY$ is the probability of finding a structure with values between X and $X + dX$ for the first measured quantity and between Y and $Y + dY$ for the second measured quantity.

We begin by comparing the characteristic scales measured by the Euclidean method with the corresponding scales measured by the Minkowski method. The correlations are shown in the 2D distributions $P(L_m, L_e)$, $P(W_m, W_e)$, and $P(T_m, T_e)$ in Fig. 5.4. We find that the two methods agree very well at small and intermediate scales, while

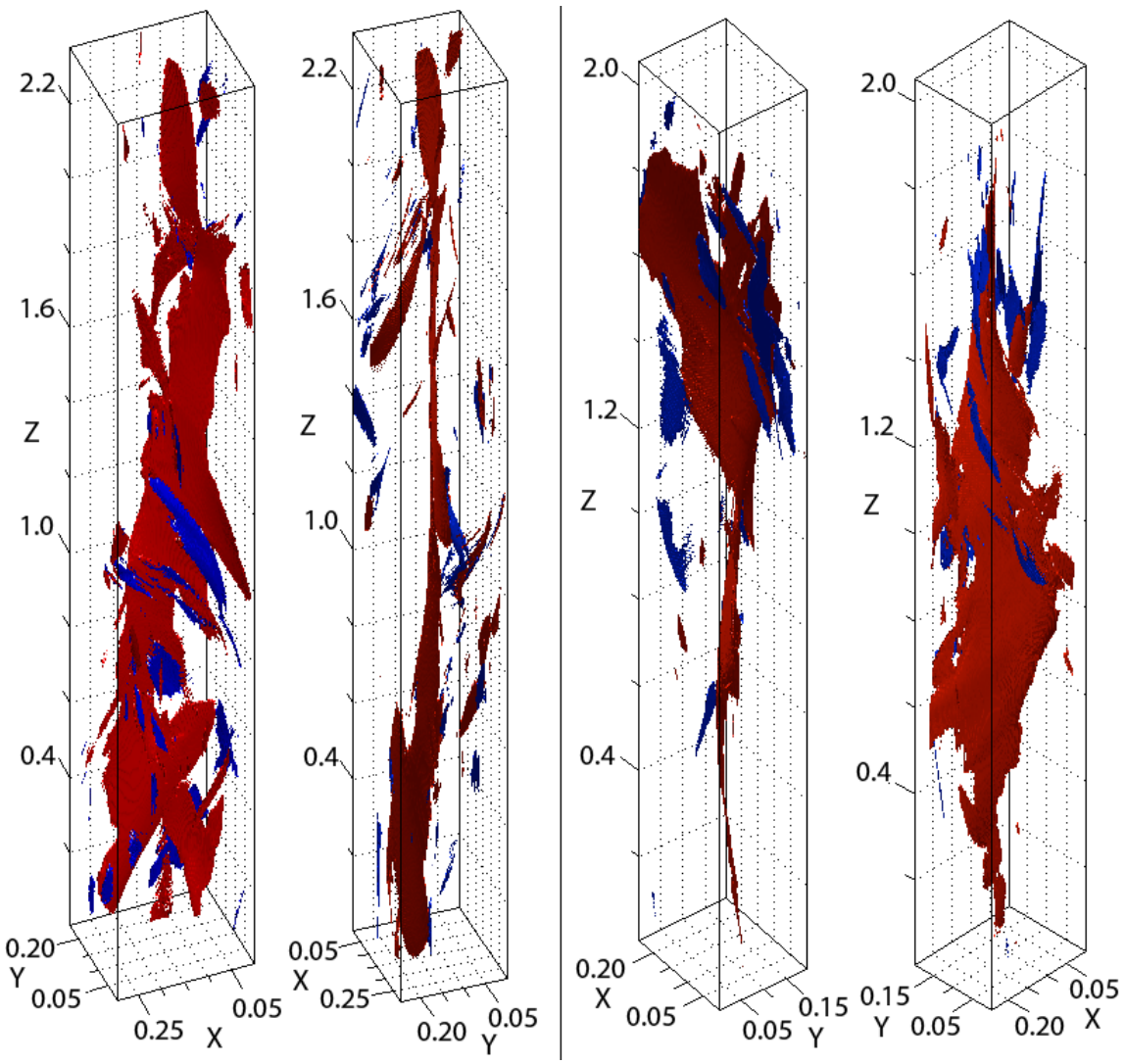

Figure 5.2: Samples of typical large current sheets in part of the simulation domain, surrounded by several smaller structures (red/blue indicates sign of current density). The left panel shows two orientations of one structure, while the right panel shows two orientations of a different structure. These samples are taken from the $Re = 1800$ simulation with a threshold of $j_{\mathrm{thr}}/j_{\mathrm{rms}} \approx 6.5$.

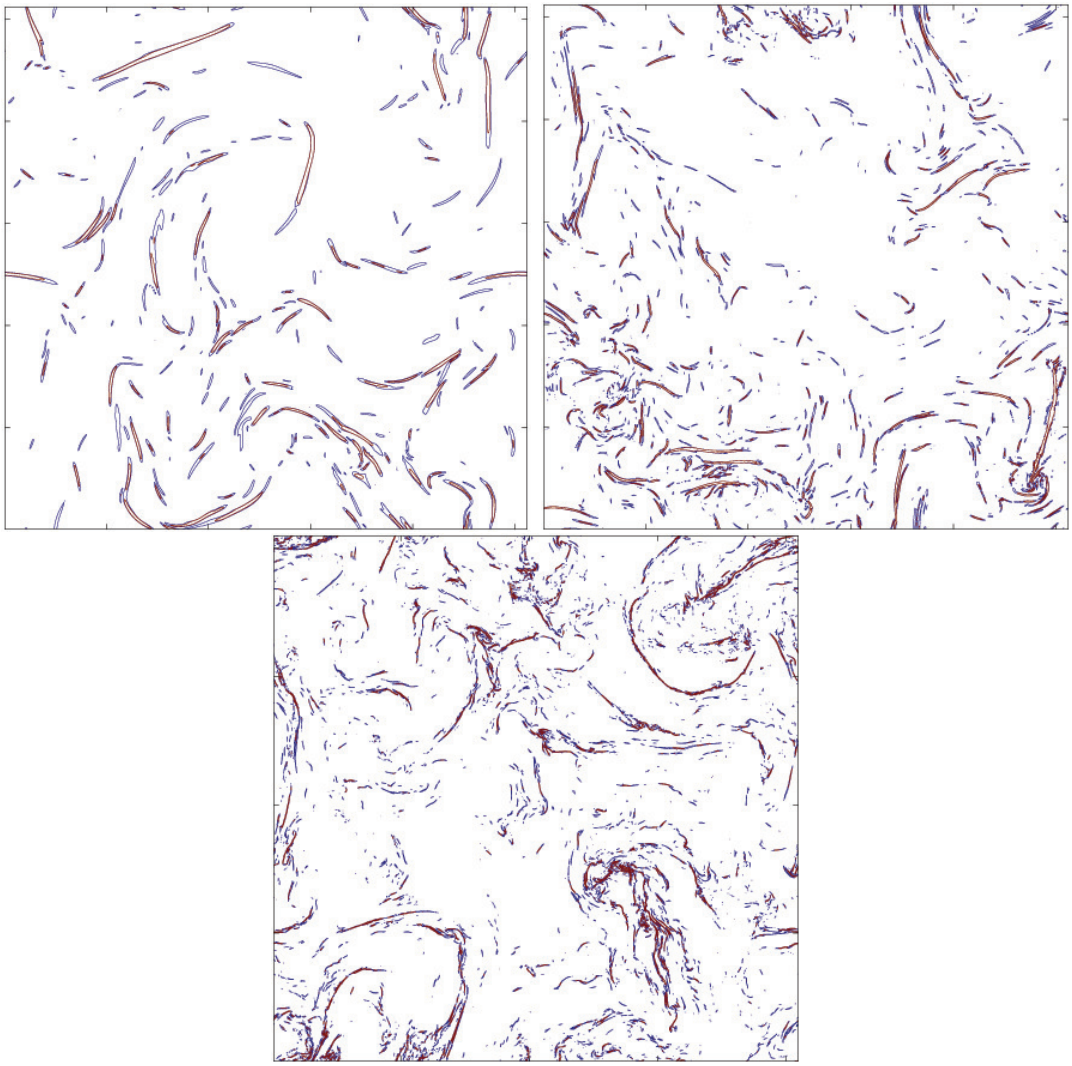

Figure 5.3: Contours of current density in an arbitrary plane perpendicular to the guide field. Contours are taken at $j_{\rm thr}/j_{\rm rms} = 2$ (blue) and $j_{\rm thr}/j_{\rm rms} = 3$ (red) for increasing Reynolds number (clockwise from top left, $Re = 1000$, 3200, and 9000).

there is noticeable deviation between the two methods at large scales. In particular, L_m is skewed toward larger scales than L_e, while W_m is skewed toward smaller scales than W_e. This is evidently due to the increasing morphological complexity of the structures, which is captured by the Minkowski method but not by the Euclidean method. The thicknesses generally agree well, although there is a significant fraction of measurements in which T_e greatly exceeds T_m. These spurious measurements can occur when T_e is measured in a poorly chosen direction (for example, T_e is overestimated for a current sheet with an S-shaped cross-section).

We next consider the correlations between the different scales. For economy, we take the Euclidean length as a reference scale, since it is arguably the best-measured scale. The 2D distributions showing the various scalings with L_e are shown in Fig. 5.5. We find robust scalings between Euclidean length and width, going as $L_e \sim W_e$. As mentioned previously, W_m and L_m deviate from their the Euclidean counterparts, although we can fit $L_e \sim W_m^{1.2}$. The scaling for thickness is much more difficult to determine, mainly because it is spread over a very small range of values and shows a large amount of scatter in L_e for any given thickness. We find scalings consistent with $L_e \sim T_e^2 \sim T_m^2$ for $Re = 1800$, although this scaling is not as clear in the cases with higher Re. A more precise measurement of the scaling for thickness requires numerical simulations which are both well-resolved in the dissipation range and have a large separation of scales, which may be difficult to obtain in the near future.

Finally, we consider the scaling of the volume and energy dissipation rate. As shown in Fig. 5.6, the scaling of energy dissipation rate $\mathcal{E}$ with L_e is somewhat steeper than the scaling of volume V with L_e. Specifically, the distributions are well fit by $\mathcal{E} \sim L_e^{2.4}$ while $V \sim L_e^{2.2}$. The correlation can be more clearly seen by plotting $\mathcal{E}$ versus V, which reveals that $\mathcal{E} \sim V^{1.1}$. Thus, the energy dissipation rate is not strictly proportional to volume, meaning that the amplitude of the structure (i.e., $\langle j^2 \rangle$ averaged in the structure) has a small dependence on the size of the structure. This is reasonable since larger structures can accommodate higher current densities than weaker structures. In other words, on average, the local peak is higher relative to the threshold for larger structures than for smaller structures.

We next consider the dependence of some of these scalings on threshold. As shown

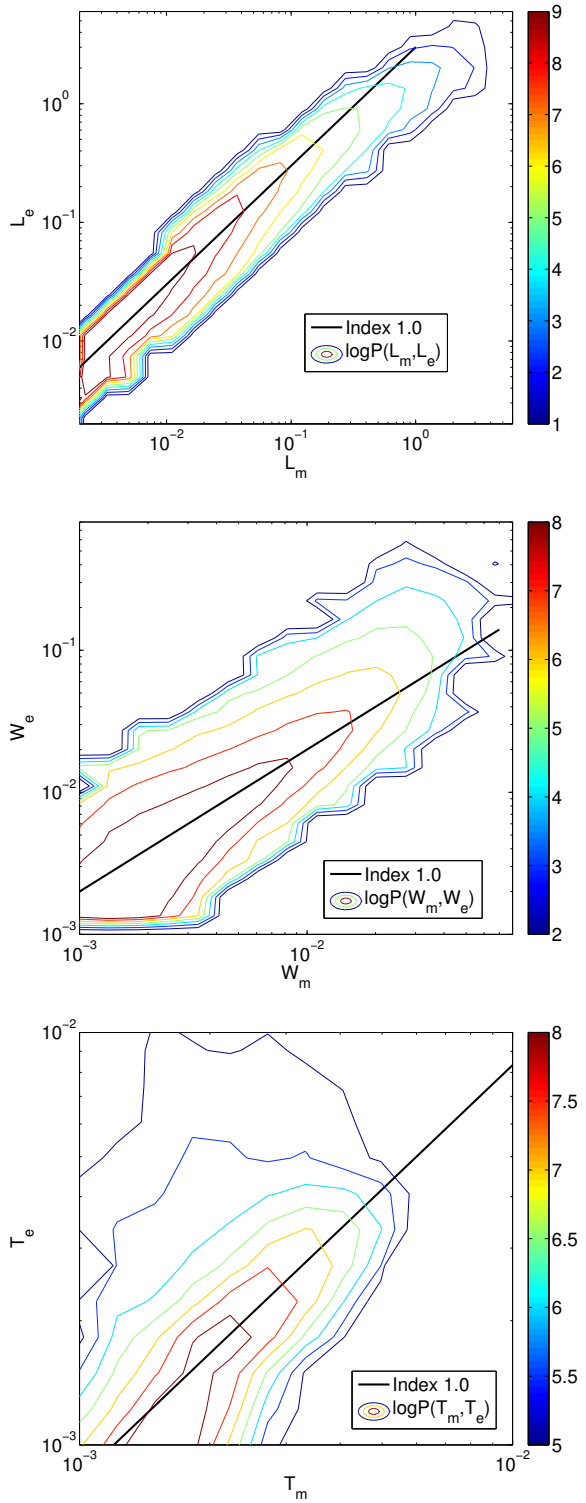

Figure 5.4: Contours of 2D probability distributions comparing the Euclidean method to the Minkowski method for measurements of current sheet lengths, widths, and thicknesses (for $Re = 1800$). The first panel compares L_e to L_m, the second panel compares W_e to W_m, and the third panel compares T_e to T_m.

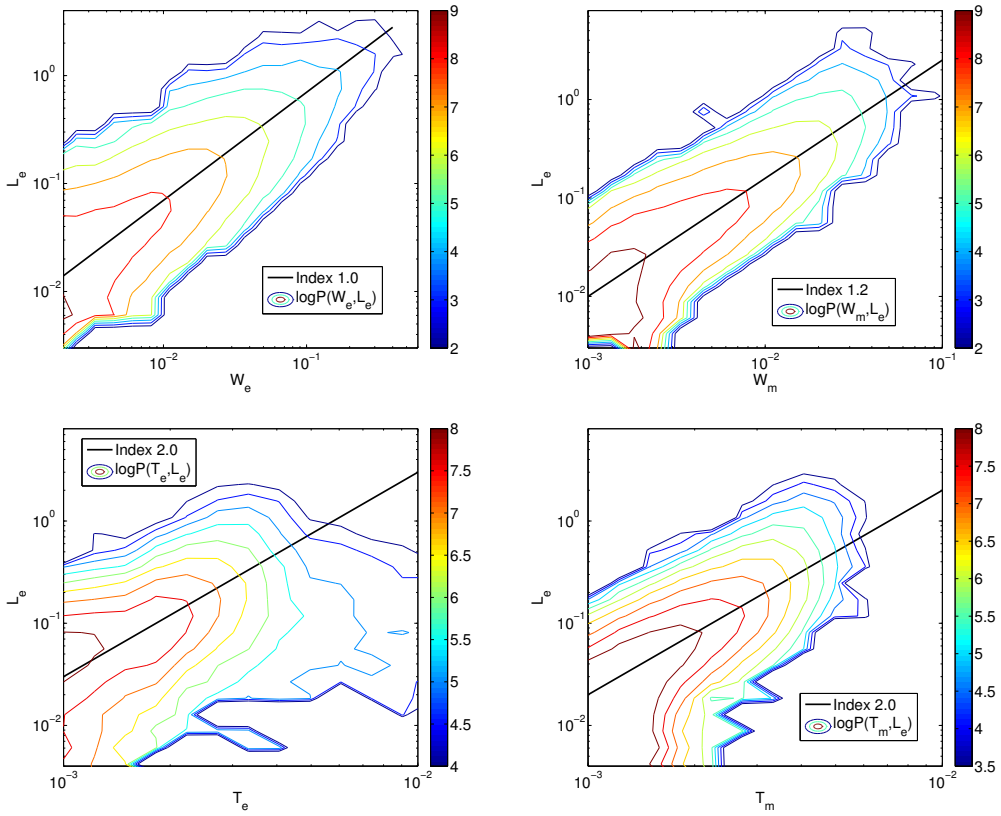

Figure 5.5: Contours of 2D probability distributions comparing Euclidean length L_e with other scales of current sheets (for $Re = 1800$). Clockwise from top left, the panels show $P(W_e, L_e)$, $P(W_m, L_e)$, $P(T_m, L_e)$, and $P(T_e, L_e)$.

in Fig. 5.7, the scaling of V versus L_e shows very little sensitivity over a large range of thresholds, $1 < j_{\rm thr}/j_{\rm rms} < 9$. The scaling of $\mathcal{E}$ versus V does not substantially change either, although the constant multiplier does change. We find that one the threshold dependence is account for, the scaling is approximated by $\mathcal{E} \approx 5\eta j_{\rm thr}^2 V^{1.1}$.

5.3 Current sheet distributions

We now consider the probability distributions for the quantities measured in the given population of current sheets. We begin with the distribution for energy dissipation

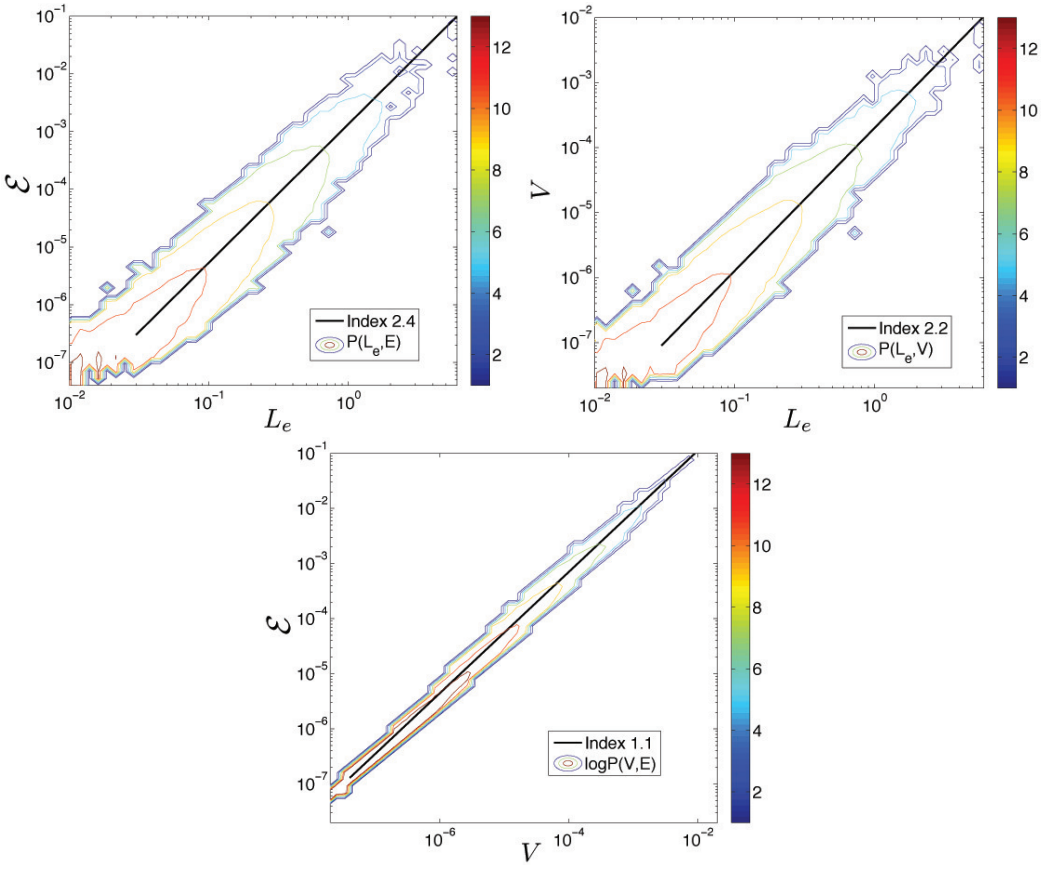

Figure 5.6: Contours of 2D probability distributions comparing Euclidean length L_e, volume V, and energy dissipation rate $\mathcal{E}$ of current sheets (for $Re = 1800$). Clockwise from top left, the panels show $P(L_e, \mathcal{E})$, $P(L_e, V)$, and $P(V, \mathcal{E})$.

rates. Let $P(\mathcal{E})d\mathcal{E}$ denote the number of structures with energy dissipation rate between $\mathcal{E}$ and $\mathcal{E} + d\mathcal{E}$, normalized to total number. As shown in Fig. 5.8, the distribution has a power-law tail $P(\mathcal{E}) \sim \mathcal{E}^{-\beta}$ with an index between $\beta = 1.8$ and $\beta = 2.0$ for all cases. From the compensated distribution $P(\mathcal{E})\mathcal{E}^2$, it is clear that with increasing Re, the distribution approaches a value of $\beta = 2.0$. This index is insensitive to the threshold, as demonstrated for the $Re = 9000$ case in the final panel of Fig. 5.8. In the regime of small $\mathcal{E}$, $P(\mathcal{E})$ becomes shallower with no evident universal behavior. The structures in this regime are a combination of structures

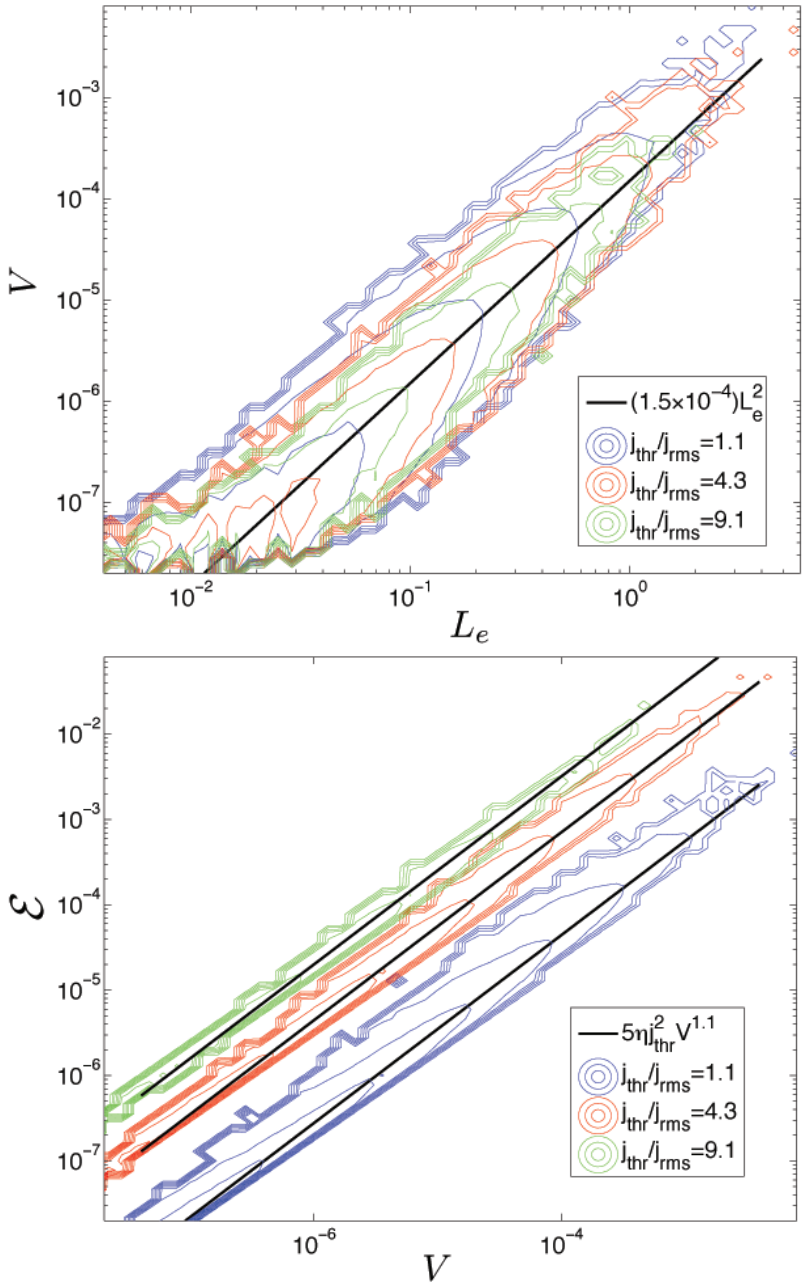

Figure 5.7: Contours of 2D probability distributions $P(L_e, V)$ (top) and $P(V, \mathcal{E})$ (bottom) at thresholds $j_{\rm thr}/j_{\rm rms} \in \{1.1, 4.3, 9.1\}$ (blue, red, and green contours, respectively) for $Re = 1800$.

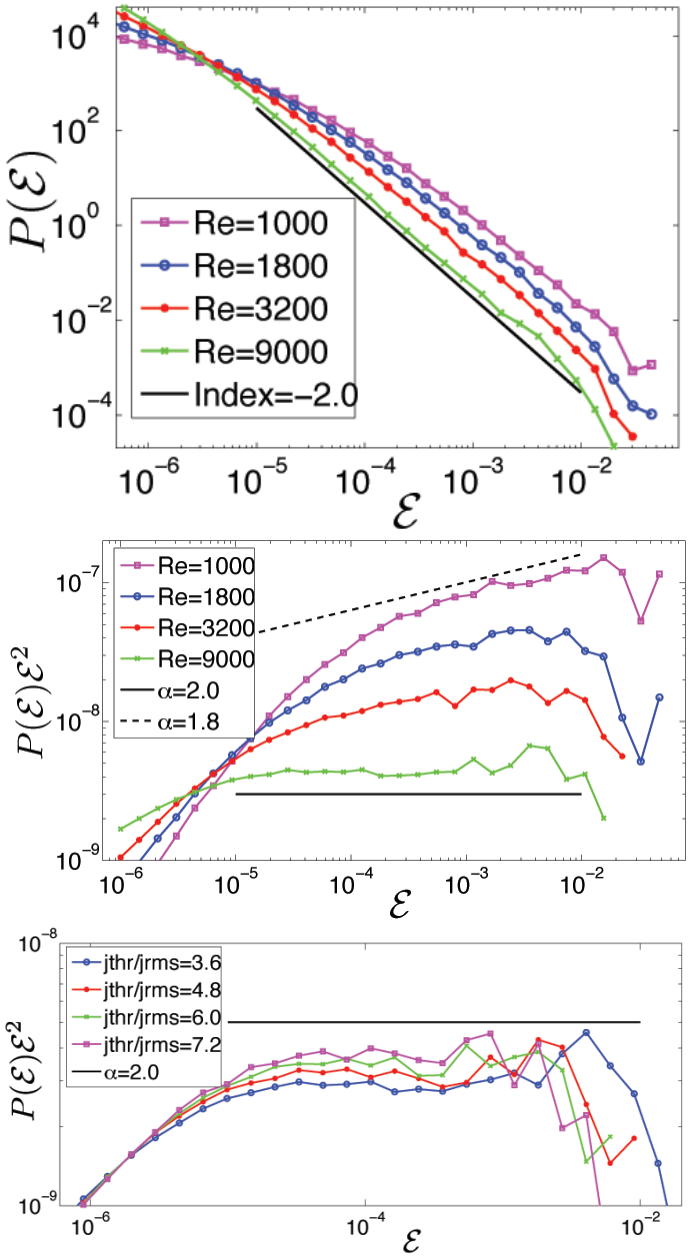

Figure 5.8: Top panel: the probability distribution $P(\mathcal{E})$ for energy dissipation rate of structures, with colors corresponding to $Re = 1000$ (magenta), $Re = 1800$ (blue), $Re = 3200$ (red), and $Re = 9000$ (green). The index for the power-law tail appears to converge to the critical value of -2 as Re increases. Middle panel: the same distribution compensated by $\mathcal{E}^2$, better showing the convergence with Re. Bottom panel: the compensated distribution for $Re = 9000$ with several different thresholds, $j_{\rm thr}/j_{\rm rms} = 3.6$ (blue), 4.8 (red), 6.0 (green), and 7.2 (magenta).

near the threshold and structures with scales completely within the dissipation range.

As mentioned previously (see Eq. 1.8), a power-law distribution with the critical value of -2 for the index has an expected value which is marginally divergent at both limits. In the case of $P(\mathcal{E})$, the critical index implies that the instantaneous energy dissipation rate is equally partitioned across structures of all intensities, with no preference toward strong structures or weak structures.

We next consider the probability distributions for the spatial scales of the current sheets, as shown in Fig. 5.9. We find that L_e, L_m, and W_e have robust power-law distributions, with corresponding indices near -3.3, -2.5, and -3.3. This confirms that $L_e \sim W_e$, with both being inertial-range quantities; L_m is also an inertial-range quantity, but apparently scales with the volume. On the other hand, the distributions for W_m, T_e, and T_m decrease very rapidly and are not clear power laws. These scales are in the dissipation range for most structures.

One may expect that the shifts in the distributions for W_m, T_e, and T_m with Re are related to the dissipation scale. As shown in Fig. 5.10, the measured scales can all be rescaled by different powers of Re to make the distributions align for all of the given simulations. From this rescaling, we infer that $W_m \sim Re^{-3/4}$ (which is the dissipation scale in K41 and GS95), $T_m \sim Re^{-3/5}$, and $T_e \sim Re^{-1/2}$. The thickness scalings, however, may be sensitive to resolution.

We note, in passing, that since the observed scalings imply that W_m decreases faster than T_m with increasing Re, the two scales will apparently become comparable at large Re. Taking as a reference value $W_m \sim 10^{-2}$ and $T_m \sim 3 \times 10^{-3}$ at $Re = 1000$, the two scales are projected to coincide when $Re \sim 10^6$, if the observed power-law scalings are assumed to continue holding. Since $W_m > T_m$ cannot be violated due to the isoperimetric inequalities, this implies that the structures either undergo a morphological transition or become unstable at some value of Re. This is reasonable since high aspect-ratio current sheets are known to be unstable to the tearing instability (at $Rm \sim 10^4$ for 2D laminar current sheets (e.g., Uzdensky et al., 2010)), and similar instabilities affect intermittent vorticity filaments in numerical simulations of Navier-Stokes turbulence at high Reynolds numbers (Ishihara et al., 2009). Alternatively, it is possible that the scaling of T_m is affected by resolution and should in fact be closer

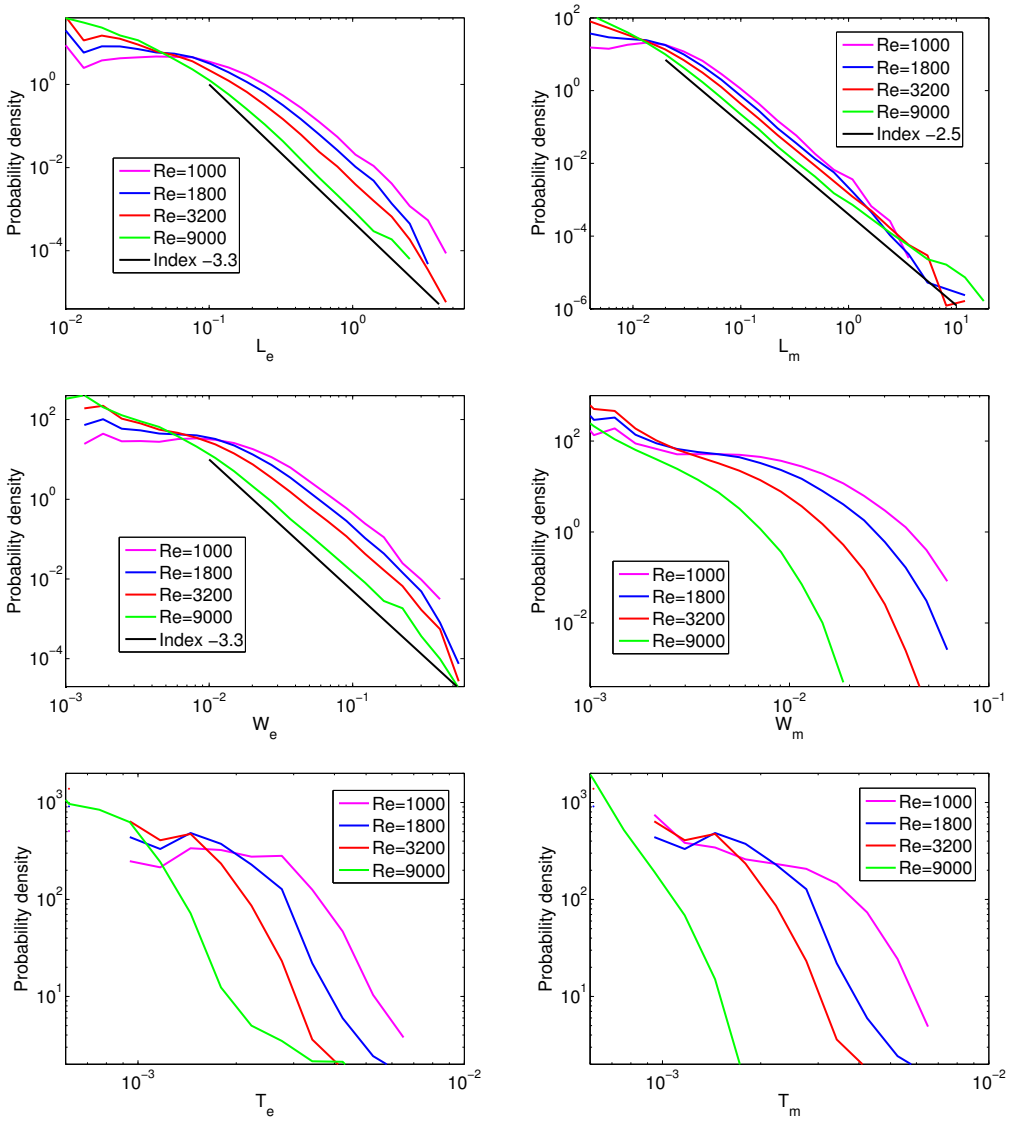

Figure 5.9: The probability distributions for spatial scales of current sheets, for $Re = 1000$ (magenta), $Re = 1800$ (blue), $Re = 3200$ (red), and $Re = 9000$ (green). Euclidean scales L_e, W_e, and T_e are shown in descending order on the left column, and Minkowski scales L_m, W_m, and T_m are shown in descending order on the right column.

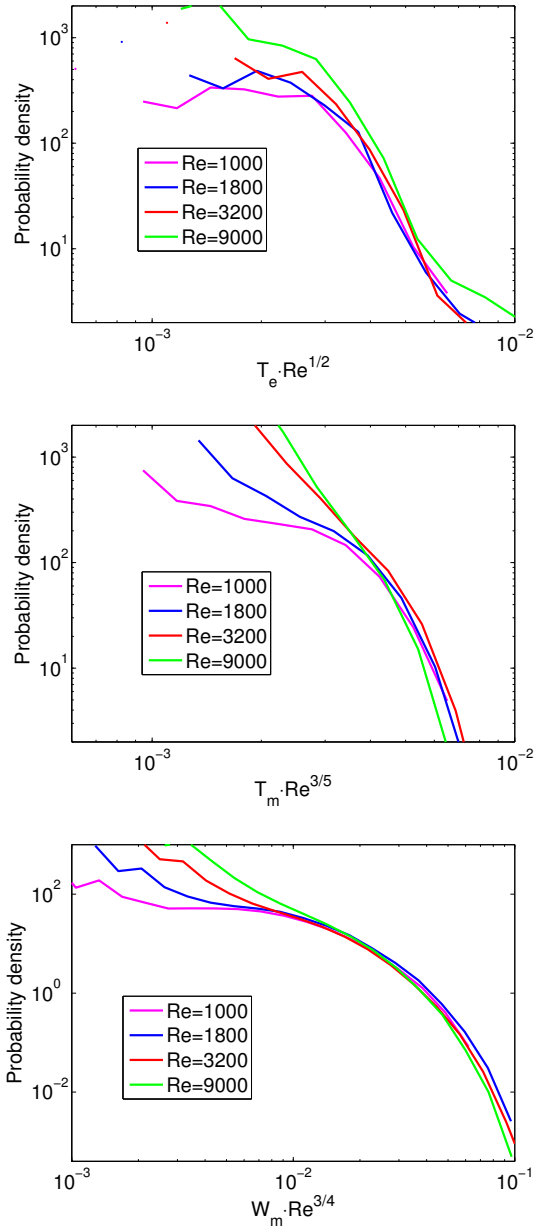

Figure 5.10: The probability distributions for rescaled spatial scales of current sheets, for $Re = 1000$ (magenta), $Re = 1800$ (blue), $Re = 3200$ (red), and $Re = 9000$ (green). Distributions for $T_e Re^{1/2}$, $T_m Re^{3/5}$, and $W_m Re^{3/4}$ are shown in descending order.

to that of W_m.

In order to ascertain which scales are energetically most relevant, we next consider the dissipation-weighted distributions $E(X)$, defined such that $E(X)dX$ is the combined energy dissipation rate for structures with the measured scale between X and $X + dX$. The maximum of the compensated dissipation-weighted distribution, $E(X)X$, indicates the scale of the structures which give the dominant contribution to the overall energy dissipation rate. These distributions are related to $P(\mathcal{E})$ in the sense that, if we assume that $P(\mathcal{E}) \sim \mathcal{E}^{-\beta}$ and that $\mathcal{E} \sim X^{\lambda}$ for arbitrary β and λ, then energy dissipation will be distributed uniformly across all X if and only if $\beta = 2$. This follows from the conservation of probability,

$$\begin{aligned} E(X)X \sim \mathcal{E}(X)P(X)X &\sim \mathcal{E}(X)\frac{d\mathcal{E}}{dX}P(\mathcal{E})X \\ &\sim X^{\lambda}X^{\lambda-1}(X^{\lambda})^{-\beta}X \\ &\sim X^{\lambda(2-\beta)}. \end{aligned} \tag{5.1}$$

Hence, if power-law scaling is assumed, then a distribution of energy dissipation rates with the critical index is equivalent to energy dissipation being distributed evenly across structures of all scales.

We first discuss the dissipation-weighted distributions for the Euclidean scales. $E(L_e)L_e$, $E(W_e)W_e$ and $E(T_e)T_e$ are shown in Fig. 5.11. We find that energy dissipation is spread nearly uniformly amongst structures with L_e and W_e spanning intermediate to large scales. For W_e, this regime corresponds to inertial-range scales associated with the perpendicular energy cascade; for L_e, the scales are similar but amplified by $B_0/b_{\rm rms}$. The energy dissipated in the large scales does not change significantly with increasing Re, although additional small scales are accessed due to a longer inertial range. In contrast to length and width, the energy dissipation is peaked at very small T_e, deep within the dissipation range. This small thickness accounts for energy dissipation at the bottom of the energy cascade. Energy dissipation peaks at smaller T_e as Re is increased, consistent with a decreasing dissipation scale.

We now compare this to the dissipation-weighted distributions for the Minkowski scales. $E(L_m)L_m$, $E(W_m)W_m$ and $E(T_m)T_m$ are shown in Fig. 5.12. As with the

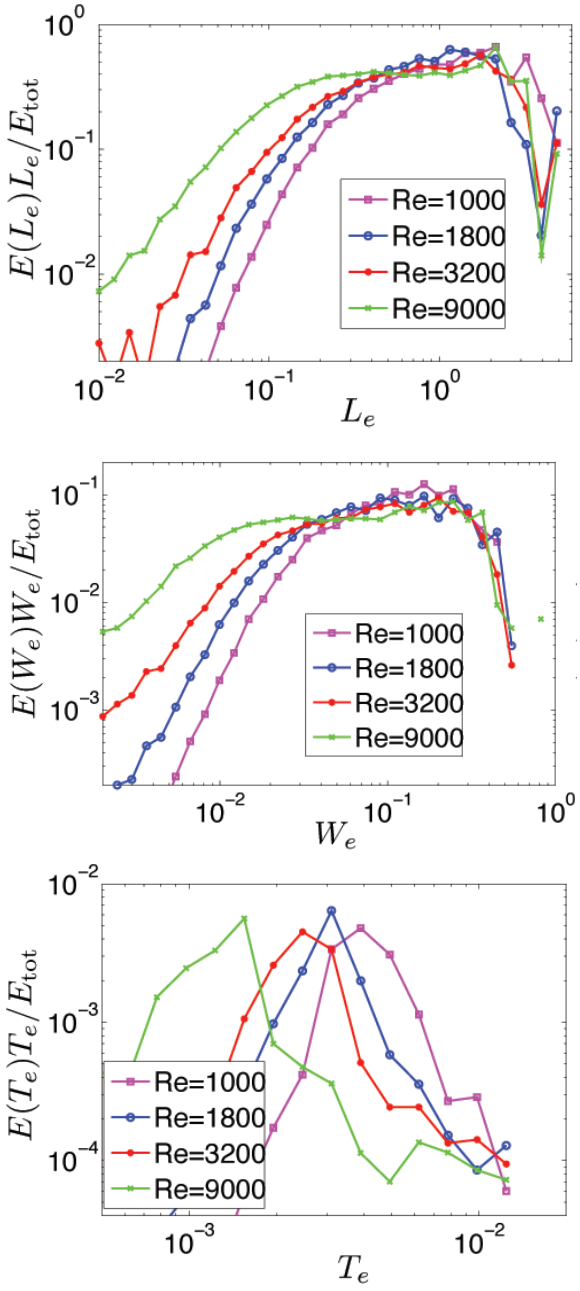

Figure 5.11: The compensated dissipation-weighted distributions $E(X)X$ for Euclidean scales $X \in \{L_e, W_e, T_e\}$ (normalized to total energy dissipation rate $E_{\rm tot}$), for $Re = 1000$ (magenta), $Re = 1800$ (blue), $Re = 3200$ (red), and $Re = 9000$ (green).

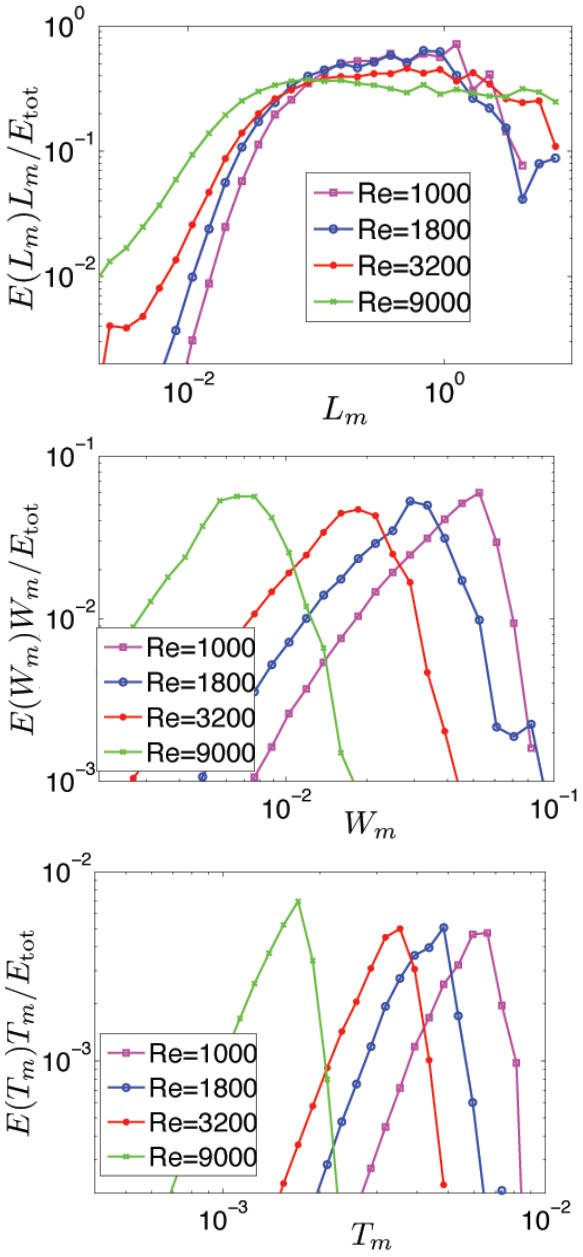

Figure 5.12: The compensated dissipation-weighted distributions $E(X)X$ for Minkowski scales $X \in \{L_m, W_m, T_m\}$ (normalized to total energy dissipation rate $E_{\rm tot}$), for $Re = 1000$ (magenta), $Re = 1800$ (blue), $Re = 3200$ (red), and $Re = 9000$ (green). Comparing with the Euclidean scales in Fig. 5.11, the length and thickness distributions agree for both methods, but the widths show qualitatively different distributions.

Euclidean case, energy dissipation occurs mainly in structures with L_m spread throughout the inertial range and T_m sharply peaked at small scales. However, unlike the Euclidean case where W_e takes a continuum of inertial-range values, W_m is strongly peaked at a scale between the intertial range and dissipation range. In fact, it appears that W_m is representative of the dissipation scale.

The pronounced qualitative difference between W_e and W_m suggests that the two methods are capturing different aspects of the structure. The differences likely stem from the fact that the Minkowski method is more sensitive to the curvature and overall morphology of the structure than the Euclidean method. The Euclidean width, by its simple definition, is a strong upper bound on the perpendicular scale at broadest part of the structure. The fact that it lies in the inertial-range is strongly indicative of the central part of the structure spanning inertial-range scales in the perpendicular direction. There are several effects that could cause the Minkowski method to differ from this interpretation. First, the structure may have an extended dissipation-scale tail which is captured by W_m. Second, there may be dissipation-scale fluctuations along structure, so that W_m represents the characteristic scale for ripples or irregularities. Third, the structure may have several branches, each with widths near the dissipation scale. In any case, it seems reasonable that the fine morphological features of the structure are tied to the dissipation scale, since that is the scale at which current density from the energy cascade accumulates.

The dissipation-weighted distributions in Fig. 5.11 and Fig. 5.12 exhibit unambiguous scaling behavior with Reynolds number, with the lower characteristic scales decreasing with Re. However, it is difficult to get a definitive quantitative measurement for these scalings due to the limited range in Re, uncertainty into how to best normalize the broad distributions for proper comparison, and possible effects of resolution on the scalings (in particular, for the thicknesses). Regardless, we estimate these scalings in Fig. 5.13 by considering the dissipation-weighted distributions for the scales rescaled by powers of Re. We verify the dissipation-range scalings inferred from the unweighted distributions in Fig 5.10: $W_m \sim Re^{-3/4}$, $T_m \sim Re^{-3/5}$, and $T_e \sim Re^{-1/2}$. We also identify new scalings corresponding to the small-scale cutoff for the inertial-range scales. We find that these cutoff scales (denoted by superscript c)

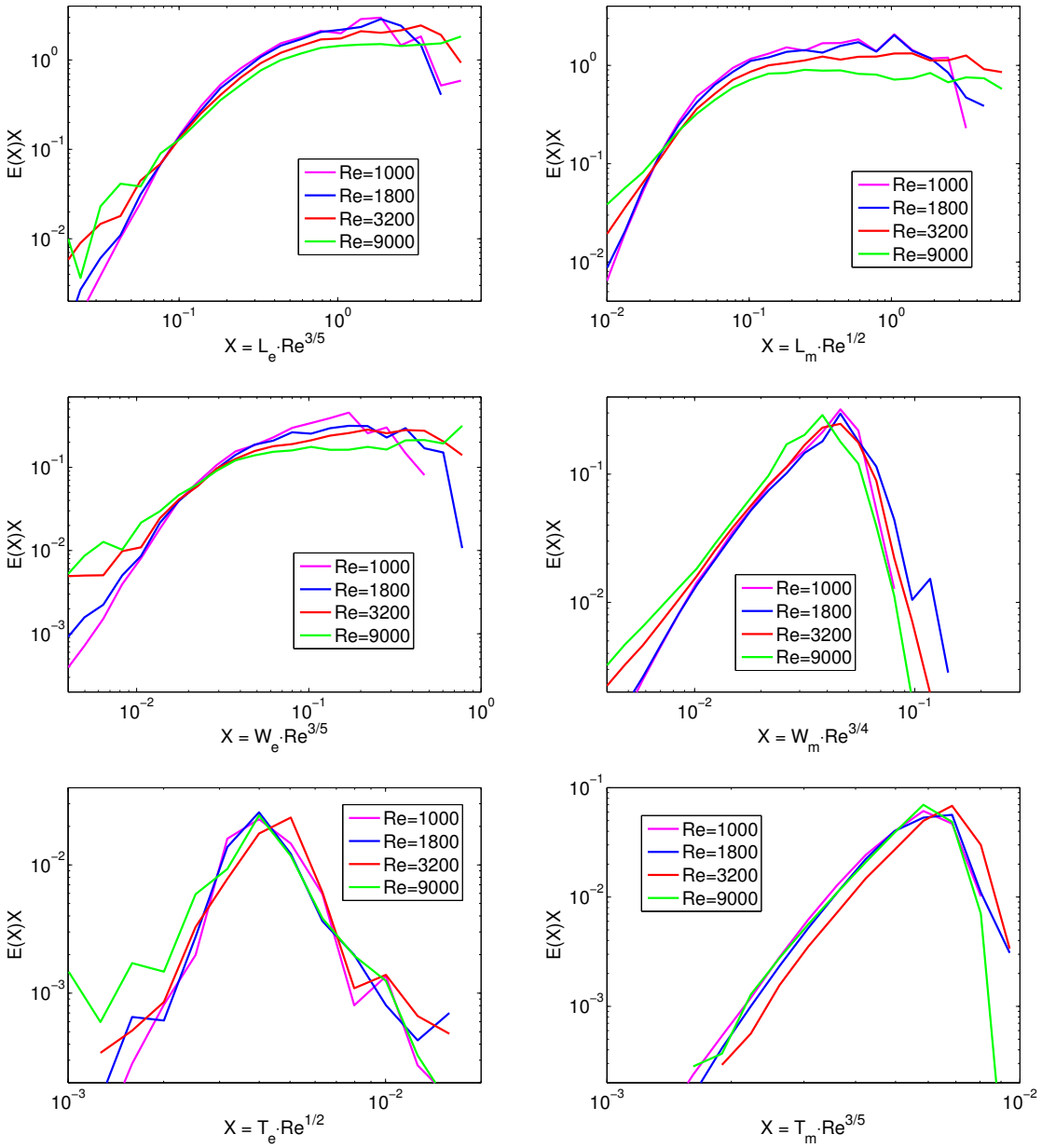

Figure 5.13: Compensated dissipation-weighted distributions for rescaled scales. In descending order in the left column are $L'_e = L_e(Re/Re_0)^{3/5}$, $W'_e = W_e(Re/Re_0)^{3/5}$, and $T'_e = T_e(Re/Re_0)^{1/2}$; in the right column are $L'_m = L_m(Re/Re_0)^{1/2}$, $W'_m = W_m(Re/Re_0)^{3/4}$, and $T'_m = T_m(Re/Re_0)^{3/5}$, where $Re_0 = 1000$ is the reference Reynolds number.

go as $L_e^c \sim W_e^c \sim Re^{-3/5}$ and $L_m^c \sim Re^{-1/2}$. In particular, the scalings of W_m and the L_m^c are consistent with the GS95 prediction of parallel and perpendicular dissipation scales, $l_{\perp,\eta} \sim \eta^{3/4}$ and $l_{\parallel,\eta} \sim \eta^{1/2}$. The shallower scaling of T_m is more uncertain due to resolution effects, and we cannot rule out a scaling closer to $Re^{-3/4}$.

5.4 Scaling of population size

Finally, we remark on the scaling of the population size, i.e., the number of dissipative current sheets per snapshot. The simplest approach is to directly count the unfiltered number of structures in the population. However, this result strongly over-represents the under-resolved structures near the threshold, which significantly contribute to the population size even though they represent a negligible contribution to the energy dissipation. For a more reasonable estimate, we count only the structures with energy dissipation rates greater than a minimum value $Ch^3\eta j_{\text{thr}}^2$, where h^3 is the lattice volume element and $C \geq 1$ is some fixed number. This criterion removes many of the under-resolved, unphysical structures consisting of a few points near the lattice scale. We find that this filtered number of structures, N, strongly increases with Re, as shown in Fig. 5.14 for $C = 8$. This trend is similar for other values of C (including the unfiltered case of $C = 1$), and also for other filtering methods, e.g., volumetric filtering of structures or Fourier space filtering of the fields.

Potentially more meaningful than the total population size is the number of inertial-range structures, N_{inertial}. To determine this quantity, we count only structures in the flat region of the energy distributions in Fig. 5.11 and Fig. 5.12, i.e., with either $L_e > L_e^c$, $L_m > L_m^c$, or $W_e > W_e^c$, where L_e^c, L_m^c, and W_e^c are the Reynolds-number dependent lower cutoff for the inertial-range in $E(L_e)L_e$, $E(L_m)L_m$, and $E(W_e)W_e$, with scalings as implied by Fig. 5.13. As shown in Fig. 5.15, we find that $N_{\text{inertial}} \sim Re^2$ for the inertial-range populations measured from all three distributions.

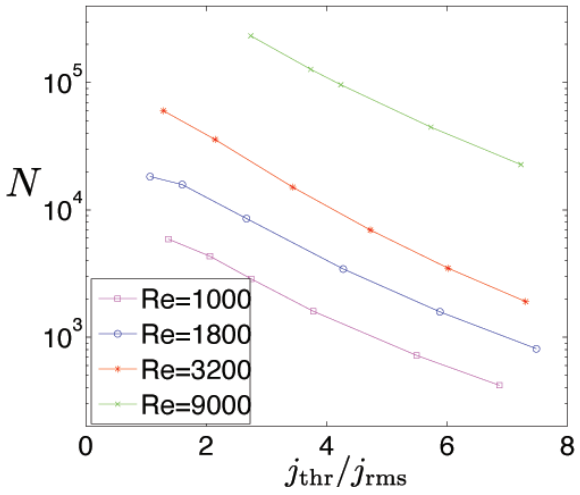

Figure 5.14: The filtered number of structures N per snapshot as a function of the rescaled threshold for $Re = 1000$ (magenta), $Re = 1800$ (blue), $Re = 3200$ (red), and $Re = 9000$ (green). The number of structures at any given threshold increases strongly with Re.

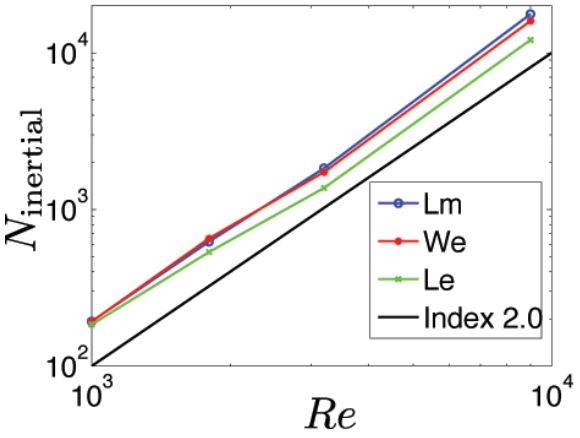

Figure 5.15: Number of inertial-range structures versus Re for the given threshold of $j_{\rm thr}/j_{\rm rms} \approx 3.75$. We find that $N_{\rm inertial} \sim Re^2$ using inertial-range populations for three different quantities: L_e (green), L_m (blue), and W_e (red).

5.5 Summary of spatial analysis

The statistical analysis of dissipative current sheets drives us to conclude that as resistivity of the system is decreased (or equivalently, Re increased), the following scenario occurs. Energy dissipation takes place in a large number of thin, broad, and tightly-packed current sheets spanning a wide range of scales. Since the distribution of energy dissipation rates has a power-law distribution with index very close to, if not exactly equal to, the critical index of -2.0, populations of weak (small) structures and strong (large) structures both contribute equally to the overall energy dissipation. The lengths (and Euclidean widths) of the dissipative structures occupy a continuum of inertial-range scales spanning from the dissipation scale up to the system size. The thicknesses (and Minkowski widths) of the structures decrease in tandem with the dissipation scale, making room for a larger number of structures. The spatial dissipative structures in driven MHD turbulence therefore instantaneously exhibit features of both nanoflares and large-scale coherent structures. However, as we will see in the following chapter, the picture changes once the temporal dynamics of structures are considered.

6 TEMPORAL ANALYSIS

6.1 Overview of temporal analysis

In this chapter, we perform a statistical analysis of spatiotemporal dissipative structures (i.e., flare events) in MHD turbulence, based on the procedure and methods described in Sections 3.3, 3.4, and 3.5. We describe the probability distributions, scalings, and evolution of dissipative processes. We compare our results to the observed statistical properties of solar flares in Sec. 6.8, and summarize our conclusions in Sec. 6.9.

6.2 Simulations for temporal analysis

We first describe the numerical simulations on which the temporal analysis is performed. We consider hundreds of snapshots from four simulations, with the same conditions as described in Section 4.1, and parameters shown in Table 6.1. Durations (and other timescales) are measured in terms of large-scale eddy turnover times of the turbulence, given by $\tau_{\rm eddy} = L_\perp/(2\pi v_{\rm rms}) \approx 1$. The analysis is performed on time intervals of durations $\tau_{\rm tot}$, all of which begin after the simulations reach statistical steady state. Case 1 is a lower-resolution (256^3) run used to establish convergence of the results with resolution. Three independent runs with resolution 512^3 are chosen to study scalings with Re, although the relatively limited range ($Re = 800 - 1800$) inhibits precise measurements of the scalings. Of these runs, Case 3 with $Re = 1250$ is the most robust data set, having the highest cadence, being nominally well-resolved dynamically, and having the longest time interval ($\tau_{\rm tot} = 15.6$).

We analyze snapshots dumped at a cadence $(\Delta t)^{-1}$, with Δt being larger than the internal time step in the simulation. For reference, we now estimate the minimum cadence required to properly track structures between two adjacent snapshots. This is estimated by requiring that the distance advected by the flow during Δt is less than the typical current sheet thickness. Estimating the former as $v_{\rm rms}\Delta t$ and the latter as $b_{\rm rms}/j_{\rm thr}$, we require $\Delta t < b_{\rm rms}/(v_{\rm rms} j_{\rm thr}) \approx 1/j_{\rm thr}$. For the four cases in

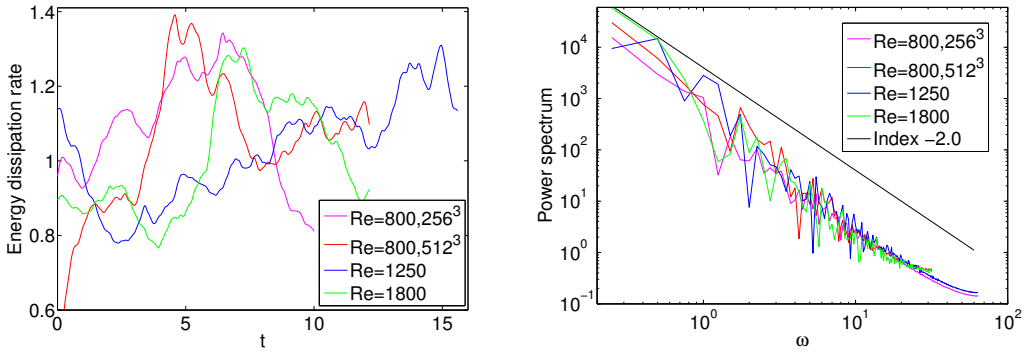

Figure 6.1: Left panel: the total energy dissipation rate in the system for the analyzed interval of time in the four simulations. Right panel: the power spectrum of this time series, showing a power law index near -2. The colors correspond to cases 1 (magneta), 2 (red), 3 (blue), and 4 (green) from Table 6.1.

Table 6.1, we have $j_{\rm rms} \in \{12.1, 11.8, 14.6, 17.4\}$, which gives the condition $\Delta t < \{1/12.1, 1/11.8, 1/14.6, 1/17.4\} j_{\rm rms}/j_{\rm thr}$. The cadences given in Table 6.1 fall short of satisfying this condition for thresholds more than three or four times larger than the rms fluctuations. However, this condition is somewhat alleviated in practice because associations are made for states that do not fully overlap (since displacements of one lattice spacing satisfy spatial connectivity) and the condition is applied to all of the points in the (generally large) structure. Most of the results show robust convergence with, or only weak sensitivity to, cadence.

Table 6.1: Numerical simulations for temporal analysis

Case	Resolution	Re	Δt	$\tau_{\rm tot}$
1	256^3	800	1/64	10.0
2	512^3	800	1/32	12.2
3	512^3	1250	1/64	15.6
4	512^3	1800	1/32	12.2

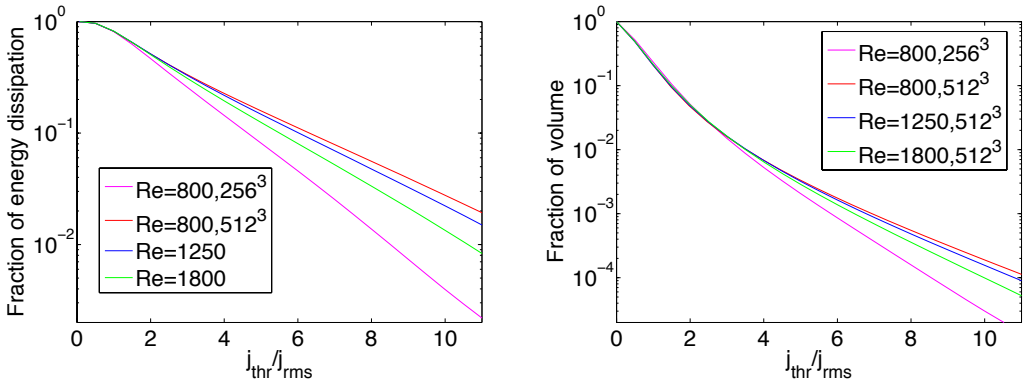

Figure 6.2: The fractions of total energy dissipation (left) and volume (right) in structures with $|j| > j_{\rm thr}$. The curves correspond to cases 1 (magenta), 2 (red), 3 (blue), and 4 (green) from Table 6.1. Cases 2 and 3 are most consistent with the result from fully-resolved simulations used in the spatial analysis (see Fig. 4.2).

6.3 Global results

We first describe the global features of energy dissipation in the simulations. In the first panel of Fig. 6.1, we show the total ohmic energy dissipation rate in the system, $\mathcal{E}_{\rm tot}(t)$, during the given time intervals for all of the simulations in Table 6.1. If we associate the dissipated energy with prompt optically-thin emission, i.e., if we assume that all dissipated energy is converted immediately into radiation in an optically-thin environment, then this represents a light curve for the system. The mean of $\mathcal{E}_{\rm tot}(t)$ is very close to 1.0, in agreement with the energy input from the large-scale forcing. The rms fluctuation about this mean is approximately 0.15 for all cases. In the second panel of Fig. 6.1, we show the power spectra of $\mathcal{E}_{\rm tot}(t)$, which exhibits a power law with index close to -2.0 for all cases.

For reference, we show cumulative distributions of the energy dissipation and volume conditioned on the threshold, as described in Sec. 4.2 for the spatial analysis. The fraction of total energy dissipation occurring in structures with $|j| > j_{\rm thr}$, i.e., $\mathcal{E}_{\rm cum}(j_{\rm thr}/j_{\rm rms})/\mathcal{E}_{\rm tot}$, is shown in Fig. 6.2. We find that this function has a wide tail characteristic of intermittency, declining exponentially at large $j_{\rm thr}$. We also show the fraction of total volume occupied by the same structures, in the second panel

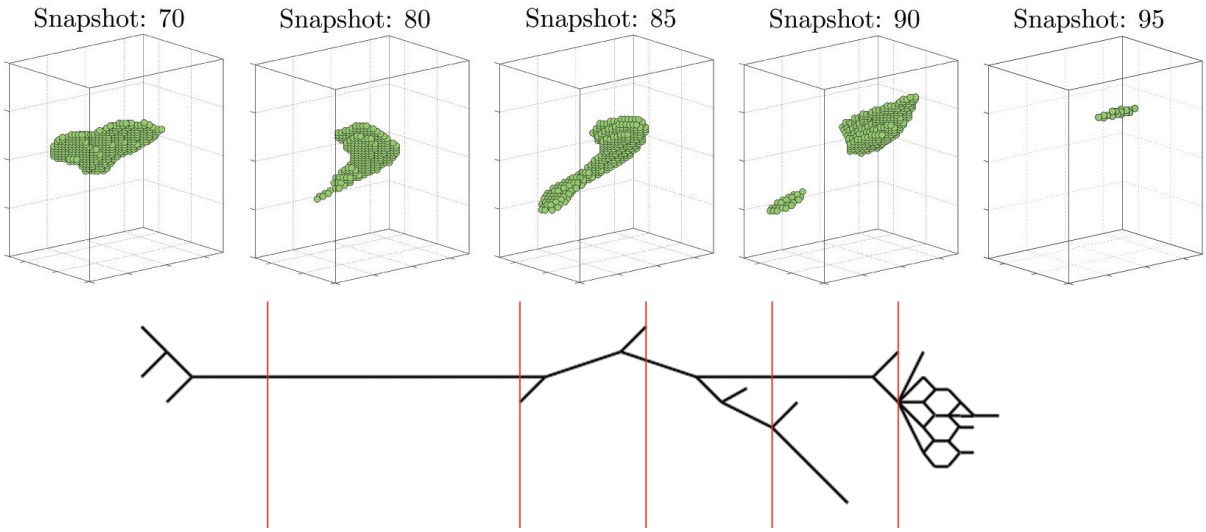

Figure 6.3: An example of a typical process with duration $\tau \approx 0.5$, shown in green on the simulation lattice. A schematic diagram of the process is also shown, with the snapshot times marked by a red line.

of Fig. 6.2. The fraction of energy dissipation always greatly exceeds the occupied volume, with, for example, about 30% of the energy dissipation occurring in 1% of the volume at $j_{\text{thr}}/j_{\text{rms}} \approx 3$. As discussed in Sec. 4.2, the fractions of energy dissipation and occupied volume may both be universal for sufficiently well-resolved, high-Re simulations. Cases 2 and 3 closely match these previous results. Since significant deviations occur at large $j_{\text{thr}}/j_{\text{rms}}$ for the other cases, they may not be completely well-resolved.

Before proceeding to the quantitative analysis of processes in the simulations, we show an example of a relatively simple process in Fig. 6.3. This process has a duration $\tau \approx 0.5$ with 31 distinct paths. Snapshots of a few representative states (in green) are shown on a subdomain of the simulation lattice (with size $0.10 \times 0.14 \times 0.90$). These images do not account for the elongation of the lattice along the (vertical) guide field, which would emphasize the ribbon-like character of the structures. The broadest part of the structure is shown from the given perspective. In addition to these snapshots, we also show the schematic diagram of the process (as established in Sec. 3.3), with

the snapshot times marked in red. It is evident that this process is highlighted by a major division which occurs after the structure is stretched. A disproportionally large number of paths in this case are produced at the final stages of the process, as it decays toward the threshold.

6.4 Aggregate quantities

We now consider some aggregate quantities for the sample of processes in our simulations. Note that occurrence rates are generally not a very robust statistic, since they can be strongly affected by structures near the threshold, which in turn are strongly affected by resolution and cadence. A more robust analysis would filter out the small-scale and under-resolved structures to circumvent these numerical issues. We use no filtering in the present analysis, both for simplicity and because we are only interested in broad trends.

Table 6.2: Aggregate quantities in all cases ($j_{\text{thr}}/j_{\text{rms}} \approx 6.8$, $\Delta t = 1/32$)

Quantity	$256^3, Re = 800$	$512^3, Re = 800$	$512^3, Re = 1250$	$512^3, Re = 1800$
$\langle N_{\text{state}} \rangle$	194	288	657	1328
N_{proc}	914	1271	4272	11608
$N_{\text{proc}}/N_{\text{path}}$	0.218	0.240	0.278	0.339
$N_{\text{int}}/N_{\text{isol}}$	0.278	0.329	0.187	0.115
$N_{\text{mer}}/N_{\text{div}}$	0.839	0.776	0.800	0.823
$N_{\text{form}}/N_{\text{des}}$	0.871	0.853	0.886	0.911
$N_{\text{n-vert}}/N_{\text{3-vert}}$	0.341	0.353	0.485	0.523

Some general results are shown in Table 6.2 for all of the simulations with fixed threshold $j_{\text{thr}}/j_{\text{rms}} \approx 6.8$ and cadence $\Delta t^{-1} = 32$. Here, N_{proc} is the number of processes, N_{path} is the number of paths, N_{int} is the number of processes with interactions (i.e., processes consisting of more than one path), N_{isol} is the number of isolated structures (i.e., processes consisting of one path), N_{mer} is the number of merger events (where a vertex with n ingoing paths counts as $n-1$ mergers), N_{div} is the number of division events (where a vertex with n outgoing paths counts as $n-1$ divisions), N_{form} is the number of formation events (i.e., the number of paths with no

predecessors), N_{des} is the number of destruction events (i.e., the number of paths with no successors), $N_{\text{3-vert}}$ is the number of three-point vertices, and $N_{\text{n-vert}}$ is the number of n-point vertices with $n > 3$. All of these preceding quantities are normalized to the number per eddy turnover time. We also show the mean number of states per snapshot, $\langle N_{\text{state}} \rangle$. Table 6.2 mainly shows the ratios of these various quantites; see the much more detailed Table A.1 in the Appendix for actual occurrence rates.

We now make several remarks about Table 6.2. First, $\langle N_{\text{state}} \rangle$ and N_{proc} in Case 1 are smaller than the corresponding values for the higher-resolution Case 2, with a discrepancy of about 30%. In fact, there is a similar discrepancy in the number of occurrences for all measured quantities (see Table A.1 in Appendix). This can be attributed to the fact that Case 1 is somewhat under-resolved and therefore misses some of the small-scale dynamics present in Case 2. Second, $\langle N_{\text{state}} \rangle$ and N_{proc} both strongly increase with Re, obeying estimated scalings of $\langle N_{\text{state}} \rangle \sim Re^{1.9}$ and $N_{\text{proc}} \sim Re^{2.7}$. Third, three-point vertices are more common than higher-order vertices, although the higher-order vertices still occur in significant numbers. Higher-order vertices appear to be an unavoidable consequence of time discretization. Indeed, the ratio $N_{\text{n-vert}}/N_{\text{3-vert}}$ increases with Re, implying that interactions occur over smaller timescales for higher Re. Fourth, although there are fewer processes with interactions than processes with no interactions, they contain the majority of the paths (i.e., $N_{\text{proc}}/N_{\text{path}} < 1/2$). Fifth, divisions are somewhat more common than mergers, implying a time asymmetry in the interactions. Equivalently, there are more destructions than formations. This asymmetry is reasonable since the time-reversal symmetry of the ideal MHD equations is broken by resistive and viscous dissipation. The preference for divisions over mergers may be a manifestation of the direct cascade of energy from large scales to small scales.

We next consider the effect of cadence, Δt^{-1}, on the above quantities. We show the various quantities from Case 3 for $1/64 \leq \Delta t \leq 1/4$ in Table 6.3. Most quantities monotonically increase when the cadence is increased, or equivalently, Δt is decreased (see Table A.2 and Table A.3 in the Appendix). However, N_{proc} first increases then decreases with cadence, showing a local maximum near $\Delta t \approx 1/16$. This unintuitive result may be explained as follows. Although the number of paths

always increases with cadence, the connectivity of paths changes. For low cadence, paths tend to be isolated structures. This may be a sign that the cadence is insufficient to properly track structures - in particular, in the limit of very large Δt, snapshots become completely uncorrelated, so most processes appear as single states, therefore $N_{\rm proc} \sim (\tau_{\rm tot}/\Delta t)\langle N_{\rm state}\rangle$. For intermediate cadence (i.e., once structures are properly tracked), the paths interact more often when cadence increases, eventually decreasing $N_{\rm proc}$ due to the combining of isolated structures. The transition between these two regimes can be expected when $N_{\rm proc}/N_{\rm path} \approx 1/2$, which is close to the local peak in $N_{\rm proc}$ near $\Delta t \approx 1/16$ for this case. For very high cadence, $N_{\rm proc}$ either saturates or increases once again. The latter scenario may occur if additional isolated structures appear at the shortest time-scales, or if the processes are fractal. This trend is observed for Case 1 (see Table A.2 in the Appendix).

Table 6.3: Variation of aggregate quantities with cadence (Case 3: $512^3, Re = 1250, j_{\rm thr}/j_{\rm rms} \approx 6.8$)

Quantity	$\Delta t = 1/64$	$\Delta t = 1/32$	$\Delta t = 1/16$	$\Delta t = 1/8$	$\Delta t = 1/4$
$N_{\rm proc}$	3311	4272	4908	3704	2197
$N_{\rm proc}/N_{\rm path}$	0.120	0.278	0.562	0.780	0.895
$N_{\rm int}/N_{\rm isol}$	0.429	0.176	0.067	0.030	0.016
$N_{\rm mer}/N_{\rm div}$	0.845	0.799	0.797	0.771	0.778
$N_{\rm form}/N_{\rm des}$	0.831	0.886	0.953	0.978	0.992
$N_{\text{n-vert}}/N_{\text{3-vert}}$	0.367	0.485	0.607	0.697	0.772

Finally, we consider the effect of the threshold, $j_{\rm thr}$, on the above quantities. We show the various quantities from Case 3 for $5.5 \leq j_{\rm thr}/j_{\rm rms} \leq 9.6$ in Table 6.4. For these relatively high thresholds, the occurrence rates for all quantities increase as $j_{\rm thr}$ decreases, due to the larger sample size of paths (see Table A.4 in the Appendix). In particular, we estimate that $\langle N_{\rm state}\rangle \sim j_{\rm thr}^{-3.5}$ and $N_{\rm path} \sim j_{\rm thr}^{-3.1}$, although these must deviate from a power law as $j_{\rm thr} \to j_{\rm rms}$. In contrast, the ratios of the occurrence rates change relatively little. The asymmetry of interactions decreases and the relative proportion of isolated structures increases as $j_{\rm thr}$ decreases, likely due to a larger sample of small structures near the threshold.

The onset of percolation occurs near $j_{\text{thr}}/j_{\text{rms}} \approx 6.8$ for structures through space (in the periodic domain along the guide field, when $\max\{L\} \to L_{\parallel}/(2\pi)$), and near $j_{\text{thr}}/j_{\text{rms}} \approx 5.5$ for processes through the given time interval (when $\max\{\tau\} \to \tau_{\text{tot}}$). We call this latter quantity the percolation threshold, which, in the limit $\tau_{\text{tot}} \to \infty$, is a fundamental characteristic current density of the system. For j_{thr} below the percolation threshold, the initial processes and final processes (defined in Sec. 3.4) contain a large fraction of the dissipated energy, as can be seen in Table 6.4 from $E_{\text{interior}}/E_{\text{all}}$, which is the ratio of energy dissipated by interior processes (i.e., processes that contain no states from the initial or final snapshots), E_{interior}, to energy dissipated by all processes (including initial and final processes), E_{all}. This ratio is large (i.e., $E_{\text{interior}}/E_{\text{all}} > 0.7$) until the percolation threshold is approached near $j_{\text{thr}}/j_{\text{rms}} \approx 5.5$, where the ratio quickly becomes small ($E_{\text{interior}}/E_{\text{all}} \sim 0.29$). The percolation threshold sets a practical limit on the smallest threshold for a reliable temporal analysis, since percolation otherwise interferes with the statistics of structures at the largest scales.

Table 6.4: Variation of aggregate quantities with threshold (Case 3: 512^3, $Re = 1250$, $\Delta t = 1/64$)

Quantity	$j_{\text{thr}}/j_{\text{rms}} \approx 9.6$	$j_{\text{thr}}/j_{\text{rms}} \approx 8.2$	$j_{\text{thr}}/j_{\text{rms}} \approx 6.8$	$j_{\text{thr}}/j_{\text{rms}} \approx 5.5$
$\langle N_{\text{state}} \rangle$	190	343	657	1287
N_{proc}	1105	1777	3311	6314
$N_{\text{proc}}/N_{\text{path}}$	0.139	0.125	0.120	0.116
$N_{\text{int}}/N_{\text{isol}}$	0.491	0.481	0.429	0.383
$N_{\text{mer}}/N_{\text{div}}$	0.825	0.832	0.845	0.863
$N_{\text{form}}/N_{\text{des}}$	0.820	0.820	0.831	0.869
$N_{\text{n-vert}}/N_{\text{3-vert}}$	0.313	0.331	0.367	0.400
$E_{\text{interior}}/E_{\text{all}}$	0.88	0.86	0.70	0.29
$\max\{L\}$	2.6	3.3	6.0	6.0
$\max\{W\}$	0.32	0.33	0.44	0.55
$\max\{\tau\}$	3.3	3.9	8.5	13.8

6.5 Probability distributions and scaling relations

We now describe the probability distributions for the process characteristics, defined in Sec. 3.5. For clarity, we focus on Cases 2-4, which have resolution 512^3 and varying Re. We choose a relatively high threshold of $j_{\text{thr}}/j_{\text{rms}} \approx 6.8$, which is well above the percolation threshold. We retain initial and final processes for better statistics. The distributions are converged with respect to cadence and resolution (based on a comparison between Case 1 and Case 2 in Table 6.1), although it is possible that they have not fully converged with Re.

We begin with the distribution for dissipated energy, $P(E)$, shown in the first panel of Fig. 6.4. We find that $P(E)$ has a power law tail with index near -1.75 ± 0.1. The power law region extends across approximately three orders of magnitude in E, from $E \approx 10^{-5}$ up to about $E \approx 10^{-2}$. For smaller E, the distribution is shallower and appears to be non-universal, likely due to a combination of dissipation-range effects and threshold effects. With increasing Re, the power law extends to smaller E, consistent with a longer inertial range. If we instead consider the distribution for dissipated energy in isolated structures or in paths alone, then there is no clear power law.

The distribution for the peak energy dissipation rate, $P(\mathcal{E}_{\text{max}})$, is shown in the second panel of Fig. 6.4. We find that $P(\mathcal{E}_{\text{max}})$ has a power law with index close to -2.0 ± 0.1 in the range $\mathcal{E}_{\text{max}} \approx 10^{-4}$ to $\mathcal{E}_{\text{max}} \approx 10^{-2}$. Incidentally, this index is also observed in the distribution for energy dissipation rates, $P(\mathcal{E})$, obtained from the analysis of spatial structures, i.e. states, shown in the third panel of Fig. 6.4. The power law index of -2.0 for $P(\mathcal{E})$ is in agreement with the results from the spatial analysis (shown in Fig. 5.8). As will be shown analytically in Sec. 6.7, if one assumes that all processes are single paths that evolve with identical, self-similar functional forms, then the indices for $P(\mathcal{E}_{\text{max}})$ and $P(\mathcal{E})$ must be equal.

The distribution for process duration τ is shown in the first panel of Fig. 6.5. The durations extend to well above an eddy turnover time, sometimes comparable to τ_{tot}. The distribution from $\tau \approx 0.2$ to $\tau \approx 8$ can be fit by a power law with

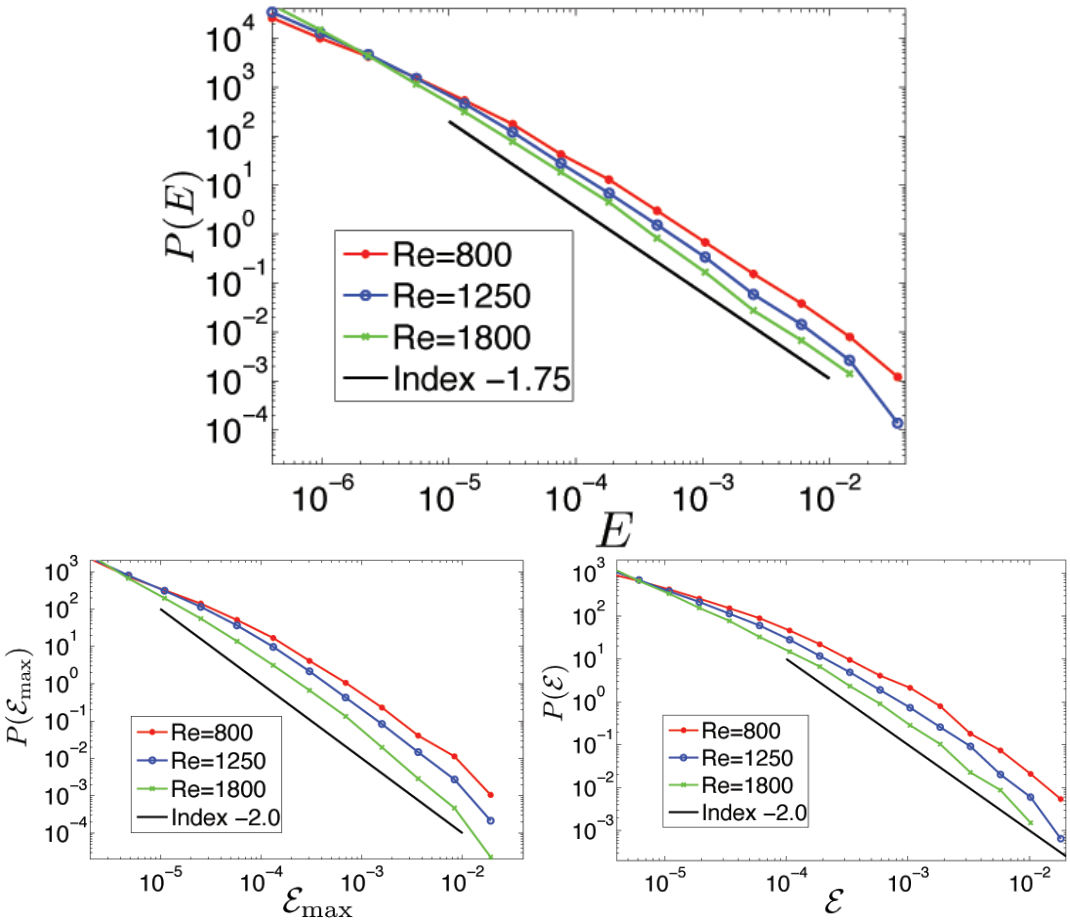

Figure 6.4: The distributions for dissipated energy E, peak energy dissipation rate $\mathcal{E}_{\max}$, and energy dissipation rate (of states) $\mathcal{E}$. These have power laws with index close to -1.75 for $P(E)$ and -2.0 for $P(\mathcal{E}_{\max})$ and $P(\mathcal{E})$. The curves correspond to $Re = 800$ (red), $Re = 1250$ (blue), and $Re = 1800$ (green).

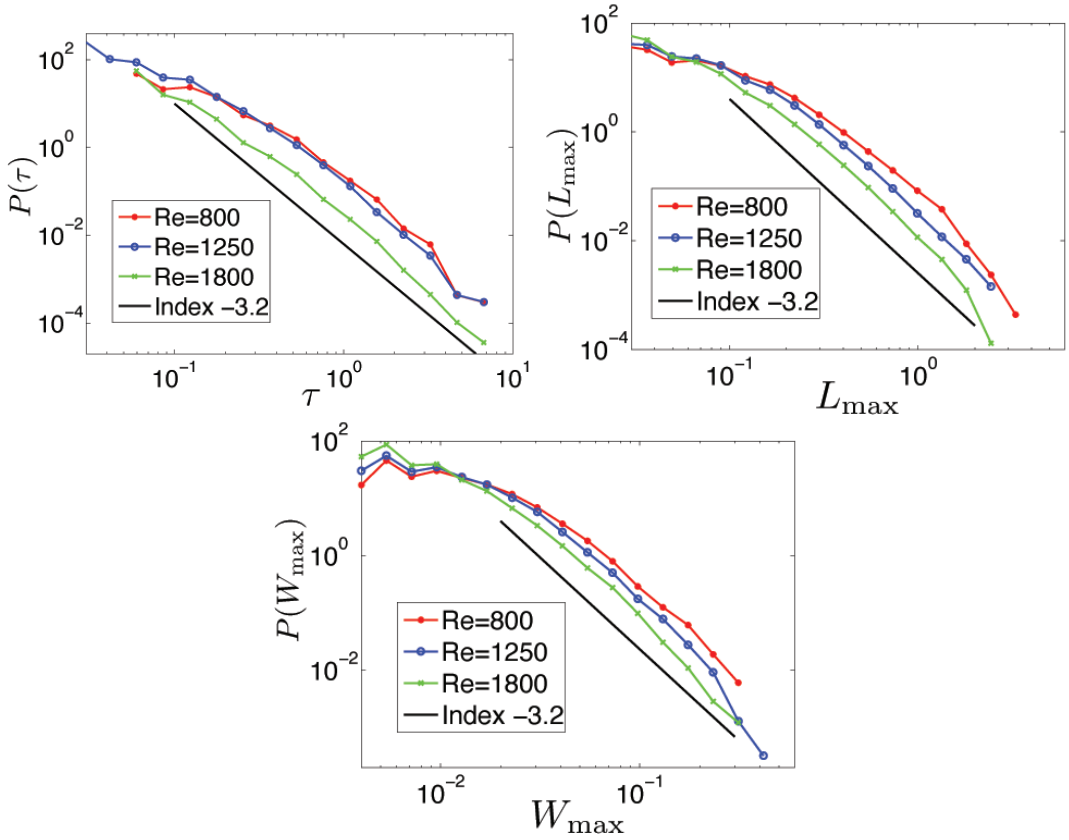

Figure 6.5: The distributions for duration τ, maximum length $L_{\max}$, and maximum width $W_{\max}$, all showing power laws with index near -3.2. The curves correspond to $Re = 800$ (red), $Re = 1250$ (blue), and $Re = 1800$ (green).

index near -3.2 ± 0.2. Likewise, the distributions for maximum length $L_{\max}$ and maximum width $W_{\max}$ have power laws with indices near -3.2, also shown in Fig. 6.5. The distributions for all of these geometric quantities are related due to the strong correlations, described later in this section.

We now remark on the distribution for maximum thickness. As shown in the first panel of Fig. 6.6, $P(T_{\max})$ peaks at the lattice scale, $h = 1/512 \approx 0.002$ (in units of system size, $L_\perp$). This is mainly due to the large population of under-resolved structures near the threshold. It is therefore more transparent to consider the dissipation-weighted distribution, i.e., the distribution weighted by the dissipated

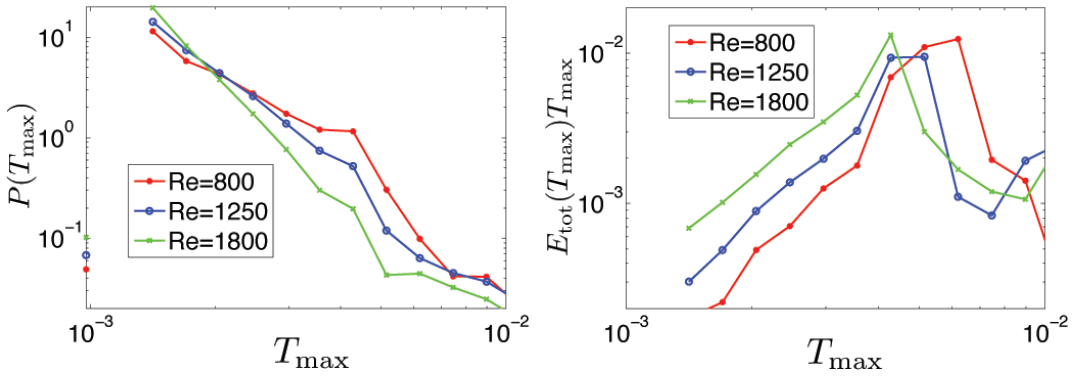

Figure 6.6: Left panel: the distribution for maximum thickness $T_{\max}$, which peaks at the lattice scale, $h \approx 0.02$. Right panel: the same distribution weighted by dissipated energy and compensated by $T_{\max}$, showing that energy dissipation is dominated by processes with thicknesses a few times larger than the lattice scale. The curves correspond to $Re = 800$ (red), $Re = 1250$ (blue), and $Re = 1800$ (green).

energy of the processes, which we denote $E_{\rm tot}(T_{\max})$. As shown in Fig 6.6, the compensated dissipation-weighted distribution $E_{\rm tot}(T_{\max})T_{\max}$ is strongly peaked at $T_{\max}$ a few times larger than the grid scale by (peaking at 2 to 3 times h, depending on Re). In agreement with the analysis in Chapter 5, the thickness shows a very small spread of values.

Finally, we consider the distribution for the number of paths per process, $N_{\rm path}$, which is shown in Fig. 6.7. We find that $P(N_{\rm path})$ shows a robust power law with index near -2.0 ± 0.2. The most complex processes have $\sim 10^3$ paths. It is remarkable that $P(N_{\rm path})$ shows such a robust power law across nearly the entire range of values (roughly $1 < N_{\rm path} < 4 \times 10^3$), since, a priori, it is not clear that the number of paths is a robust physical quantity.

All of the distributions described above are insensitive to the threshold for large enough thresholds. As an example, we show $P(\mathcal{E})$ and $P(\tau)$ for $4.1 \leq j_{\rm thr}/j_{\rm rms} \leq 9.6$ in Fig. 6.8. The distributions are similar in all cases with thresholds above the percolation threshold $j_{\rm thr}/j_{\rm rms} \approx 5.5$. Deviations in the tails of both distributions are discernable when $j_{\rm thr}/j_{\rm rms} = 5.5$ and are more evident when $j_{\rm thr}/j_{\rm rms} = 4.1$, well below the percolation threshold. The percolation of processes steepens the tails of

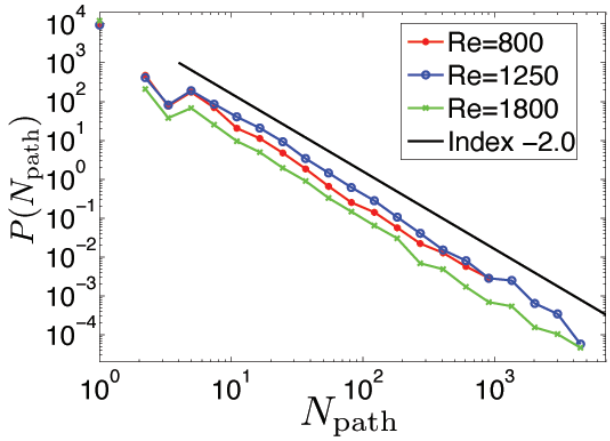

Figure 6.7: The probability distribution for the number of paths per process, which is well fit by a power law with index -2.0. The most complex processes contain thousands of paths. The curves correspond to $Re = 800$ (red), $Re = 1250$ (blue), and $Re = 1800$ (green).

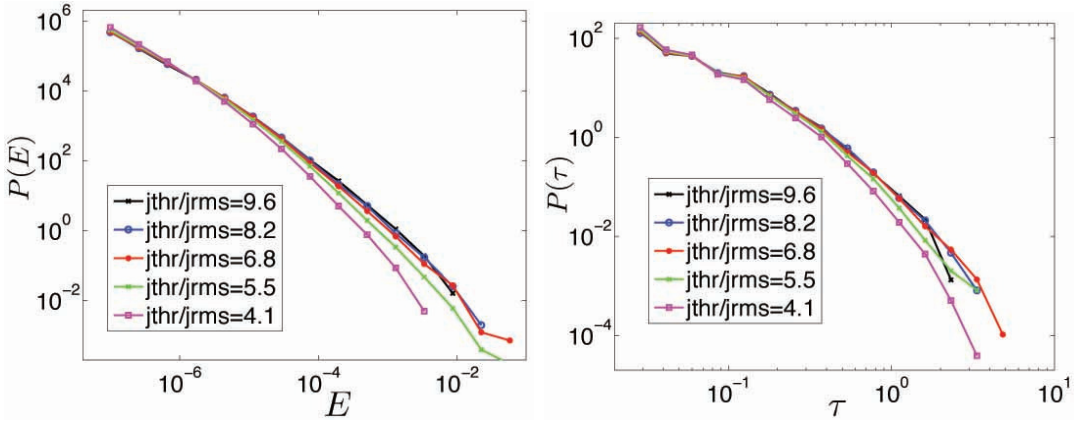

Figure 6.8: The probability distributions $P(\mathcal{E})$ (left) and $P(\tau)$ (right) at various $j_{\mathrm{thr}}/j_{\mathrm{rms}}$. The distributions are affected by percolation through the time interval for thresholds below $j_{\mathrm{thr}}/j_{\mathrm{rms}} = 5.5$ (green), visible in the curve for $j_{\mathrm{thr}}/j_{\mathrm{rms}} = 4.1$ (magenta).

the distributions, consistent with undercounting the large-scale processes.

We now describe the scaling relations between the various process characteristics. We show scatter plots of the different quantities versus process duration τ in Fig. 6.9. For clarity, these are only shown for Case 3, with similar scalings for all other cases. We find that $L_{\max} \approx 6W_{\max} \approx 0.6\tau$, $\mathcal{E}_{\max} \sim V_{\max} \sim \tau^2$, and $E \approx (3\times10^{-4})\tau^3$. We find that $T_{\max}$ exhibits no evident correlation with τ or other quantities. Therefore, to a good approximation, the thickness is constant. These scalings are then consistent with the simple geometric estimates, $V_{\max} \sim L_{\max}W_{\max}T_{\max} \sim \tau^2$, $\mathcal{E}_{\max} \sim V_{\max}\eta j_{\rm thr}^2 \sim \tau^2$, and $E = \int dt \int dV \eta j^2 \approx \tau V_{\max}\eta j_{\rm thr}^2 \sim \tau^3$ based on the other correlations, assuming that the thickness and typical current densities are constant.

A constraint between the indices of the distributions can be derived analytically if all processes are assumed to be single paths evolving with identical, rescaled functional forms. In this case, $E \sim \mathcal{E}_{\max}\tau$ is an exact relation; this is described later in Sec. 6.7 for a derivation of this result. In addition, the distributions and scaling relations can be checked for self-consistency by using the conservation of probability. For example, one may suppose that $P(\mathcal{E}_{\max}) \sim \mathcal{E}_{\max}^{-2}$, which implies that the distribution for peak energy dissipation rates is not dominated by weak or strong events. Then the measured scaling relations, $\mathcal{E}_{\max} \sim \tau^2$ and $E \sim \tau^3 \sim \mathcal{E}_{\max}^{3/2}$, fix the indices of the other distributions. In this case, $P(E) = P(\mathcal{E}_{\max})\, d\mathcal{E}_{\max}/dE \sim E^{-5/3}$, which is relatively close to our measured index near -1.75. The scalings then also imply that $P(\tau) \sim \tau^{-3}$, consistent with our measured index of -3.2. In general, it is clear that $P(E)$ should be somewhat shallower than $P(\mathcal{E}_{\max})$ due to integration across the duration, which increases with $\mathcal{E}_{\max}$.

6.6 Process evolution

We now present results on the temporal evolution of individual processes. The following information is based on the time-series of instantaneous characteristics for each process, obtained from the constituent states at each snapshot. In general, the evolution of a given process is irregular and chaotic - in particular, long-lived processes are marked by frequent interactions and various phases of growth and decline. For

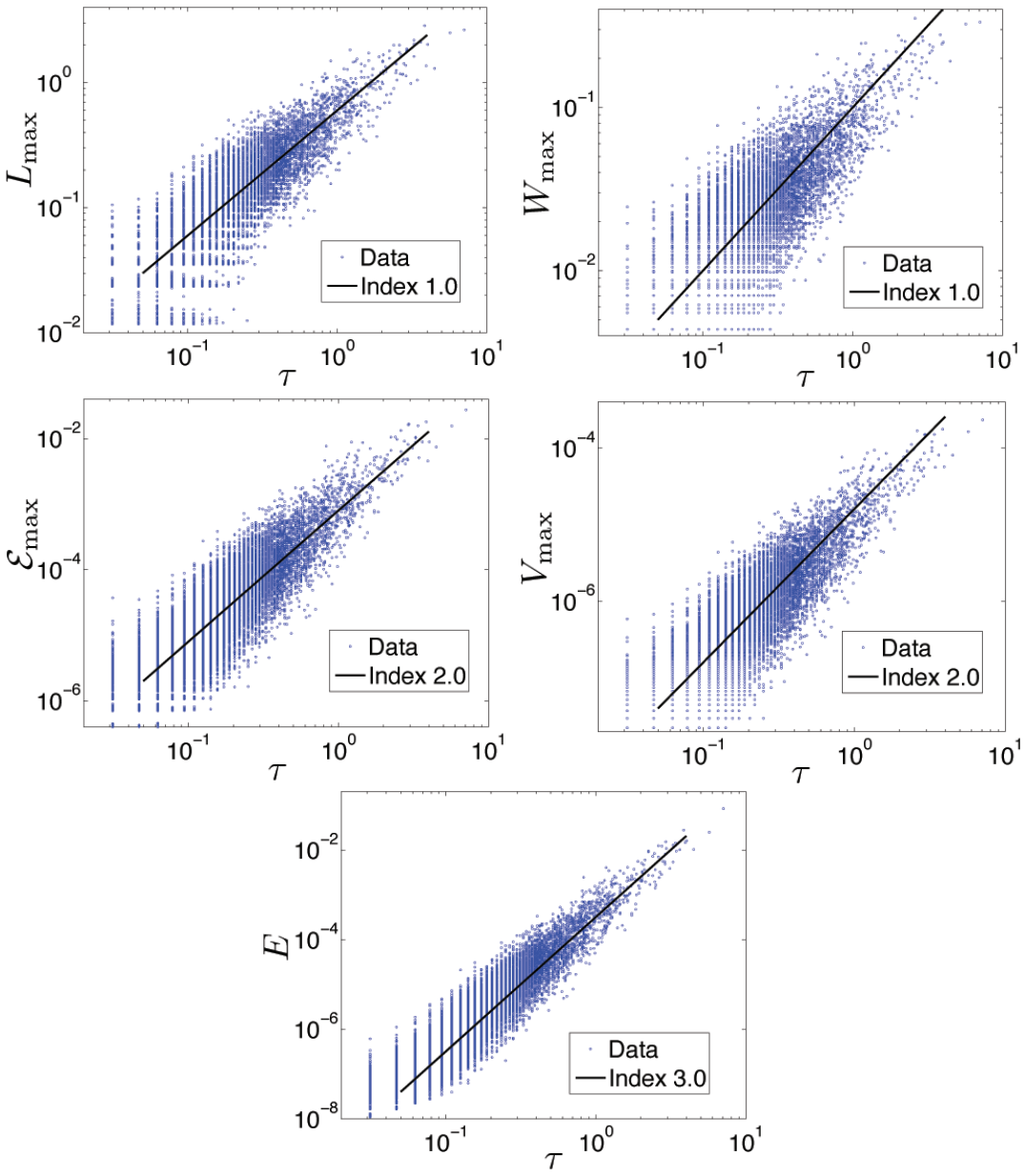

Figure 6.9: Scatter plots of maximum length $L_{\max}$, maximum width $W_{\max}$, peak energy dissipation rate $\mathcal{E}_{\max}$, peak volume $V_{\max}$ (relative to the system volume), and dissipated energy E versus the process duration τ.

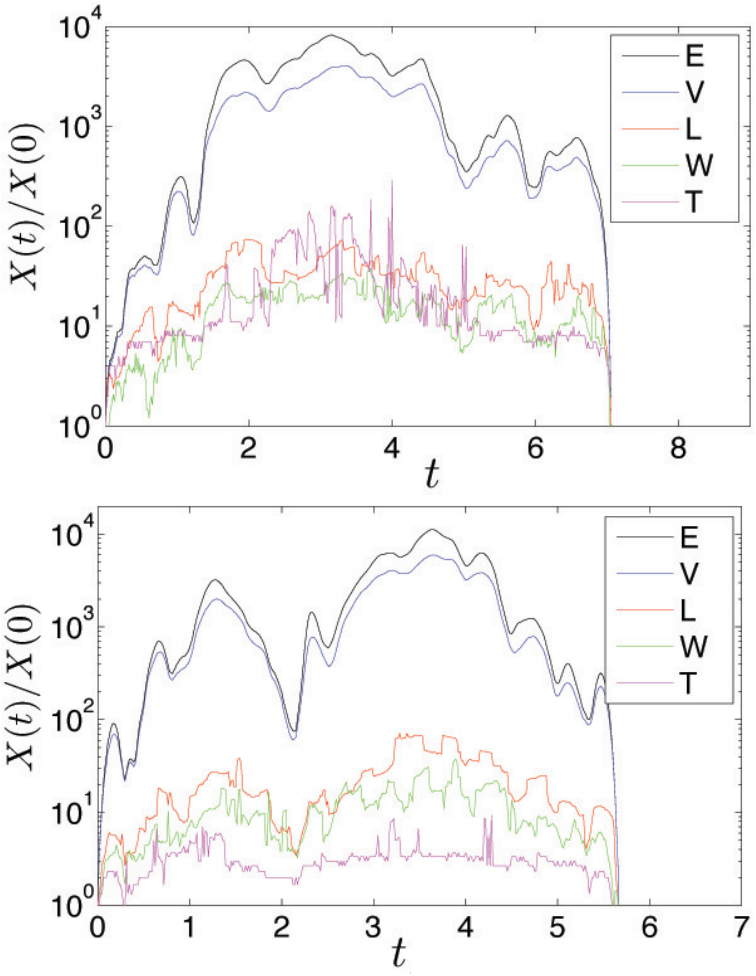

Figure 6.10: The evolution of several characteristics for the two longest processes for the $Re = 1250$ case. The curves correspond to energy dissipation rate $\mathcal{E}$ (black), volume V (blue), length L (red), width W (green), and thickness T (magenta).

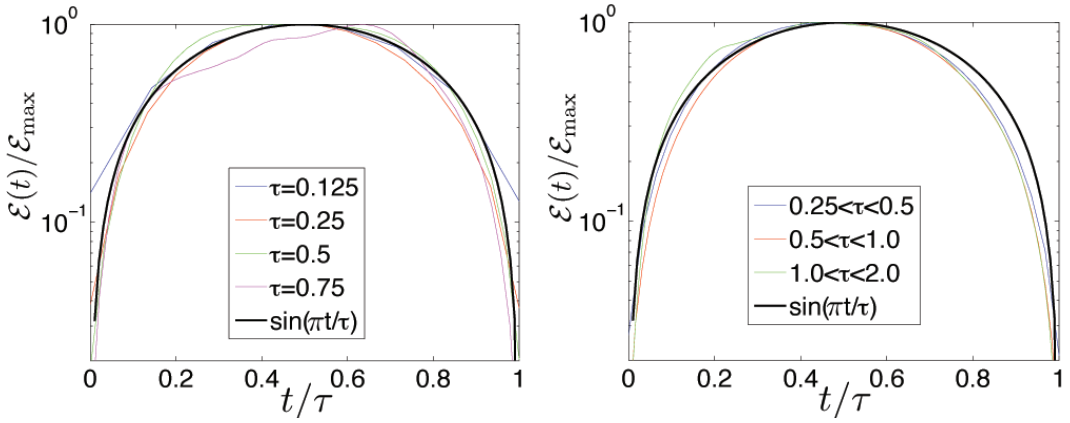

Figure 6.11: Energy dissipation rate versus time, averaged for all processes of given durations (left) and all processes in given intervals of durations (right). Also shown in black is the fit by a sine function.

example, the evolution of several characteristics for the two longest processes in Case 3 (at $j_{\rm thr}/j_{\rm rms} = 6.8$), which have durations of $\tau \approx 7.1$ and 5.7, are shown in Fig. 6.10. These processes begin by rapid growth, followed by a relatively steady phase that is randomly kicked via interactions, and end by rapid decay toward the threshold. We investigate the evolution of a typical process by averaging over all processes of a given duration.

To be concrete, we focus on the evolution of energy dissipation rate, $\mathcal{E}(t)$ for $0 < t < \tau$. Shown in the left panel of Fig. 6.11 is the averaged energy dissipation rate normalized to peak energy dissipation rate, $\mathcal{E}(t/\tau)/\mathcal{E}_{\rm max}$, versus time normalized to duration, t/τ, for processes of durations $\tau \in \{0.125, 0.25, 0.5, 0.75\}$ in Case 3. The evolution is well approximated by a single sine mode, $\mathcal{E}(t/\tau)/\mathcal{E}_{\rm max} \approx \sin(\pi t/\tau)$, independent of τ. Since the long-lived processes have a similar evolution as short-lived processes (with time normalized to duration and energy dissipation rate normalized to the corresponding peak value), it is reasonable to average the statistics over structures with varying τ. This type of average is shown in the right panel of Fig. 6.11 for all processes with τ in the intervals $\{(0.25, 0.5), (0.5, 1), (1, 2)\}$. The averaged $\mathcal{E}(t/\tau)/\mathcal{E}_{\rm max}$ continues to follow the same form up to $\tau \approx 2$, above which the statistical sample becomes limited.

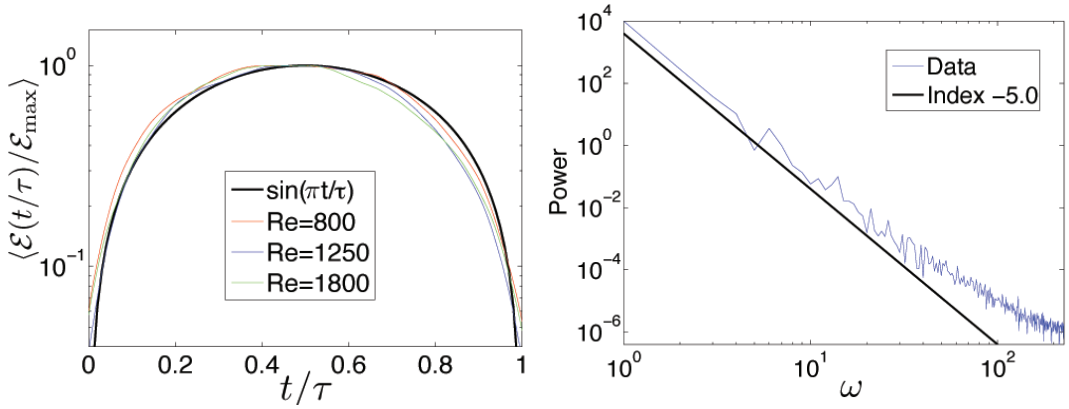

Figure 6.12: Left panel: the evolution of energy dissipation rate $\langle \mathcal{E}(t/\tau)/\mathcal{E}_{\max} \rangle$ versus time t/τ, with the average performed across processes of all durations. The fit by $\sin(\pi t/\tau)$ (shown in black) works very well. The colors correspond to $Re = 800$ (red), $Re = 1250$ (blue), and $Re = 1800$ (green). Right panel: the power spectrum of $\langle \mathcal{E}(t/\tau)/\mathcal{E}_{\max} \rangle$ for the $Re = 1250$ case, showing a very steep descent as a power law with index near -5.0 at low ω.

We next perform an average over processes of all durations to obtain $\langle \mathcal{E}(t/\tau)/\mathcal{E}_{\max} \rangle$, shown for Cases 2-4 in Fig. 6.12. It is clear that $\langle \mathcal{E}(t/\tau)/\mathcal{E}_{\max} \rangle \approx \sin(\pi t/\tau)$ holds to a very good approximation. For a more quantitative analysis, we show the power spectrum of $\langle \mathcal{E}(t/\tau)/\mathcal{E}_{\max} \rangle$ for Case 3 in the right panel of Fig. 6.12, which has a very steep decline in power going approximately as ω^{-5} at low ω, confirming that the $\omega = 1$ mode strongly dominates. The geometric characteristics V, L, W, and T show a similar temporal evolution as $\mathcal{E}$, consistent with the strong correlations.

Next we consider the temporal evolution of the instantaneous number of states involved in the process, $N_{\text{states}}(t/\tau)$. This is shown for Case 3 in Fig. 6.13, with averages performed across durations in the four intervals $\{(0, 0.5), (0.5, 1), (1, 1.5), (1.5, 2)\}$ (left panel) and across all durations (right panel). The functional form of $N_{\text{states}}(t)$ exhibits clear qualitative differences from $\mathcal{E}(t)$ and the geometric characteristics. The average across all durations can be approximated as a triangle function, i.e., linearly increasing in time and then linearly decreasing in time.

Although $\mathcal{E}(t)$ and $N_{\text{states}}(t)$ are symmetric to a good approximation, a small asymmetric component can be discerned from Figs. 6.12 and 6.13. This asymmetry

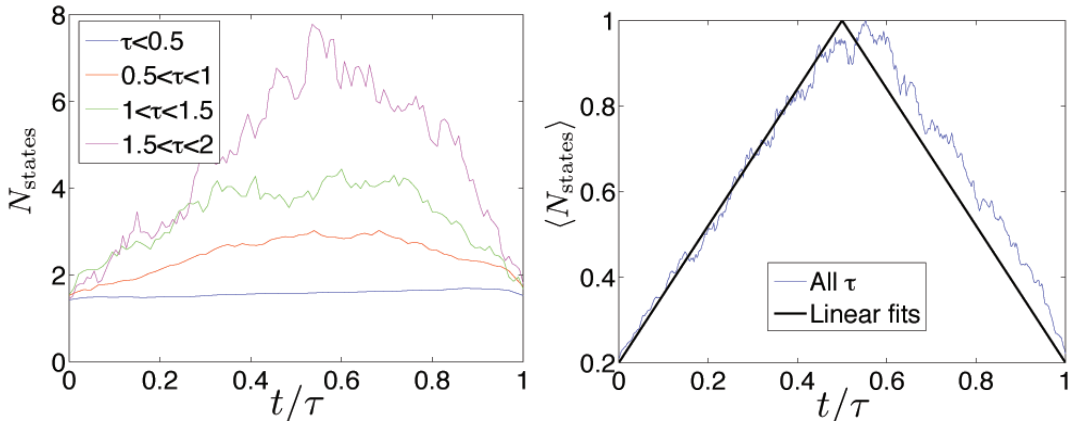

Figure 6.13: The instantaneous number of states in the process, $N_{\text{states}}(t/\tau)$, across the duration of the process, averaged for processes with durations in given intervals (left) and for processes with all durations (right).

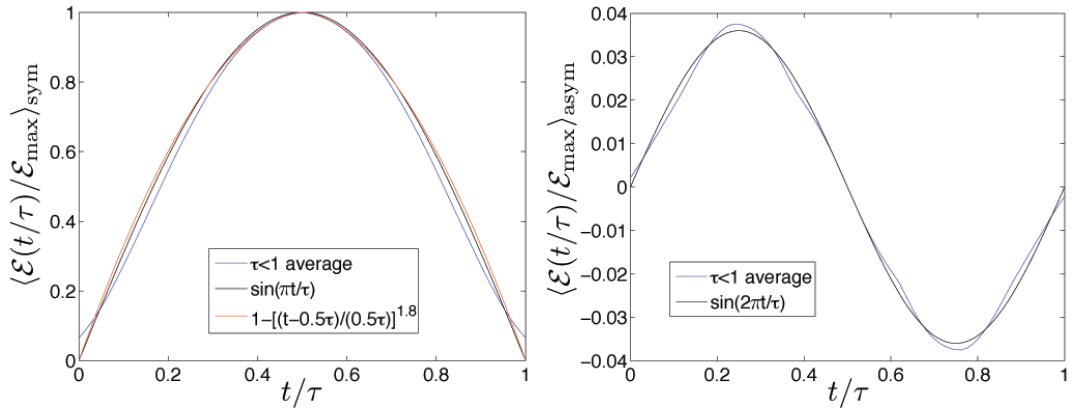

Figure 6.14: Left panel: the symmetric part of $\langle \mathcal{E}(t/\tau)/\mathcal{E}_{\text{max}} \rangle$, averaged across processes with $\tau < 1$. The fit by $\sin(\pi t/\tau)$ (shown in black) and $1-[(t-0.5\tau)/(0.5\tau)]^{1.8}$ (shown in red) both work very well. Right panel: the corresponding antisymmetric part, fit by $0.036 \sin(2\pi t/\tau)$ (shown in black).

can be seen more clearly by decomposing the curve into symmetric and anti-symmetric parts,

$$f_{\rm sym}(t) = \frac{f(t) + f(\tau - t)}{2}$$
$$f_{\rm asym}(t) = \frac{f(t) - f(\tau - t)}{2}\,, \tag{6.1}$$

where $f(t)$ is the given function on $0 < t < \tau$. Taking $f(t) = \langle \mathcal{E}(t/\tau)/\mathcal{E}_{\rm max} \rangle$, we show the symmetric and anti-symmetric parts in Fig. 6.14. As noted before, the symmetric part is well fit by $\sin(\pi t/\tau)$. We also find that it can be equally well fit by $1 - [(t - 0.5\tau)/(0.5\tau)]^{1.8}$, which is nearly indistinguishable from the sine peak. We find that the anti-symmetric part of $\langle \mathcal{E}(t/\tau)/\mathcal{E}_{\rm max} \rangle$ can be very well fit by $\sin(2\pi t/\tau)$, with an amplitude of 0.036. To investigate the asymmetry more precisely, we consider the first moments of the evolution curves,

$$\langle t/\tau \rangle_f \;=\; \frac{\int_0^\tau (t/\tau) f(t) dt}{\int_0^\tau f(t) dt}\,, \tag{6.2}$$

where deviation from 0.5 is indicative of temporal asymmetry. We show $\langle t/\tau \rangle_{\mathcal{E}}$ and $\langle t/\tau \rangle_{N_{\rm states}}$ for $\tau < 1$ in Fig. 6.15. We find that $\langle t/\tau \rangle_{\mathcal{E}}$ is very close to but slightly below 0.5, while $\langle t/\tau \rangle_{N_{\rm states}}$ is very close to but slightly above 0.5. At small τ, the displacement from 0.5 initially grows with increasing τ, but then asymptotes and becomes dominated by scatter at large τ. Upon averaging over all durations, we find that for $Re = \{800, 1250, 1800\}$, $\langle t/\tau \rangle_{\mathcal{E}} = \{0.483, 0.483, 0.476\}$ while $\langle t/\tau \rangle_{N_{\rm states}} = \{0.517, 0.517, 0.522\}$. Incidentally, the degree of asymmetry is comparable for both types of measurements, although in opposite directions.

6.7 Constraints between indices of distributions

Throughout our statistical analysis, we have considered several different measurements for the energetics: $\mathcal{E}$ (for spatial structures), $\mathcal{E}_{\rm max}$, and E. One may wonder whether these quantities are actually independent. In fact, some constraints between these

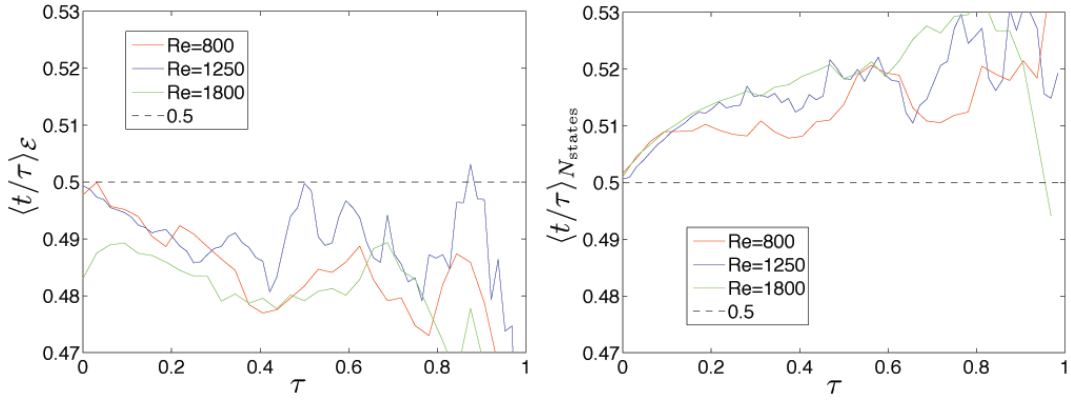

Figure 6.15: The first moment, $\langle t/\tau \rangle$, of the evolution of energy dissipation rate $\mathcal{E}(t/\tau)/\mathcal{E}_{\max}$ (left) and number of states $N_{\text{states}}(t/\tau)$ (right), versus process duration τ for $Re = 800$ (red), $Re = 1250$ (blue), and $Re = 1800$ (green). The curves are smoothed for clarity.

quantities can be made under simple assumptions. If we suppose that all processes are single paths that evolve with identical (but rescaled) functional forms for the energy dissipation rate, which is consistent with the numerical results, then we can derive several constraints between the indices of the distributions given in Sec. 6.5.

Specifically, for simplicity, assume that all processes of duration τ consist of a single path with the energy dissipation rate $\mathcal{E}_\tau(t) = \mathcal{E}_{\max}(\tau) f(t/\tau)$ for $0 < t < \tau$, where the universal shape function $f(x)$ satisfies $f(0) = f(1) = 0$, $0 \leq f(x) \leq 1$ and $\sup\{f(x)\} = 1$ for $0 < x < 1$. If we assume power-law distributions for all quantities, then they are given by

$$\begin{aligned} P(E) &\sim E^{-\alpha} \\ P(\mathcal{E}) &\sim \mathcal{E}^{-\beta} \\ P(\mathcal{E}_{\max}) &\sim \mathcal{E}_{\max}^{-\beta} \\ P(\tau) &\sim \tau^{-\gamma}\,, \end{aligned} \tag{6.3}$$

with the constraint

$$(\beta - 1)(\gamma - \alpha) = (\gamma - 1)(\alpha - 1)\,. \tag{6.4}$$

The corresponding scaling relations are given by

$$\begin{aligned} E &\sim \tau^{(\gamma-1)/(\alpha-1)} \\ \mathcal{E}_{\max} &\sim \tau^{(\gamma-\alpha)/(\alpha-1)}\,. \end{aligned} \tag{6.5}$$

Normalizable distributions require $\gamma > \alpha$. For the measured value of $\beta = 2$, $\gamma = 1/(2-\alpha)$ is required, so that $1 < \alpha < 2$. In particular, an example set of parameters satisfying this constraint are $\beta = 2$, $\gamma = 3$, and $\alpha = 5/3$, along with scalings $E \sim \tau^3$ and $\mathcal{E}_{\max} \sim \tau^2$, all of which are consistent with the numerical results.

The derivation is as follows. We first relate the distribution of instantaneous energy dissipation rates, $P(\mathcal{E})$, measured from states at random, to the distribution of peak energy dissipation rates, $P(\mathcal{E}_{\max})$, measured from processes. Assuming that one samples a random value $\mathcal{E}$ from $\mathcal{E}_\tau(t) = \mathcal{E}_{\max}(\tau) f(t/\tau)$ with uniform time sampling, so $P(t) = 1/\tau$, we obtain the distribution of energy dissipation rates from a process of duration τ,

$$P(\mathcal{E}|\tau) = \left|\frac{dt}{d\mathcal{E}}\right| P(t) = \frac{1}{\mathcal{E}_{\max}(\tau)} \sum_{i=1}^{n} \left|\frac{dx}{df(x)}\right|_{x=x_i} \equiv \frac{1}{\mathcal{E}_{\max}(\tau)} g\left(\frac{\mathcal{E}_{\max}(\tau)}{\mathcal{E}}\right)\,, \tag{6.6}$$

where x_i $(i = 1, \ldots, n)$ are the n roots of $f(x_i) - \mathcal{E}/\mathcal{E}_{\max}(\tau)$, and we have defined the function $g(y)$. The total distribution of energy dissipation rates is then

$$\begin{aligned} P(\mathcal{E}) &= \int_{\tau_{\min}}^{\infty} d\tau P(\tau) P(\mathcal{E}|\tau) \\ &= \int_{\tau_{\min}}^{\infty} d\tau P(\tau) \frac{1}{\mathcal{E}_{\max}(\tau)} g\left(\frac{\mathcal{E}_{\max}(\tau)}{\mathcal{E}}\right) \\ &= \int_{\mathcal{E}}^{\infty} d\mathcal{E}_{\max} \frac{P(\mathcal{E}_{\max})}{\mathcal{E}_{\max}} g\left(\frac{\mathcal{E}_{\max}}{\mathcal{E}}\right)\,, \end{aligned} \tag{6.7}$$

where $\tau_{\min}$ is defined such that $\mathcal{E}_{\max}(\tau_{\min}) = \mathcal{E}$. The lower bound of the integral is required since processes with durations $\tau < \tau_{\min}$ do not reach high enough energy dissipation rates to contribute to the distribution. Now assume that $P(\mathcal{E}_{\max}) \sim \mathcal{E}_{\max}^{-\beta}$. Then Eq. 6.7 becomes

$$\begin{aligned} P(\mathcal{E}) &\sim \int_{\mathcal{E}}^{\infty} d\mathcal{E}_{\max} \mathcal{E}_{\max}^{-\beta-1} g\left(\frac{\mathcal{E}_{\max}}{\mathcal{E}}\right) \\ &\sim \mathcal{E}^{-\beta} \int_{1}^{\infty} dy y^{-\beta-1} g(y) \\ &\sim \mathcal{E}^{-\beta}, \end{aligned} \tag{6.8}$$

where $y = \mathcal{E}_{\max}/\mathcal{E}$. Therefore, assuming the integral in Eq. 6.8 converges, $P(\mathcal{E})$ has the same index as $P(\mathcal{E}_{\max})$. More broadly, the same argument shows that the index of the distribution for maximum spatial scales in processes must equal the index of the distribution for instantaneous spatial scales in structures. To relate this to other indices, note that the dissipated energy $E(\tau)$ per process is given by

$$E(\tau) = \int_0^{\tau} dt \mathcal{E}_{\tau}(t) = \mathcal{E}_{\max}(\tau)\tau \int_0^1 dx f(x) \sim \mathcal{E}_{\max}(\tau)\tau\,, \tag{6.9}$$

where $x = t/\tau$, and the integral $\int_0^1 dx f(x)$ evaluates to a constant of order unity; hence, $E \sim \mathcal{E}_{\max}\tau$ is exactly satisfied. Assuming $P(\tau) \sim \tau^{-\gamma}$ and $P(E) \sim E^{-\alpha}$, we can find the exponent λ for $E \sim \tau^{\lambda}$,

$$\frac{dE}{d\tau} = \frac{P(\tau)}{P(E)} \implies \tau^{\lambda-1} = \frac{\tau^{-\gamma}}{\tau^{-\lambda\alpha}} \implies \lambda = \frac{\gamma-1}{\alpha-1}\,. \tag{6.10}$$

Hence, $\mathcal{E}_{\max} \sim E/\tau \sim \tau^{-1+(\gamma-1)/(\alpha-1)} \sim \tau^{(\gamma-\alpha)/(\alpha-1)}$ and

$$P(\mathcal{E}_{\max}) \sim \frac{d\tau}{d\mathcal{E}_{\max}} P(\tau) \sim \tau^{1-(\gamma-\alpha)/(\alpha-1)-\gamma} \sim \mathcal{E}_{\max}^{-1-(\gamma-1)(\alpha-1)/(\gamma-\alpha)}\,. \tag{6.11}$$

Therefore we have $\beta = 1 + (\gamma-1)(\alpha-1)/(\gamma-\alpha)$, as required.

6.8 Comparison to solar flare observations

In this section, we compare our statistical results for dissipative processes in MHD turbulence with the statistical properties of solar flares, taken from a number of observational studies. This comparison is not intended to draw any direct conclusions about solar flares, since our simulations are physically inadequate for describing the overall dynamics of the solar corona, although they may describe the turbulence that develops at small scales. Instead, the present comparison is motivated by the fact that solar flares are the best-observed natural example of intermittent energy dissipation in large-scale magnetized plasmas. For a more direct comparison, simulations of line-tied MHD (Galsgaard and Nordlund, 1997; Ng and Bhattacharjee, 1998; Ng et al., 2012; Wan et al., 2014) or other numerical models of the corona (Bingert and Peter, 2011, 2013) may be investigated.

The properties of solar flares are obtained from observations of extreme UV (EUV), soft X-ray, and hard X-ray emissions by applying a methodology similar to the one used here. However, there are several important, unavoidable methodological differences that may affect the comparison. First, the emission may not be in direct association with the dissipation, making it nontrivial to infer the dissipation from the spectral amplitude. Indeed, although hard X-rays are thought to be promptly powered by dissipative magnetic reconnection events, soft X-rays and EUV can originate from aftereffects including chromospheric evaporation and cooling. Second, images of solar flares are projected onto a 2D plane, reducing the available information. In addition, there are several physical differences between driven, incompressible MHD turbulence and the solar corona. In contrast to volumetrically-driven turbulence in a periodic box, flares in the solar corona are generally modeled by force-free MHD with slowly-driven, line-tied boundary conditions. Additional plasma physics arising from kinetic and two-fluid effects may be important during magnetic reconnection. Following the reconnection event, other physical processes including chromospheric evaporation, radiative cooling, and thermal conduction may affect the decay of the solar flare. Nevertheless, we proceed with the comparison.

In order to make a tangible comparison, we focus on a handful of studies which

are methodologically most similar to our present work. These are the papers by Uritsky et al. (2007) (U07), Uritsky et al. (2013) (U13), and Aschwanden et al. (2014) (A14). These studies take extreme UV images of the corona and magnetograms of the photosphere to identify 3D spatiotemporal dissipative processes. The range of indices for the distributions and scalings from these studies, along with our results, are shown in Table 6.5. The statistics for dissipated energy and length agree favorably with our results, whereas they appear to differ for durations. The sub-diffusive growth of solar flares (Aschwanden, 2012a; Aschwanden et al., 2013), which has been modeled in the framework of self-organized criticality (Aschwanden, 2012b), also appears to be at odds with the evolution of processes measured in our work.

Table 6.5: Comparison of distributions and scalings with solar flare statistics

Quantity	MHD turbulence	U07	U13	A14
Index for $P(E)$	1.75	$1.6-1.7$	1.5	$1.8-2.2$
Index for $P(\mathcal{E}_{\max})$	2.0	–	–	$2.1-2.5$
Index for $P(L)$	3.2	–	$2.5-2.9$	$3.5-4.1$
Index for $P(\tau)$	3.2	$1.9-2.1$	$2.0-2.2$	$2.2-2.6$
$\log E/\log L$	3.0	$3.0-3.6$	$3.0-3.1$	$2.5-2.6$
$\log \tau/\log L$	1.0	$1.8-2.3$	$1.2-1.4$	–

Comparing to more general studies of solar flares, our distribution for dissipated energy, with index near -1.75 ± 0.1, is close to the analogous measurements for total energy released in solar flares identified from hard X-rays, generally having an index quoted to be between -1.7 and -1.8 (e.g., Aschwanden et al., 2000; Bromund et al., 1995; Christe et al., 2008). Similarly, our distribution for peak energy dissipation rate $\mathcal{E}_{\max}$ with index -2.0 ± 0.1 is close to observations of peak hard X-ray flux (e.g., Bromund et al., 1995) and soft X-ray flux (e.g., Aschwanden and Freeland, 2012). Our distribution for duration with index near -3.2 ± 0.2 is somewhat steeper than the indices ranging between -2.2 and -3.0 for solar flare durations (Crosby et al., 1993; Bromund et al., 1995; Veronig et al., 2002), although it is closer to the index for rise times, given as -3.4 in Christe et al. (2008) and -3.2 (during solar maximum; shallower otherwise) in Aschwanden and Freeland (2012). One final point

of comparison is the asymmetry of processes, recalling that in our case, a process tends to dissipate slightly more energy at early times than late times. This is qualitatively in agreement with observations of solar and stellar flares, although the asymmetry appears to be much more pronounced in flares. The asymmetry can be defined from the rise time $t_{\rm rise}$ and decay time $t_{\rm decay}$ as $A_{\rm ev} = (t_{\rm decay} - t_{\rm rise})/(t_{\rm decay} + t_{\rm rise})$; this is found to be 0.2 for X-ray flares, giving a peak at approximately 40% of the flare duration (Christe et al., 2008). In contrast, the asymmetry of processes in our simulations, based on this definition, is 0.034.

In summary, the energetic and geometric statistical properties of dissipative events in MHD turbulence are consistent with solar flare observations, whereas the durations and temporal asymmetries present a noticeable discrepancy. The differences may be due to the Neupert effect, in which the chromospheric evaporation prolongs the decay of a flare observed in soft X-rays relative to hard X-rays (Neupert, 1968; Dennis and Zarro, 1993). This would explain why the distribution of process durations in our present work matches the distribution of solar flare rise times better than their total durations.

The nontrivial similarities in the statistical properties between dissipative events in MHD turbulence and in the solar corona leaves open the possibility that MHD turbulence plays a governing role in the intermittency of the coronal energetics. This possibility has been advocated in numerous past studies (e.g., Georgoulis, 2005; Uritsky et al., 2007, 2013) as an alternative to self-organized criticality. A more careful three-way comparison of the temporal statistics of dissipative events in MHD turbulence, self-organized criticality, and observations of the solar corona is left for future consideration.

6.9 Summary of temporal analysis

In this chapter, we demonstrated that the statistical analysis of spatiotemporal dissipative structures, i.e., time-evolving current sheets/dissipative processes/flare events, can lead to concrete physical insights about intermittency. We found the following basic conclusions to hold in numerical simulations of MHD turbulence. The

resistive energy dissipation occurs in current sheets that participate in intense, complex, long-lived processes with durations that may span several large eddy turnover times. These processes are analogous to flares in the solar corona and other astrophysical systems. The durations of these processes are directly proportional to their maximum lengths, providing a strong link between the spatial and temporal behavior. The energy dissipated in these intense processes is distributed as a power law with index near -1.75, implying the dominance of large, intense flares. Incidentally, this index is consistent with observed energy distributions of solar flares. Processes are weakly asymmetric in time, dividing more often than merging, and dissipating slightly more energy at early times in their evolution than at later times. The averaged temporal evolution for the energy dissipation rate (and geometric properties) of the processes exhibits a nearly time-symmetric, sine-like form that is applicable to processes of all durations that were robustly sampled.

7 CONCLUSION

7.1 Summary of results

In this thesis, we investigated the intermittency of energy dissipation in MHD turbulence by considering the statistical properties of dissipative current sheets in both space and time. We developed a methodology for identifying and tracking these structures, and developed methods for characterizing their spatial and temporal characteristics. We then applied these methods to a series of numerical simulations of driven MHD turbulence (in the strong guide field limit) to perform a statistical analysis on the given population of structures and the corresponding spatiotemporal processes.

A summary of the results is as follows. One must make the distinction between the statistics for structures at any given time (the spatial analysis) and for spatiotemporal structures (the temporal analysis). From the spatial analysis, we find that the energy dissipation takes place mainly in current sheets with (Euclidean) lengths L and widths W distributed in the inertial range, related by $L \sim W$. Along with energy dissipation rates $\mathcal{E}$, these have the following power-law distributions:

$$\begin{aligned} P(\mathcal{E}) &\sim \mathcal{E}^{-\beta} \\ P(L) &\sim L^{-\gamma} \\ P(W) &\sim W^{-\gamma}\,, \end{aligned} \tag{7.1}$$

where $\gamma \approx 3.3$ and $\beta \approx 2.0$. Notably, the measured scaling for $P(\mathcal{E})$ implies a critical case in which the energy dissipation rate is evenly partitioned between both weak (small) and strong (large) structures. The thicknesses T, on the other hand, are localized in the dissipation range and do not exhibit any robust scaling.

From the temporal analysis, we find that dissipative processes have maximum lengths $L_{\max}$, maximum widths $W_{\max}$, and durations τ distributed in the inertial range, related by $L_{\max} \sim W_{\max} \sim \tau$. Along with the peak energy dissipation rates

$\mathcal{E}_{\max}$ and dissipated energies E, these have power-law distributions consistent with

$$\begin{aligned} P(L_{\max}) &\sim L_{\max}^{-\gamma} \\ P(W_{\max}) &\sim W_{\max}^{-\gamma} \\ P(\tau) &\sim \tau^{-\gamma} \\ P(\mathcal{E}_{\max}) &\sim \mathcal{E}_{\max}^{-\beta} \\ P(E) &\sim E^{-\alpha}\,, \end{aligned} \tag{7.2}$$

with γ, β in agreement with the above given values, and $\alpha \approx 1.75$, implying that the strongest (largest) dissipative processes dominate the overall energy dissipation. The apparent equivalence between the distributions of the instantaneous properties of current sheets (i.e., L, W, and $\mathcal{E}$) and the maximum corresponding values for processes (i.e., $L_{\max}$, $W_{\max}$, and $\mathcal{E}_{\max}$) appears to be due to the self-similar evolution of processes (as argued in Sec. 6.7).

Other notable results are as follows. We found that the log-normal random cascade model provides a reasonable approximation for the distribution of local energy dissipation rates, and can be used to approximate the energy dissipated and volume occupied by intermittent structures. We found that two methods for measuring the characteristic scales of structures, called the Euclidean method and Minkowski method, give differing scalings and distributions for the large structures, which is attributed to the Minkowski method capturing more morphological information about the structures. We found that dissipative processes can involve many interacting current sheets, which have a small tendency to divide rather than to merge. The typical evolution of a process also shows a slight tendency for dissipating more energy at early times than at late times in the process; this evolution is otherwise well fit by a sine function.

7.2 Implications for MHD turbulence

The methodology described in this thesis is an important addition to the tools conventionally used to probing turbulence and its intermittency. It has several advantages over the other methods, despite the relatively complex numerical implementation and, for the temporal analysis, the necessity of a large data set. We find remarkably robust power-law distributions and scalings, implying that the methods are accurately extracting information about the turbulence. For example, given a relatively meager $Re = 800$, the distribution for dissipated energy per process shows a power law across nearly three decades in energy, whereas the inertial range is barely discernable in the corresponding energy spectrum at the same Re. This large separation of scales may be attributed to the cumulative information given by the combined spatial and temporal properties of the turbulence. The analysis of structures also naturally describes the anisotropy and inhomogeneity of the dynamics, which is often challenging for other methods.

In this work, we found that the distribution for the energy dissipation rates of spatial structures, as well as the distribution for the peak energy dissipation rates of spatiotemporal structures, has an index close to the critical index of -2 (Zhdankin et al., 2014). This suggests that, at any given time, inertial-range structures of all energy dissipation rates contribute equally to the overall energy dissipation rate. This may be a manifestation of the scale-invariance of inertial-range turbulence, since a distribution for energy dissipation rates with the critical index is equivalent to the energy dissipation being evenly spread across structures of all lengths, if power-law scaling is assumed (see Eq. 5.1).

Furthermore, the temporal analysis allows us to establish that the dissipated energy in evolving structures (processes) has a power law distribution with index shallower than the critical index, namely, with an index near -1.75 ± 0.1. This implies that intense dissipative events, i.e., large-scale and long-lived coherent structures, dominate the overall energy dissipation. This is a consequence of the linear scaling of duration with maximum length, which causes the distribution of dissipated energy to be shallower than the distribution of energy dissipation rates.

The distributions, scalings, and evolution of processes appear to be insensitive to the Reynolds numbers sampled in our simulations. At face value, this suggests that these statistics may be valid for the asymptotically large Re in space and astrophysical turbulence. This also implies that the results may be universal, i.e., insensitive to the mechanisms of energy input and dissipation, although this should be verified in the future by varying the boundary conditions, forcing mechanisms, and dissipation mechanisms. Examples of astrophysically-relevant driving mechanisms include the magnetorotational instability for accretion disks (Balbus and Hawley, 1991) and line-tied driving for the force-free solar corona. Indeed, line-tied boundary conditions are thought to strongly affect current sheet formation (Ng and Bhattacharjee, 1998; Cowley et al., 1997; Zweibel and Li, 1987) and magnetic tearing modes (Huang and Zweibel, 2009; Delzanno and Finn, 2008), particularly at global scales. It is also possible for the nature of intermittency to undergo a transition at sufficiently large Re, due to instabilities for large and morphologically complex structures. Therefore, it is important to verify our results in future simulations of MHD turbulence with larger Re, where more precise power-law fits can be obtained and a systematic study of the Re dependence can be investigated. It is challenging to apply our methodology for the temporal analysis, in its present form, to direct numerical simulations with larger Re, since both the spatial resolution and time cadence must be increased, making it impractical to store the full sequence of data snapshots. It may be necessary to perform the bulk of the analysis in parallel with the simulations, rather than analyzing post-processed snapshots as was done in this work. Alternatively, the amount of information used for the analysis may be reduced by, e.g., filtering out large-scale or small-scale modes. This is left for future consideration.

The methodology for the temporal analysis provides a new avenue to investigating temporal asymmetry, which was previously inferred in studies of MHD turbulence through the third-order moment or rate of energy flux (e.g., MacBride et al., 2008; Podesta, 2008; Wan et al., 2010) and field-line diffusion (Beresnyak, 2014). The temporal asymmetry in this case is measured in the larger number of divisions than mergers, the tendency of the number of states in a process to be larger at late times than early times, and the tendency of the energy dissipation rate and geometric

characteristics to be larger at early times than late times. Temporal asymmetry may occur from the onset of an instability, such as the tearing instability in resistive MHD or avalanches in critically self-organized systems. However, the asymmetry measured in our simulations is relatively negligible and does not significantly increase for larger structures that may cross an instability threshold. Furthermore, the processes do not exhibit the impulsiveness expected when an instability is triggered. Therefore, we find it unlikely that the instability of structures plays a role in our simulations, although it will be an important signature to search for in future studies. Indeed, the tearing instability is expected to occur for laminar, 2D current sheets when they become sufficiently thin, which may occur at $Rm \sim 10^4$ (e.g., Bhattacharjee et al., 2009; Uzdensky et al., 2010; Loureiro et al., 2007). It is conceivable that 3D current sheets in a turbulent medium become unstable at different (possibly lower) Rm than naively expected (Loureiro et al., 2009); it is also possible that the instability is entirely absent.

In our case, the temporal asymmetry may be linked to the turbulent energy cascade. Specifically, the inertial range of 3D MHD turbulence is characterized by a direct energy cascade from large scales to small scales. Therefore, turbulent eddies cause large structures with inertial-range lengths and widths to be broken into smaller structures, leading to a surplus of divisions over mergers, as well as more states at late times in a process. This can also explain why the energy dissipation rate and geometric characteristics are larger at early times in a process, since a single large state may accomodate a higher current density than many individual states. Since the dynamics are otherwise time-symmetric in the inertial range, this asymmetry can be relatively weak (e.g., Coburn et al., 2015). We note that another distinct contribution to the asymmetry can be from the dissipative term directly (rather than the cascade through the inertial range), relevant for states with lengths and widths that are near the dissipation scale. It is left to future work to better quantify the asymmetry and its origins, and to relate the measured quantities to the energy cascade rate.

7.3 Implications for solar flares and self-organized criticality

In our temporal analysis, we found that the energetics and length scales of dissipative processes in MHD turbulence are remarkably consistent with observations of solar flares (see Sec. 6.8). However, the statistics of durations and temporal asymmetries appear to disagree. There are three potential reasons for this observed difference between the two systems.

Firstly, the numerical results and solar flare observations may not be properly measuring the same quantity. In particular, while we directly measure the energy dissipation rate in 3D MHD turbulence, studies of solar flares must rely on inferring the energy dissipation indirectly from 2D emissions. These emissions may originate from other effects not directly related to the dissipative event. In particular, the afterglow of the flare due to chromospheric evaporation can extend the duration and amplify the asymmetry. Future observational studies may better account for this effect, as attempted by Aschwanden et al. (2014). Alternatively, a more careful comparison with observations in hard X-rays, which are more directly associated with the dissipative event, can be performed.

Secondly, the discrepancy may be caused by the RMHD simulations missing some essential physics. For example, compressibility, kinetic effects, and line-tying may be important for describing the solar corona. These factors may cause dissipative events to become more impulsive, affecting their temporal statistics (Bhattacharjee, 2004). To address this possibility, a similar statistical analysis of dissipative processes can be applied to numerical simulations which include those effects.

Thirdly, it may be possible that turbulence is not the governing physical process behind the intermittency in the solar corona. The major alternative, although not necessarily exclusive, statistical model for solar flares is self-organized criticality (Uritsky et al., 2007). It is therefore important to concoct future predictions that can definitively distinguish between turbulence and self-organized criticality. This may be nontrivial to do, since models based on self-organized criticality have a number of free parameters (e.g., the dimensionality of the dissipative event and the

diffusion exponent) (Aschwanden, 2012b; Aschwanden, 2014), and generally give similar constraints to those presented by statistical arguments in Sec. 6.7. A more careful theoretical and numerical comparison between dynamics in self-organized criticality and turbulence is left to future work.

7.4 Future directions

The success of our methodology applied to driven incompressible MHD turbulence prompts us to consider further applications to MHD and beyond. In this section, we discuss several promising future directions of this research.

Vorticity and viscous dissipation

In addition to our statistical analysis on dissipative structures in the current density, we applied our methodology to perform a cursory analysis of vorticity structures, and the associated viscous dissipation, in the same RMHD simulations. Although not presented, we found the results to be qualitatively very similar to those presented for dissipative current sheets. In particular, vorticity structures have similar energetics and a ribbon-like morphology. The main difference is that the total viscous energy dissipation is somewhat less than the resistive energy dissipation, as shown by the cumulative distributions in Sec. 4.2 and theoretical arguments in Sec. 2.3. This difference may be related to residual energy, the observed excess of magnetic energy over kinetic energy (Wang et al., 2011; Boldyrev et al., 2012b,a). In the future, the relationships and correlations between current sheets and vorticity sheets can be considered in more detail.

Clustering of structures

In addition to energy dissipation being localized in intermittent structures, the intermittent structures themselves tend to be spatially localized in clusters (e.g., Moisy and Jiménez, 2004). Numerical simulations of Navier-Stokes turbulence indicate that

intermittent structures at high Reynolds numbers organize in large-scale cloud-like structures (Ishihara et al., 2009). Therefore, the clustering characteristics of structures may be as important to consider as the structures themselves. This is especially true if the structures become unstable or lose their coherence at high Reynolds numbers. The best methodology for such an analysis is unclear and left for future consideration.

Conditional statistics

The analysis in this thesis is, by and large, limited to dissipative structures. This is done because energy dissipation, being related to the energy cascade rate, is one of the central concepts in turbulence. However, to fully understand the dynamics, one must know how the energy dissipation is connected with other quantities, including the magnetic field, velocity field, and their gradients. These quantities play a role in determining the morphology and dynamics of intermittent structures. Conditional statistics may be used to better ascertain the correlations between the various dynamical quantities.

Particle acceleration

Magnetic reconnection is believed to produce energetic particles in many space and astrophysical environments, including in solar flares (Hudson and Ryan, 1995; Aschwanden, 2002), the ambient solar wind (Fisk and Gloeckler, 2006; Tessein et al., 2013), and the Earth's magnetotail (Øieroset et al., 2002; Egedal et al., 2005). However, the mechanisms of particle acceleration remain poorly understood for realistic plasmas. It is now recognized that in order to properly describe fast magnetic reconnection in most natural systems, the effects of turbulence (Matthaeus and Lamkin, 1986; Lazarian and Vishniac, 1999; Kim and Diamond, 2001), instabilities (Loureiro et al., 2007; Uzdensky et al., 2010; Bhattacharjee et al., 2009; Huang and Bhattacharjee, 2010), or kinetic physics (Daughton and Roytershteyn, 2012) must be included. In particular, a kinetic model is essential for a consistent explanation of how the released magnetic energy is partitioned among particles.

The advent of particle-in-cell (PIC) simulations spurred progress in understanding magnetic reconnection at the kinetic level. There is now strong numerical evidence for the production of energetic particles (Drake et al., 2006, 2013; Oka et al., 2010b,a; Sironi and Spitkovsky, 2014; Guo et al., 2014). Recent studies investigated mechanisms of particle acceleration by identifying the locations and times where the energetic particles gained the most energy. These studies found that magnetic flux islands produced by the tearing instability may contribute to particle acceleration; phenomenological models based on contracting islands (Drake et al., 2006, 2013), trapped electrons (Egedal et al., 2008, 2010, 2012), coalescing islands (Oka et al., 2010b), island surfing (Hoshino, 2005; Oka et al., 2010a), and curvature drift (Hoshino et al., 2001; Guo et al., 2014) were constructed to describe the numerical observations. In general, acceleration processes evidently involve a number of diverse, competing mechanisms.

The statistical analysis of structures can give insight into the mechanisms of particle acceleration (see, e.g., Uzdensky et al., 2010; Huang and Bhattacharjee, 2012; Fermo et al., 2010; Drake et al., 2013, for some statistical models). In particular, this methodology can be applied to directly measure the contribution to particle acceleration from structures such as current sheets and magnetic flux tubes. The methodology developed in this thesis provides a foundation for such an analysis.

Other systems

The methodology developed in this thesis, and in particular, the novel methods for the temporal analysis, may prove useful for understanding intermittency in the following problems:

- Hydrodynamic turbulence
- MHD turbulence with a weak guide field
- Compressible MHD turbulence
- Magnetoconvection (Cattaneo et al., 2003)

- Kinematic dynamo (Wilkin et al., 2007)
- Magnetorotational instability (Balbus and Hawley, 1991)
- Line-tied MHD
- Turbulence in the kinetic regime (Wan et al., 2012a; Leonardis et al., 2013; Karimabadi et al., 2013; TenBarge and Howes, 2013; Pueschel et al., 2014)
- Gravitational clustering
- Self-organized criticality

It is evident that many applications of these methods exist, and that much remains to be discovered in this area of research. We look forward to exploring some of these other problems in the future.

A APPENDIX 1

The following tables show occurrence rates from the temporal analysis used to compute ratios in Subsection 6.4. Table A.1 compares all runs, Tables A.2 and A.3 show varying cadence for Cases 1 and 3, and Table A.4 shows varying threshold for Case 3.

Table A.1: Aggregate quantities in all cases ($j_{\text{thr}}/j_{\text{rms}} \approx 6.8$, $\Delta t = 1/32$)

Quantity (per τ_{eddy})	$256^3, Re = 800$	$512^3, Re = 800$	$512^3, Re = 1250$	$512^3, Re = 1800$
N_{path}	4202	5295	15392	34275
N_{proc}	914	1271	4272	11608
N_{isol}	715	956	3600	10416
N_{int}	199	315	672	1193
N_{div}	1494	1663	5352	11585
N_{mer}	1253	1290	4276	9540
N_{des}	1746	2458	7088	17312
N_{form}	1520	2096	6283	15766
$N_{\text{3-vert}}$	1449	1527	3886	7745
$N_{\text{n-vert}}$	494	539	1884	4051
$\langle N_{\text{state}} \rangle$	194	288	657	1328

Table A.2: Variation of aggregate quantities with cadence (Case 1: $256^3, Re = 800, j_{\text{thr}}/j_{\text{rms}} \approx 6.8$)

Quantity	$\Delta t = 1/64$	$\Delta t = 1/32$	$\Delta t = 1/16$	$\Delta t = 1/8$	$\Delta t = 1/4$
N_{path}	6852	4202	2426	1360	720
N_{proc}	1136	914	959	921	629
N_{isol}	894	715	834	867	613
N_{int}	241	199	126	54	16
N_{div}	2614	1494	666	199	39
N_{mer}	2277	1253	514	141	27
N_{des}	2295	1746	1418	1078	663
N_{form}	1984	1520	1276	1022	651
$N_{\text{3-vert}}$	2953	1449	512	125	24
$N_{\text{n-vert}}$	775	494	235	71	14
$\langle N_{\text{state}} \rangle$	194	194	193	192	189

Table A.3: Variation of aggregate quantities with cadence (Case 3: $512^3, Re = 1250, j_{\text{thr}}/j_{\text{rms}} \approx 6.8$)

Quantity	$\Delta t = 1/64$	$\Delta t = 1/32$	$\Delta t = 1/16$	$\Delta t = 1/8$	$\Delta t = 1/4$
N_{path}	27500	15390	8731	4748	2454
N_{proc}	3311	4272	4908	3704	2197
N_{isol}	2316	3600	4600	3595	2163
N_{int}	994	672	308	109	34
N_{div}	11900	5352	1816	495	116
N_{mer}	10060	4276	1447	382	90
N_{des}	8364	7088	5964	4031	2283
N_{form}	6954	6283	5685	3942	2264
$N_{\text{3-vert}}$	10750	3886	1099	261	57
$N_{\text{n-vert}}$	3949	1884	667	182	44

Table A.4: Variation of aggregate quantities with threshold (Case 3: $512^3, Re = 1250$)

Quantity	$j_{\text{thr}}/j_{\text{rms}} \approx 9.6$	$j_{\text{thr}}/j_{\text{rms}} \approx 8.2$	$j_{\text{thr}}/j_{\text{rms}} \approx 6.8$	$j_{\text{thr}}/j_{\text{rms}} \approx 5.5$
N_{path}	7975	14270	27500	54630
N_{proc}	1105	1777	3311	6314
N_{isol}	694	1200	2316	4565
N_{int}	341	577	994	1749
N_{div}	3077	5757	11900	26390
N_{mer}	2539	4788	10060	22785
N_{des}	2694	4705	8364	12540
N_{form}	2210	3858	6954	10900
$N_{\text{3-vert}}$	3081	5557	10750	22120
$N_{\text{n-vert}}$	964	1837	3949	8854
$\langle N_{\text{state}} \rangle$	190	343	657	1287

REFERENCES

Abdo, AA, M Ackermann, M Ajello, A Allafort, L Baldini, J Ballet, G Barbiellini, D Bastieri, K Bechtol, R Bellazzini, et al. 2011. Gamma-ray flares from the crab nebula. *Science* 331(6018):739–742.

Adams, Allan, Paul M Chesler, and Hong Liu. 2014. Holographic turbulence. *Physical Review Letters* 112(15):151602.

Albert, Jordi, E Aliu, H Anderhub, P Antoranz, A Armada, C Baixeras, JA Barrio, H Bartko, D Bastieri, JK Becker, et al. 2007. Variable very high energy γ-ray emission from markarian 501. *The Astrophysical Journal* 669(2):862.

Antar, Ghassan Y, Glenn Counsell, Yang Yu, Brian Labombard, and Pascal Devynck. 2003. Universality of intermittent convective transport in the scrape-off layer of magnetically confined devices. *Physics of Plasmas (1994-present)* 10(2):419–428.

Armstrong, JW, BJ Rickett, and SR Spangler. 1995. Electron density power spectrum in the local interstellar medium. *The Astrophysical Journal* 443:209–221.

Arneodo, A, S Manneville, and JF Muzy. 1998. Towards log-normal statistics in high reynolds number turbulence. *The European Physical Journal B-Condensed Matter and Complex Systems* 1(1):129–140.

Arneodo, A, S Manneville, JF Muzy, and SG Roux. 1999. Revealing a lognormal cascading process in turbulent velocity statistics with wavelet analysis. *Philosophical Transactions of the Royal Society of London. Series A: Mathematical, Physical and Engineering Sciences* 357(1760):2415–2438.

Aschwanden, M. J. 2014. A Macroscopic Description of a Generalized Self-organized Criticality System: Astrophysical Applications. *The Astrophysical Journal* 782:54.

Aschwanden, Markus J. 2002. Particle acceleration and kinematics in solar flares–a synthesis of recent observations and theoretical concepts (invited review). *Space Science Reviews* 101(1-2):1–227.

———. 2012a. The spatio-temporal evolution of solar flares observed with aia/sdo: Fractal diffusion, sub-diffusion, or logistic growth? *The Astrophysical Journal* 757(1): 94.

———. 2012b. A statistical fractal-diffusive avalanche model of a slowly-driven self-organized criticality system. *Astronomy and Astrophysics* 539:A2.

Aschwanden, Markus J, and Samuel L Freeland. 2012. Automated solar flare statistics in soft x-rays over 37 years of goes observations: the invariance of self-organized criticality during three solar cycles. *The Astrophysical Journal* 754(2):112.

Aschwanden, Markus J, Ted D Tarball, Richard W Nightingale, Carolus J Schrijver, Charles C Kankelborg, Piet Martens, Harry P Warren, et al. 2000. Time variability of the quietïi sun observed with t race. ii. physical parameters, temperature evolution, and energetics of extreme-ultraviolet nanoflares. *The Astrophysical Journal* 535: 1047È1065.

Aschwanden, Markus J, Yan Xu, and Ju Jing. 2014. Global energetics of solar flares. i. magnetic energies. *The Astrophysical Journal* 797(1):50.

Aschwanden, Markus J, Jie Zhang, and Kai Liu. 2013. Multi-wavelength observations of the spatio-temporal evolution of solar flares with aia/sdo. i. universal scaling laws of space and time parameters. *The Astrophysical Journal* 775(1):23.

Asgari-Targhi, Mahboubeh, AA Van Ballegooijen, SR Cranmer, and EE DeLuca. 2013. The spatial and temporal dependence of coronal heating by alfvén wave turbulence. *The Astrophysical Journal* 773(2):111.

Audard, Marc, Manuel Güdel, and Edward F Guinan. 1999. Implications from extreme-ultraviolet observations for coronal heating of active stars. *The Astrophysical Journal Letters* 513(1):L53.

Baalrud, S.D., A. Bhattacharjee, and Y.M. Huang. 2012. Reduced magnetohydrodynamic theory of oblique plasmoid instabilities. *Physics of Plasmas* 19(2): 022101.

Balbus, Steven A, and John F Hawley. 1991. A powerful local shear instability in weakly magnetized disks. i-linear analysis. ii-nonlinear evolution. *The Astrophysical Journal* 376:214–233.

Benz, AO, and M Güdel. 1994. X-ray/microwave ratio of flares and coronae. *Astronomy and Astrophysics* 285:621–630.

Benzi, R, S Ciliberto, R Tripiccione, C Baudet, F Massaioli, and S Succi. 1993. Extended self-similarity in turbulent flows. *Physical review E* 48(1):R29.

Beresnyak, Andrey. 2011. Spectral slope and kolmogorov constant of mhd turbulence. *Physical Review Letters* 106(7):075001.

———. 2014. Asymmetric diffusion of magnetic field lines in turbulence. *Physica Scripta* 89(11):118001.

Bershadskii, A. 2003. Three-dimensional isotropic magnetohydrodynamic turbulence and thermal velocity of the solar wind ions. *Physics of Plasmas (1994-present)* 10(12):4613–4615.

Bhattacharjee, A., Y.-M. Huang, H. Yang, and B. Rogers. 2009. Fast reconnection in high-Lundquist-number plasmas due to the plasmoid Instability. *Physics of Plasmas* 16(11):112102.

Bhattacharjee, Amitava. 2004. Impulsive magnetic reconnection in the earth's magnetotail and the solar corona. *Annu. Rev. Astron. Astrophys.* 42:365–384.

Bingert, Sven, and Hardi Peter. 2011. Intermittent heating in the solar corona employing a 3d mhd model. *Astronomy and Astrophysics* 530:A112.

———. 2013. Nanoflare statistics in an active region 3d mhd coronal model. *Astronomy and Astrophysics* 550:A30.

Biskamp, D. 2003. *Magnetohydrodynamic turbulence*. Cambridge Univ Pr.

Biskamp, Dieter. 1995. Scaling properties in mhd turbulence. *Chaos, Solitons & Fractals* 5(10):1779–1793.

Blaes, O. 2013. General Overview of Black Hole Accretion Theory. *Space Science Reviews*.

Boffetta, Guido, Vincenzo Carbone, Paolo Giuliani, Pierluigi Veltri, and Angelo Vulpiani. 1999. Power laws in solar flares: self-organized criticality or turbulence? *Physical Review Letters* 83(22):4662.

Boldyrev, S. 2005. On the spectrum of magnetohydrodynamic turbulence. *The Astrophysical Journal Letters* 626(1):L37.

———. 2006. Spectrum of magnetohydrodynamic turbulence. *Physical Review Letters* 96(11):115002.

Boldyrev, S., A. A.. Nordlund, and P. Padoan. 2002. Scaling Relations of Supersonic Turbulence in Star-forming Molecular Clouds. *The Astrophysical Journal* 573: 678–684.

Boldyrev, S., J. C. Perez, and Y. Wang. 2012a. Residual Energy in Weak and Strong MHD Turbulence. In *Numerical modeling of space plasma slows (astronum 2011)*, ed. N. V. Pogorelov, J. A. Font, E. Audit, and G. P. Zank, vol. 459 of *Astronomical Society of the Pacific Conference Series*, 3.

Boldyrev, S., J. C. Perez, and V. Zhdankin. 2012b. Residual energy in MHD turbulence and in the solar wind. In *American institute of physics conference series*, ed. J. Heerikhuisen, G. Li, N. Pogorelov, and G. Zank, vol. 1436 of *American Institute of Physics Conference Series*, 18–23.

Brandenburg, Axel, Kari Enqvist, and Poul Olesen. 1996. Large-scale magnetic fields from hydromagnetic turbulence in the very early universe. *Physical Review D* 54(2):1291.

Bromund, Kenneth R, James M McTiernan, and Sharad R Kane. 1995. Statistical studies of isee 3/ice observations of impulsive hard x-ray solar flares. *The Astrophysical Journal* 455:733.

Bruno, R, V Carbone, L Primavera, F Malara, L Sorriso-Valvo, B Bavassano, and P Veltri. 2004. On the probability distribution function of small-scale interplanetary magnetic field fluctuations. *Annales Geophysicae* 22(10):3751–3769.

Buchlin, E, and M Velli. 2007. Shell models of rmhd turbulence and the heating of solar coronal loops. *The Astrophysical Journal* 662(1):701.

Burlaga, LF. 2001. Lognormal and multifractal distributions of the heliospheric magnetic field. *Journal of Geophysical Research: Space Physics (1978–2012)* 106(A8): 15917–15927.

Bushby, PJ, and S. M. Houghton. 2005. Spatially intermittent fields in photospheric magnetoconvection. *Monthly Notices of the Royal Astronomical Society* 362(1): 313–320.

Carbone, V, L Sorriso-Valvo, E Martines, V Antoni, and P Veltri. 2000. Intermittency and turbulence in a magnetically confined fusion plasma. *Physical Review E* 62(1): R49.

Carnevale, GF, JC McWilliams, Y Pomeau, JB Weiss, and WR Young. 1991. Evolution of vortex statistics in two-dimensional turbulence. *Physical Review Letters* 66(21):2735.

Cattaneo, Fausto. 1999. On the origin of magnetic fields in the quiet photosphere. *The Astrophysical Journal Letters* 515(1):L39.

Cattaneo, Fausto, Thierry Emonet, and Nigel Weiss. 2003. On the interaction between convection and magnetic fields. *The Astrophysical Journal* 588(2):1183.

Chen, C. H. K., T. S. Horbury, A. A. Schekochihin, R. T. Wicks, O Alexandrova, and J Mitchell. 2010. Anisotropy of solar wind turbulence between ion and electron scales. *Physical Review Letters* 104(25):255002.

Chen, CHK, A Mallet, TA Yousef, AA Schekochihin, and TS Horbury. 2011. Anisotropy of alfvénic turbulence in the solar wind and numerical simulations. *Monthly Notices of the Royal Astronomical Society* 415(4):3219–3226.

Cho, Jungyeon, Alex Lazarian, and Ethan T Vishniac. 2002. Simulations of magnetohydrodynamic turbulence in a strongly magnetized medium. *The Astrophysical Journal* 564(1):291.

Christe, S, IG Hannah, Säm Krucker, J McTiernan, and Robert P Lin. 2008. Rhessi microflare statistics. i. flare-finding and frequency distributions. *The Astrophysical Journal* 677(2):1385.

Coburn, Jesse T, Miriam A Forman, Charles W Smith, Bernard J Vasquez, and Julia E Stawarz. 2015. Third-moment descriptions of the interplanetary turbulent cascade, intermittency and back transfer. *Philosophical Transactions of the Royal Society of London A: Mathematical, Physical and Engineering Sciences* 373(2041): 20140150.

Collura, A, L Pasquini, and JHMM Schmitt. 1988. Time variability in the x-ray emission of dm stars observed by exosat. *Astronomy and Astrophysics* 205:197–206.

Cowley, SC, DW Longcope, and RN Sudan. 1997. Current sheets in mhd turbulence. *Physics Reports* 283(1):227–251.

Cranmer, Steven R, Mahboubeh Asgari-Targhi, Mari Paz Miralles, John C Raymond, Leonard Strachan, Hui Tian, and Lauren N Woolsey. 2015. The role of turbulence in coronal heating and solar wind expansion. *Philosophical Transactions of the Royal Society of London A: Mathematical, Physical and Engineering Sciences* 373(2041): 20140148.

Cranmer, Steven R, Adriaan A Van Ballegooijen, and Richard J Edgar. 2007. Self-consistent coronal heating and solar wind acceleration from anisotropic magnetohydrodynamic turbulence. *The Astrophysical Journal Supplement Series* 171(2): 520.

Crosby, Norma B, Markus J Aschwanden, and Brian R Dennis. 1993. Frequency distributions and correlations of solar x-ray flare parameters. *Solar Physics* 143(2): 275–299.

Dahlburg, R. B., G. Einaudi, A. F. Rappazzo, and M. Velli. 2012. Turbulent coronal heating mechanisms: coupling of dynamics and thermodynamics. *Astron. Astrophys.* 544:L20.

Daughton, William, and Vadim Roytershteyn. 2012. Emerging parameter space map of magnetic reconnection in collisional and kinetic regimes. *Space science reviews* 172(1-4):271–282.

De Wit, T.D. 2004. Can high-order moments be meaningfully estimated from experimental turbulence measurements? *Physical Review E* 70(5):055302.

Delzanno, Gian Luca, and John M Finn. 2008. The effect of line-tying on tearing modes. *Physics of Plasmas* 15:032904.

Dennis, Brian R, and Dominic M Zarro. 1993. The neupert effect: What can it tell us about the impulsive and gradual phases of solar flares? *Solar Physics* 146(1): 177–190.

Di Matteo, Tiziana, Annalisa Celotti, and Andrew C Fabian. 1999. Magnetic flares in accretion disc coronae and the spectral states of black hole candidates: The case of gx339-4. *Monthly Notices of the Royal Astronomical Society* 304(4):809–820.

D'Ippolito, DA, JR Myra, SI Krasheninnikov, GQ Yu, and A Yu Pigarov. 2004. Blob transport in the tokamak scrape-off-layer. *Contributions to Plasma Physics* 44(1-3):205–216.

Dmitruk, Pablo, and Daniel O Gómez. 1997. Turbulent coronal heating and the distribution of nanoflares. *The Astrophysical Journal Letters* 484(1):L83.

———. 1999. Scaling law for the heating of solar coronal loops. *The Astrophysical Journal Letters* 527(1):L63.

Douady, S, Y Couder, and ME Brachet. 1991. Direct observation of the intermittency of intense vorticity filaments in turbulence. *Physical Review Letters* 67(8):983.

Drake, JF, Merav Opher, Marc Swisdak, and JN Chamoun. 2010. A magnetic reconnection mechanism for the generation of anomalous cosmic rays. *The Astrophysical Journal* 709(2):963.

Drake, JF, M Swisdak, H Che, and MA Shay. 2006. Electron acceleration from contracting magnetic islands during reconnection. *Nature* 443(7111):553–556.

Drake, JF, M Swisdak, and R Fermo. 2013. The power-law spectra of energetic particles during multi-island magnetic reconnection. *The Astrophysical Journal Letters* 763(1):L5.

Dubrulle, Bérengère. 1994. Intermittency in fully developed turbulence: Log-poisson statistics and generalized scale covariance. *Physical Review Letters* 73(7):959.

Eckart, A, FK Baganoff, MR Morris, D Kunneriath, M Zamaninasab, G Witzel, R Schödel, M García-Marín, L Meyer, GC Bower, et al. 2009. Modeling mm-to x-ray flare emission from sagittarius a*. *Astronomy and Astrophysics* 500:935–946.

Egedal, J, W Fox, N Katz, M Porkolab, M Øieroset, RP Lin, W Daughton, and JF Drake. 2008. Evidence and theory for trapped electrons in guide field magnetotail reconnection. *Journal of Geophysical Research: Space Physics (1978–2012)* 113(A12).

Egedal, J, A Lê, Y Zhu, W Daughton, M Øieroset, T Phan, RP Lin, and JP Eastwood. 2010. Cause of super-thermal electron heating during magnetotail reconnection. *Geophysical Research Letters* 37(10).

Egedal, J, M Øieroset, W Fox, and RP Lin. 2005. In situ discovery of an electrostatic potential, trapping electrons and mediating fast reconnection in the earth's magnetotail. *Physical Review Letters* 94(2):025006.

Egedal, Jan, W Daughton, and A Le. 2012. Large-scale electron acceleration by parallel electric fields during magnetic reconnection. *Nature Physics* 8(4):321–324.

Einaudi, G, and M Velli. 1999. The distribution of flares, statistics of magnetohydrodynamic turbulence and coronal heating. *Physics of Plasmas* 6:4146.

Falgarone, Edith, Giorgos Momferratos, and Pierre Lesaffre. 2015. The intermittency of ism turbulence: What do the observations tell us? In *Magnetic fields in diffuse media*, 227–252. Springer.

Fefferman, Charles L. 2000. Existence and smoothness of the navier-stokes equation. *The millennium prize problems* 57–67.

Fermo, RL, JF Drake, and M Swisdak. 2010. A statistical model of magnetic islands in a current layer. *Physics of Plasmas (1994-present)* 17(1):010702.

Feynman, Richard Phillips. 1948. Space-time approach to non-relativistic quantum mechanics. *Reviews of Modern Physics* 20(2):367.

Fisk, LA, and G Gloeckler. 2006. The common spectrum for accelerated ions in the quiet-time solar wind. *The Astrophysical Journal Letters* 640(1):L79.

Frisch, U. 1995. *Turbulence: The legacy of an kolmogorov*. Cambridge Univ. Press.

Galsgaard, Klaus, and Åke Nordlund. 1997. Heating and activity of the solar corona: 3. dynamics of a low beta plasma with three-dimensional null points. *Journal of Geophysical Research: Space Physics (1978–2012)* 102(A1):231–248.

Galtier, S, SV Nazarenko, Alan C Newell, and A Pouquet. 2000. A weak turbulence theory for incompressible magnetohydrodynamics. *Journal of Plasma Physics* 63(05): 447–488.

Georgoulis, Manolis K. 2005. Turbulence in the solar atmosphere: manifestations and diagnostics via solar image processing. *Solar Physics* 228(1-2):5–27.

Georgoulis, Manolis K, Marco Velli, and Giorgio Einaudi. 1998. Statistical properties of magnetic activity in the solar corona. *The Astrophysical Journal* 497(2):957.

Goldreich, P., and S. Sridhar. 1995. Toward a theory of interstellar turbulence. 2: Strong alfvenic turbulence. *The Astrophysical Journal* 438:763–775.

Goodman, J., and D. A. Uzdensky. 2008. Reconnection in marginally collisionless accretion disk coronae. *The Astrophysical Journal* 688(1):555.

Gosling, JT. 2007. Observations of magnetic reconnection in the turbulent high-speed solar wind. *The Astrophysical Journal Letters* 671(1):L73.

Grauer, R, J Krug, and C Marliani. 1994. Scaling of high-order structure functions in magnetohydrodynamic turbulence. *Physics Letters A* 195(5):335–338.

Greco, A., W.H. Matthaeus, S. Servidio, P. Chuychai, and P. Dmitruk. 2009a. Statistical analysis of discontinuities in solar wind ace data and comparison with intermittent mhd turbulence. *The Astrophysical Journal Letters* 691:L111.

Greco, A, WH Matthaeus, S Servidio, and P Dmitruk. 2009b. Waiting-time distributions of magnetic discontinuities: Clustering or poisson process? *Physical Review E* 80(4):046401.

Green, Stephen R, Federico Carrasco, and Luis Lehner. 2014. Holographic path to the turbulent side of gravity. *Physical Review X* 4(1):011001.

Güdel, Manuel, Marc Audard, Vinay L Kashyap, Jeremy J Drake, and Edward F Guinan. 2003. Are coronae of magnetically active stars heated by flares? ii. extreme ultraviolet and x-ray flare statistics and the differential emission measure distribution. *The Astrophysical Journal* 582(1):423.

Guo, Fan, Hui Li, William Daughton, and Yi-Hsin Liu. 2014. Formation of hard power laws in the energetic particle spectra resulting from relativistic magnetic reconnection. *Physical Review Letters* 113:155005.

Gurnett, Donald A, and Amitava Bhattacharjee. 2005. *Introduction to plasma physics: with space and laboratory applications*. Cambridge university press.

Hannah, IG, S Christe, Säm Krucker, GJ Hurford, HS Hudson, and Robert P Lin. 2008. Rhessi microflare statistics. ii. x-ray imaging, spectroscopy, and energy distributions. *The Astrophysical Journal* 677(1):704.

Haynes, AL, and CE Parnell. 2010. A method for finding three-dimensional magnetic skeletons. *Physics of Plasmas* 17:092903.

Heyvaerts, J, and ER Priest. 1992. A self-consistent turbulent model for solar coronal heating. *The Astrophysical Journal* 390:297–308.

Horbury, T. S., and A Balogh. 1997. Structure function measurements of the intermittent mhd turbulent cascade. *Nonlinear Processes in Geophysics* 4(3):185–199.

Hoshino, M, T Mukai, T Terasawa, and I Shinohara. 2001. Suprathermal electron acceleration in magnetic reconnection. *Journal of Geophysical Research: Space Physics (1978–2012)* 106(A11):25979–25997.

Hoshino, Masahiro. 2005. Electron surfing acceleration in magnetic reconnection. *Journal of Geophysical Research: Space Physics (1978–2012)* 110(A10).

Hosokawa, I, and K Yamamoto. 1992. Evidence against the kolmogorov refined similarity hypothesis. *Physics of Fluids A: Fluid Dynamics (1989-1993)* 4(3):457–459.

Huang, Yi-Min, and A Bhattacharjee. 2012. Distribution of plasmoids in high-lundquist-number magnetic reconnection. *Physical Review Letters* 109(26):265002.

Huang, Yi-Min, and Ellen G Zweibel. 2009. Effects of line tying on resistive tearing instability in slab geometry. *Physics of Plasmas* 16:042102.

Huang, Y.M., and A. Bhattacharjee. 2010. Scaling laws of resistive magnetohydrodynamic reconnection in the high-lundquist-number, plasmoid-unstable regime. *Physics of Plasmas* 17(6).

Hudson, H, and J Ryan. 1995. High-energy particles in solar flares. *Annual Review of Astronomy and Astrophysics* 33(1):239–282.

Hudson, HS. 1991. Solar flares, microflares, nanoflares, and coronal heating. *Solar Physics* 133(2):357–369.

Ishihara, Takashi, Toshiyuki Gotoh, and Yukio Kaneda. 2009. Study of high-reynolds number isotropic turbulence by direct numerical simulation. *Annual Review of Fluid Mechanics* 41:165–180.

Jimenez, Javier, and Alan A Wray. 1998. On the characteristics of vortex filaments in isotropic turbulence. *Journal of Fluid Mechanics* 373:255–285.

Jiménez, Javier, Alan A Wray, Philip G Saffman, and Robert S Rogallo. 1993. The structure of intense vorticity in isotropic turbulence. *Journal of Fluid Mechanics* 255:65–90.

Kadomtsev, B.B., and V.M. Kantorovich. 1974. Turbulence theory in hydrodynamics and in a plasma. *Nauchnaia Shkola po Nelineinym Kolebaniiam i Volnam v Raspredelennykh Sistemakh, 2 nd, Gorki, USSR, Mar. 1973.) Radiofizika* 17(4): 511–540.

Karimabadi, H, V Roytershteyn, M Wan, WH Matthaeus, W Daughton, P Wu, M Shay, B Loring, J Borovsky, Ersilia Leonardis, et al. 2013. Coherent structures, intermittent turbulence, and dissipation in high-temperature plasmas. *Physics of Plasmas* 20(1):012303.

Kerscher, Martin. 2000. Statistical analysis of large-scale structure in the universe. In *Statistical physics and spatial statistics*, 36–71. Springer.

Kida, Shigeo, and Hideaki Miura. 1998. Identification and analysis of vortical structures. *European Journal of Mechanics-B/Fluids* 17(4):471–488.

Kim, E., and PH Diamond. 2001. On turbulent reconnection. *The Astrophysical Journal* 556:1052.

Klimchuk, James A. 2006. On solving the coronal heating problem. *Solar Physics* 234(1):41–77.

Knizhnik, Kalman, Marc Swisdak, and James F Drake. 2011. The acceleration of ions in solar flares during magnetic reconnection. *The Astrophysical Journal Letters* 743(2):L35.

Kolář, Václav. 2007. Vortex identification: New requirements and limitations. *International journal of heat and fluid flow* 28(4):638–652.

Kolmogorov, Andrey Nikolaevich. 1941. Dissipation of energy in locally isotropic turbulence. *Dokl. Akad. Nauk SSSR* 32(1):16–18.

———. 1962. A refinement of previous hypotheses concerning the local structure of turbulence in a viscous incompressible fluid at high reynolds number. *Journal of Fluid Mechanics* 13(01):82–85.

Kowal, G., A. Lazarian, E.T. Vishniac, and K. Otmianowska-Mazur. 2009. Numerical tests of fast reconnection in weakly stochastic magnetic fields. *The Astrophysical Journal* 700:63.

Kraichnan, Robert H. 1974. On kolmogorov's inertial-range theories. *Journal of Fluid Mechanics* 62(02):305–330.

Kritsuk, A. G., M. L. Norman, and R. Wagner. 2011. On the Density Distribution in Star-forming Interstellar Clouds. *The Astrophysical Journal Letters* 727:L20.

Lazarian, A., and E.T. Vishniac. 1999. Reconnection in a weakly stochastic field. *The Astrophysical Journal* 517:700.

Leonardis, Ersilia, SC Chapman, W Daughton, V Roytershteyn, and H Karimabadi. 2013. Identification of intermittent multifractal turbulence in fully kinetic simulations of magnetic reconnection. *Physical Review Letters* 110(20):205002.

Leung, T, N Swaminathan, and PA Davidson. 2012. Geometry and interaction of structures in homogeneous isotropic turbulence. *Journal of Fluid Mechanics* 710: 453.

Liu, Jiajia, Scott W McIntosh, Ineke De Moortel, James Threlfall, and Christian Bethge. 2014. Statistical evidence for the existence of alfvénic turbulence in solar coronal loops. *The Astrophysical Journal* 797(1):7.

Longcope, D.W., and R.N. Sudan. 1994. Evolution and statistics of current sheets in coronal magnetic loops. *The Astrophysical Journal* 437:491–504.

Loureiro, N. F., A. A. Schekochihin, and D. A. Uzdensky. 2013. Plasmoid and Kelvin-Helmholtz instabilities in Sweet-Parker current sheets. *Phys. Rev. E* 87(1): 013102. 1208.0966.

Loureiro, N. F., D. A. Uzdensky, A. A. Schekochihin, S. C. Cowley, and T. A. Yousef. 2009. Turbulent magnetic reconnection in two dimensions. *Monthly Notices of the Royal Astronomical Society: Letters* 399(1):L146–L150.

Loureiro, NF, AA Schekochihin, and SC Cowley. 2007. Instability of current sheets and formation of plasmoid chains. *Physics of Plasmas* 14:100703.

MacBride, Benjamin T, Charles W Smith, and Miriam A Forman. 2008. The turbulent cascade at 1 au: Energy transfer and the third-order scaling for mhd. *The Astrophysical Journal* 679(2):1644.

Makwana, K. D., V. Zhdankin, H. Li, W. Daughton, and F. Cattaneo. 2015. Energy dynamics and current sheet structure in fluid and kinetic simulations of decaying magnetohydrodynamic turbulence. *Physics of Plasmas* 22(4):042902.

Mallet, A, AA Schekochihin, and BDG Chandran. 2015. Refined critical balance in strong alfvénic turbulence. *Monthly Notices of the Royal Astronomical Society: Letters* 449(1):L77–L81.

Mandelbrot, Benoit B. 1974. Intermittent turbulence in self-similar cascades: divergence of high moments and dimension of the carrier. *Journal of Fluid Mechanics* 62(02):331–358.

Maron, Jason, and Peter Goldreich. 2001. Simulations of incompressible magnetohydrodynamic turbulence. *The Astrophysical Journal* 554(2):1175.

Mason, J., F. Cattaneo, and S. Boldyrev. 2008. Numerical measurements of the spectrum in magnetohydrodynamic turbulence. *Physical Review E* 77(3):036403–+.

Matthaeus, W.H., and S.L. Lamkin. 1986. Turbulent magnetic reconnection. *Physics of Fluids* 29:2513.

Matthaeus, William H. 1982. Reconnection in two dimensions- localization of vorticity and current near magnetic x-points. *Geophysical Research Letters* 9(6): 660–663.

McWilliams, James C. 1990. The vortices of two-dimensional turbulence. *Journal of Fluid Mechanics* 219(361-385):102.

McWilliams, J.C., J.B. Weiss, and I. Yavneh. 1999. The vortices of homogeneous geostrophic turbulence. *Journal of Fluid Mechanics* 401(1):1–26.

Mecke, Klaus R. 2000. Additivity, convexity, and beyond: applications of minkowski functionals in statistical physics. In *Statistical physics and spatial statistics*, 111–184. Springer.

Merrifield, J. A., W-C Müller, S. C. Chapman, and R. O. Dendy. 2005. The scaling properties of dissipation in incompressible isotropic three-dimensional magnetohydrodynamic turbulence. *Physics of Plasmas* 12(2):022301.

Moisy, Frédéric, and Javier Jiménez. 2004. Geometry and clustering of intense structures in isotropic turbulence. *Journal of Fluid Mechanics* 513:111–133.

Molchan, GM. 1997. Turbulent cascades: Limitations and a statistical test of the lognormal hypothesis. *Physics of Fluids (1994-present)* 9(8):2387–2396.

Momferratos, G, P Lesaffre, E Falgarone, and G Pineau des Forêts. 2014. Turbulent energy dissipation and intermittency in ambipolar diffusion magnetohydrodynamics. *Monthly Notices of the Royal Astronomical Society* 443(1):86–101.

Mouri, Hideaki, Akihiro Hori, and Masanori Takaoka. 2009. Large-scale lognormal fluctuations in turbulence velocity fields. *Physics of Fluids (1994-present)* 21(6): 065107.

Müller, Wolf-Christian, and Dieter Biskamp. 2000. Scaling properties of three-dimensional magnetohydrodynamic turbulence. *Physical Review Letters* 84(3):475.

Müller, Wolf-Christian, Dieter Biskamp, and Roland Grappin. 2003. Statistical anisotropy of magnetohydrodynamic turbulence. *Physical Review E* 67(6):066302.

Naert, Antoon, B Castaing, B Chabaud, B Hebral, and J Peinke. 1998. Conditional statistics of velocity fluctuations in turbulence. *Physica D: Nonlinear Phenomena* 113(1):73–78.

Nelkin, Mark. 1995. Inertial range scaling of intense events in turbulence. *Physical Review E* 52(5):R4610.

Neupert, Werner M. 1968. Comparison of solar x-ray line emission with microwave emission during flares. *The Astrophysical Journal* 153:L59.

Ng, CS, and A Bhattacharjee. 1998. Nonequilibrium and current sheet formation in line-tied magnetic fields. *Physics of Plasmas* 5:4028.

Ng, CS, and L Lin. 2012. Energy distribution of nanoflares in three-dimensional simulations of coronal heating. In *American institute of physics conference series*, vol. 1500, 38–43.

Ng, CS, L Lin, and A Bhattacharjee. 2012. High-lundquist number scaling in three-dimensional simulations of parker's model of coronal heating. *The Astrophysical Journal* 747(2):109.

Nigro, Giuseppina, Francesco Malara, Vincenzo Carbone, and Pierluigi Veltri. 2004. Nanoflares and mhd turbulence in coronal loops: a hybrid shell model. *Physical Review Letters* 92(19):194501.

Novikov, EA. 1971. Intermittency and scale similarity in the structure of a turbulent plow: Pmm vol. 35, n? 2, 1971, pp. 266–277. *Journal of Applied Mathematics and Mechanics* 35(2):231–241.

Obukhov, AM. 1962. Some specific features of atmospheric turbulence. *J. Fluid Mech* 13(1):77–81.

Øieroset, M, RP Lin, TD Phan, DE Larson, and SD Bale. 2002. Evidence for electron acceleration up to 300 k e v in the magnetic reconnection diffusion region of earths magnetotail. *Physical Review Letters* 89(19):195001.

Oka, M, M Fujimoto, I Shinohara, and TD Phan. 2010a. island surfing mechanism of electron acceleration during magnetic reconnection. *Journal of Geophysical Research: Space Physics (1978–2012)* 115(A8).

Oka, M, T-D Phan, S Krucker, M Fujimoto, and I Shinohara. 2010b. Electron acceleration by multi-island coalescence. *The Astrophysical Journal* 714(1):915.

Opher, M, JF Drake, M Swisdak, KM Schoeffler, JD Richardson, RB Decker, and G Toth. 2011. Is the magnetic field in the heliosheath laminar or a turbulent sea of bubbles? *The Astrophysical Journal* 734(1):71.

Osman, KT, WH Matthaeus, A Greco, and S Servidio. 2011. Evidence for inhomogeneous heating in the solar wind. *The Astrophysical Journal Letters* 727(1): L11.

Pallavicini, R, G Tagliaferri, and L Stella. 1990. X-ray emission from solar neighbourhood flare stars-a comprehensive survey of exosat results. *Astronomy and Astrophysics* 228:403–425.

Pan, Liubin, Paolo Padoan, and Alexei G Kritsuk. 2009. Dissipative structures in supersonic turbulence. *Physical Review Letters* 102(3):034501.

Paoletti, Matthew S, and Daniel P Lathrop. 2011. Quantum turbulence. *Annu. Rev. Condens. Matter Phys.* 2(1):213–234.

Pariev, V. I., E. G. Blackman, and S. A. Boldyrev. 2003. Extending the Shakura-Sunyaev approach to a strongly magnetized accretion disc model. *Astron. Astrophys.* 407:403–421.

Parker, E. N. 1972. Topological Dissipation and the Small-Scale Fields in Turbulent Gases. *Astrophys. J.* 174:499.

———. 1983. Magnetic neutral sheets in evolving fields. i-general theory. *The Astrophysical Journal* 264:635–647.

———. 1988. Nanoflares and the solar x-ray corona. *The Astrophysical Journal* 330: 474–479.

Parker, E.N. 1957. Sweet's mechanism for merging magnetic fields in conducting fluids. *Journal of Geophysical Research* 62(4):509–520.

Parnell, CE, and PE Jupp. 2000. Statistical analysis of the energy distribution of nanoflares in the quiet sun. *The Astrophysical Journal* 529(1):554.

Parnell, C.E., R.C. Maclean, A.L. Haynes, and K. Galsgaard. 2010. 3d magnetic reconnection. *Proceedings of the International Astronomical Union* 6(S271):227–238.

Parnell, Clare E, and Ineke De Moortel. 2012. A contemporary view of coronal heating. *Philosophical Transactions of the Royal Society of London A: Mathematical, Physical and Engineering Sciences* 370(1970):3217–3240.

Pasquero, Claudia, Antonello Provenzale, and Jeffrey B Weiss. 2002. Vortex statistics from eulerian and lagrangian time series. *Physical Review Letters* 89(28):284501.

Perez, J. C., and S. Boldyrev. 2010. Numerical Simulations of Imbalanced Strong Magnetohydrodynamic Turbulence. *The Astrophysical Journal Letters* 710:L63–L66.

Perez, J.C., J. Mason, F. Cattaneo, and S. Boldyrev. 2012. On the energy spectrum of strong magnetohydrodynamic turbulence. *Physical Review X* 2:041005.

Petschek, H. E. 1964. Magnetic Field Annihilation. *NASA Special Publication* 50: 425.

Phan, TD, JT Gosling, G Paschmann, C Pasma, JF Drake, M Øieroset, D Larson, RP Lin, and MS Davis. 2010. The dependence of magnetic reconnection on plasma

β and magnetic shear: Evidence from solar wind observations. *The Astrophysical Journal Letters* 719(2):L199.

Podesta, JJ. 2008. Laws for third-order moments in homogeneous anisotropic incompressible magnetohydrodynamic turbulence. *Journal of Fluid Mechanics* 609: 171–194.

———. 2009. Dependence of solar-wind power spectra on the direction of the local mean magnetic field. *The Astrophysical Journal* 698(2):986.

———. 2011. Spatial scales and temporal scales in the theory of magnetohydrodynamic turbulence. *Physics of Plasmas* 18(1):012906.

Politano, H, A Pouquet, and PL Sulem. 1995. Current and vorticity dynamics in three-dimensional magnetohydrodynamic turbulence. *Physics of Plasmas (1994-present)* 2(8):2931–2939.

Politano, Hélene, and Annick Pouquet. 1998. Dynamical length scales for turbulent magnetized flows. *Geophysical Research Letters* 25(3):273–276.

Pontin, DI. 2011. Three-dimensional magnetic reconnection regimes: A review. *Advances in Space Research*.

Priest, E.R., and P. Démoulin. 1995. Three-dimensional magnetic reconnection without null points 1. basic theory of magnetic flipping. *Journal of Geophysical Research* 100:23–23.

Pueschel, MJ, D Told, PW Terry, F Jenko, EG Zweibel, V Zhdankin, and H Lesch. 2014. Magnetic reconnection turbulence in strong guide fields: Basic properties and application to coronal heating. *The Astrophysical Journal Supplement Series* 213(2): 30.

Rappazzo, A.F., M. Velli, and G. Einaudi. 2010. Shear photospheric forcing and the origin of turbulence in coronal loops. *The Astrophysical Journal* 722(1):65.

Rappazzo, A.F., M. Velli, G. Einaudi, and R.B. Dahlburg. 2008. Nonlinear dynamics of the parker scenario for coronal heating. *The Astrophysical Journal* 677(2):1348.

Retinò, Alessandro, David Sundkvist, Andris Vaivads, F Mozer, Mats André, and CJ Owen. 2007. In situ evidence of magnetic reconnection in turbulent plasma. *Nature Physics* 3(4):236–238.

Schekochihin, AA, SC Cowley, W Dorland, GW Hammett, GG Howes, E Quataert, and T Tatsuno. 2009. Astrophysical gyrokinetics: kinetic and fluid turbulent cascades in magnetized weakly collisional plasmas. *The Astrophysical Journal Supplement Series* 182(1):310.

Schertzer, D, S Lovejoy, F Schmitt, Y Chigirinskaya, and D Marsan. 1997. Multifractal cascade dynamics and turbulent intermittency. *Fractals* 5(03):427–471.

Schmalzing, Jens, and Thomas Buchert. 1997. Beyond genus statistics: a unifying approach to the morphology of cosmic structure. *The Astrophysical Journal Letters* 482(1):L1.

Schmalzing, Jens, Thomas Buchert, Adrian L Melott, Varun Sahni, BS Sathyaprakash, and Sergei F Shandarin. 1999. Disentangling the cosmic web. i. morphology of isodensity contours. *The Astrophysical Journal* 526(2):568.

Schröder-Turk, Gerd E, Walter Mickel, Sebastian C Kapfer, Fabian M Schaller, Boris Breidenbach, Daniel Hug, and Klaus Mecke. 2013. Minkowski tensors of anisotropic spatial structure. *New Journal of Physics* 15(8):083028.

Servidio, S., A. Greco, W.H. Matthaeus, K.T. Osman, and P. Dmitruk. 2011. Statistical association of discontinuities and reconnection in magnetohydrodynamic turbulence. *Journal of Geophysical Research* 116(A9):A09102.

Servidio, S., W.H. Matthaeus, M.A. Shay, P.A. Cassak, and P. Dmitruk. 2009. Magnetic reconnection in two-dimensional magnetohydrodynamic turbulence. *Physical Review Letters* 102(11):115003.

Servidio, S., WH Matthaeus, M.A. Shay, P. Dmitruk, P.A. Cassak, and M. Wan. 2010. Statistics of magnetic reconnection in two-dimensional magnetohydrodynamic turbulence. *Physics of Plasmas* 17:032315.

Servidio, S, F Valentini, D Perrone, A Greco, F Califano, WH Matthaeus, and P Veltri. 2014. A kinetic model of plasma turbulence. *Journal of Plasma Physics* 81:1–35.

She, Zhen-Su, and Emmanuel Leveque. 1994. Universal scaling laws in fully developed turbulence. *Physical Review Letters* 72(3):336.

She, Zhen-Su, and Edward C Waymire. 1995. Quantized energy cascade and log-poisson statistics in fully developed turbulence. *Physical Review Letters* 74(2): 262.

Shimizu, Toshifumi. 1995. Energetics and occurrence rate of active-region transient brightenings and implications for the heating of the active-region corona. *Publications of the Astronomical Society of Japan* 47:251–263.

Sironi, Lorenzo, and Anatoly Spitkovsky. 2014. Relativistic reconnection: an efficient source of non-thermal particles. *The Astrophysical Journal Letters* 783(1):L21.

Sreenivasan, Katepalli R, and R. A. Antonia. 1997. The phenomenology of small-scale turbulence. *Annual review of fluid mechanics* 29(1):435–472.

Sreenivasan, KR, and P Kailasnath. 1993. An update on the intermittency exponent in turbulence. *Physics of Fluids A: Fluid Dynamics (1989-1993)* 5(2):512–514.

Stein, RF, and AA Nordlund. 2006. Solar small-scale magnetoconvection. *The Astrophysical Journal* 642(2):1246.

Strauss, H.R. 1976. Nonlinear, three-dimensional magnetohydrodynamics of noncircular tokamaks. *Physics of Fluids* 19:134.

Sweet, P.A. 1958. The neutral point theory of solar flares. In *Electromagnetic phenomena in cosmical physics*, vol. 6, 123.

Swisdak, M, JF Drake, and M Opher. 2013. A porous, layered heliopause. *The Astrophysical Journal Letters* 774(1):L8.

Swisdak, M, M Opher, JF Drake, and F Alouani Bibi. 2010. The vector direction of the interstellar magnetic field outside the heliosphere. *The Astrophysical Journal* 710(2):1769.

Tavani, M, A Bulgarelli, V Vittorini, A Pellizzoni, E Striani, P Caraveo, MC Weisskopf, A Tennant, G Pucella, A Trois, et al. 2011. Discovery of powerful gamma-ray flares from the crab nebula. *Science* 331(6018):736–739.

Telleschi, Alessandra, Manuel Güdel, Kevin Briggs, Marc Audard, Jan-Uwe Ness, and Stephen L Skinner. 2005. Coronal evolution of the sun in time: High-resolution x-ray spectroscopy of solar analogs with different ages. *The Astrophysical Journal* 622(1):653.

TenBarge, JM, and GG Howes. 2013. Current sheets and collisionless damping in kinetic plasma turbulence. *The Astrophysical Journal Letters* 771(2):L27.

Tennekes, H, and JC Wyngaard. 1972. The intermittent small-scale structure of turbulence: data-processing hazards. *Journal of Fluid Mechanics* 55(01):93–103.

Tessein, JA, WH Matthaeus, M Wan, KT Osman, D Ruffolo, and J Giacalone. 2013. Association of suprathermal particles with coherent structures and shocks. *The Astrophysical Journal Letters* 776(1):L8.

Thoroddsen, ST. 1995. Reevaluation of the experimental support for the kolmogorov refined similarity hypothesis. *Physics of Fluids (1994-present)* 7(4):691–693.

Tsinober, A. 1998. Is concentrated vorticity that important? *European Journal of Mechanics-B/Fluids* 17(4):421–449.

Uritsky, V. M., A. Pouquet, D. Rosenberg, P. D. Mininni, and E. F. Donovan. 2010. Structures in magnetohydrodynamic turbulence: Detection and scaling. *Physical Review E* 82(5):056326.

Uritsky, Vadim M, Joseph M Davila, Leon Ofman, and Aaron J Coyner. 2013. Stochastic coupling of solar photosphere and corona. *The Astrophysical Journal* 769(1):62.

Uritsky, Vadim M, Maya Paczuski, Joseph M Davila, and Shaela I Jones. 2007. Coexistence of self-organized criticality and intermittent turbulence in the solar corona. *Physical Review Letters* 99(2):025001.

Uzdensky, D.A., N.F. Loureiro, and A.A. Schekochihin. 2010. Fast magnetic reconnection in the plasmoid-dominated regime. *Physical Review Letters* 105(23): 235002.

Uzdensky, Dmitri A, and Jeremy Goodman. 2008. Statistical description of a magnetized corona above a turbulent accretion disk. *The Astrophysical Journal* 682(1):608.

Veronig, A., M. Temmer, A. Hanslmeier, W. Otruba, and M. Messerotti. 2002. Temporal aspects and frequency distributions of solar soft X-ray flares. *Astronomy and Astrophysics* 382:1070–1080.

Wan, M, WH Matthaeus, H Karimabadi, V Roytershteyn, M Shay, P Wu, W Daughton, B Loring, and Sandra C Chapman. 2012a. Intermittent dissipation at kinetic scales in collisionless plasma turbulence. *Physical Review Letters* 109(19):195001.

Wan, M, S Servidio, Sean Oughton, and William H Matthaeus. 2010. The third-order law for magnetohydrodynamic turbulence with shear: Numerical investigation. *Physics of Plasmas* 17(5):052307.

Wan, Minping, Kareem T Osman, William H Matthaeus, and Sean Oughton. 2012b. Investigation of intermittency in magnetohydrodynamics and solar wind turbulence: scale-dependent kurtosis. *The Astrophysical Journal* 744(2):171.

Wan, Minping, Antonio Franco Rappazzo, William H Matthaeus, Sergio Servidio, and Sean Oughton. 2014. Dissipation and reconnection in boundary-driven reduced magnetohydrodynamics. *The Astrophysical Journal* 797(1):63.

Wang, Y., S. Boldyrev, and J. C. Perez. 2011. Residual Energy in Magnetohydrodynamic Turbulence. *The Astrophysical Journal* 740:L36.

Whitcher, Brandon, Thomas Lee, Jeffrey B Weiss, Timothy J Hoar, and Douglas W Nychka. 2008. A multi-resolution census algorithm for calculating vortex statistics in turbulent flows. *Journal of the Royal Statistical Society: Series C (Applied Statistics)* 57(3):293–312.

Wicks, RT, TS Horbury, CHK Chen, and AA Schekochihin. 2010. Power and spectral index anisotropy of the entire inertial range of turbulence in the fast solar wind. *Monthly Notices of the Royal Astronomical Society: Letters* 407(1):L31–L35.

Wilkin, S Louise, Carlo F Barenghi, and Anvar Shukurov. 2007. Magnetic structures produced by the small-scale dynamo. *Physical Review Letters* 99(13):134501.

Yang, H., A. Zimmerman, and L. Lehner. 2015. Turbulent Black Holes. *Physical Review Letters* 114(8):081101. `1402.4859`.

Zhdankin, V., S. Boldyrev, and C. H. K. Chen. 2015a. Evidence for a log-normal energy cascade in alfénic turbulence. *In preparation*.

Zhdankin, V., S. Boldyrev, and J. Mason. 2012a. Distribution of magnetic discontinuities in the solar wind and in magnetohydrodynamic turbulence. *The Astrophysical Journal Letters* 760(2):L22.

Zhdankin, V., S. Boldyrev, J. C. Perez, and S. M. Tobias. 2014. Energy dissipation in magnetohydrodynamic turbulence: coherent structures or "nanoflares"? *The Astrophysical Journal* 795:127.

Zhdankin, V., S. B. Boldyrev, J. Mason, and J. C. Perez. 2012b. Magnetic discontinuites in mhd turbulence and in the solar wind. *Physical Review Letters* 108: 175004.

Zhdankin, V., D. A. Uzdensky, and S. Boldyrev. 2015b. Temporal analysis of dissipative structures in magnetohydrodynamic turbulence. *arXiv preprint arXiv:1506.08356*.

———. 2015c. Temporal intermittency of energy dissipation in magnetohydrodynamic turbulence. *Phys. Rev. Lett.* 114:065002.

Zhdankin, V., D. A. Uzdensky, J. C. Perez, and S. Boldyrev. 2013. Statistical Analysis of Current Sheets in Three-dimensional Magnetohydrodynamic Turbulence. *The Astrophysical Journal* 771:124.

Zweibel, Ellen G, and He-Sheng Li. 1987. The formation of current sheets in the solar atmosphere. *The Astrophysical Journal* 312:423–430.

Zweibel, Ellen G, and Masaaki Yamada. 2009. Magnetic reconnection in astrophysical and laboratory plasmas. *Annual Review of Astronomy and Astrophysics* 47:291–332.